UNIVERSITY OF CALIFORNIA
RIVERSIDE

# Motion Planning and Control of Compliant Autonomous Robots that Leverage Physical Interactions with the Environment

A Dissertation submitted in partial satisfaction
of the requirements for the degree of

Doctor of Philosophy

in

Electrical Engineering

by

Zhichao Liu

June 2023

Dissertation Committee:

Dr. Konstantinos Karydis, Chairperson
Dr. Amit K. Roy-Chowdhury
Dr. Jun Sheng

Copyright by
Zhichao Liu
2023

The Dissertation of Zhichao Liu is approved:

---

---

---

Committee Chairperson

University of California, Riverside

## Acknowledgments

First and foremost, I am immensely grateful to my advisor, Dr. Konstantinos Karydis, which has played a crucial role in bringing me to this point. I thank Professor Karydis for consistently providing me with invaluable guidance, support, and motivation. His advice, tools, resources, and help have been critical in helping me complete my studies and achieve success in my work. I am profoundly inspired by his dedication and enthusiasm for research, and the skills I have acquired under his mentorship will greatly contribute to my future endeavors.

I extend my gratitude to the faculty members who provided invaluable guidance and support throughout my academic journey. I am particularly grateful to Dr. Amit K. Roy-Chowdhury and Dr. Jun Sheng for their contributions as members of my committee. I would also like to express my appreciation to all the professors whose courses not only inspired me and expanded my knowledge but also improved my skill set. In addition, I am deeply grateful to all the peer-reviewers who consistently motivate and inspire me to enhance my studies.

Throughout the years, I have been extremely fortunate to work with a great team of lab mates, Dr. Caio Mucchiani, Dr. Mohamed Karim Bouafoura, Dr. Xinyue Kan, Dr. Zhouyu Lu, Dr. Lu Shi, Hanzhe Teng, Keran Ye, Amel Dechemi, Merrick Campbell, Cody Simons, Dimitris Chatziparaschis, Georgia Kouvoutsakis, Xiao'ao Song, Mehrnoosh Ayazi, Pamodya Peiris, Gustavo Correa. I would like to express my gratitude to the collaborators who have helped me in my research: Dr. Elena Kokkoni, Dr. Ali-akbar Agha-mohammadi, Dr. Elia Scudiero, Ipsita Sahin, Jared Dude and Linh Vu. Specially, I appreciate all the

help from Dr. Zhouyu Lu during the time that we worked closely together. This work would not have been possible without him.

This work has received financial support from various funding agencies, including NSF (grants #IIS-1724341, #IIS-1910087 and #IIS-1901379), ONR (grants #N00014-18-1-2252 and #N00014-19-1-2264), and ARL (grant #W911NF-18-1-0266). Additionally, I would like to express my gratitude to the Department of Electrical and Computer Engineering at the University of California-Riverside for providing funding through a 3-quarter fellowship and a 3-quarter teaching assistantship during my studies.

On a personal note, I would like to express my deepest gratitude to my mother Meifang Xiao, father Jinghua Liu, partner Linh Vu and my siblings, who have been a never-ending source of inspiration and motivation throughout my journey. Without their unwavering support, it would be impossible for me to complete my study. Furthermore, I would like to express my gratitude to my friends at UCR, Sam Thai, Chujing Zheng, Shan Sun, Pengxiang Zhu, Yong Ding, and Shaoshu Su, for their encouragement and valuable advice.

To my mother Meifang Xiao, father Jinghua Liu, and partner Linh Vu for your unwavering love and support.

# ABSTRACT OF THE DISSERTATION

Motion Planning and Control of Compliant Autonomous Robots that Leverage Physical Interactions with the Environment

by

Zhichao Liu

Doctor of Philosophy, Graduate Program in Electrical Engineering
University of California, Riverside, June 2023
Dr. Konstantinos Karydis, Chairperson

Development of autonomous robots that can leverage physical interactions with the environment has been increasingly attracting interest owing to the potential across applications such as precision agriculture, last-mile delivery, automated warehouses, search-and-rescue, and environmental monitoring. In addition to compliant control of rigid joints, robots with compliant or variable-stiffness bodies offer benefits such as reducing impact and adapting to different environments. This dissertation contributes to fundamental theory and practical algorithms for studying compliant aerial and legged robots capable of physical interactions with their operating environment or other robots. The dissertation spans over modeling, control, and motion planning of aerial and legged robots, specifically focusing on stabilizing from high-speed collisions, catching flying targets, and traversing rough terrain. In the first part, we introduce resilient aerial robots equipped with compliant arms to minimize impact and detect contact. We study the dynamic modeling of the compliant vehicle when experiencing external impacts and propose a recovery method to promptly stabilize the vehicle from high-speed collisions. Furthermore, we present a collision-inclusive planning

method that prioritizes contacts to facilitate navigation of aerial robots in partially-known cluttered environments. Simulated and physical experiments are conducted to demonstrate the advantages of the robot and the effectiveness of the proposed planner. The second part focuses on robot-robot interactions by presenting a solution for safely catching an aerial micro-robot in mid-air using another aerial robot equipped with a universal soft gripper. In addition to modeling and controlling the aerial vehicle, we study a planning method to avoid aerodynamic disturbances that could destabilize flying targets. Experimental results showcasing the safe capture of static and moving aerial targets are presented to demonstrate the efficacy of the approach. The third part extends the study to soft legged robots designed to traverse challenging terrains. We introduce a novel soft hexapedal robot and develop an efficient gait for overcoming rough terrain. We propose a static model for feedforward position control and present a pressure feedback controller and a closed-loop variable-height trajectory tracking method. These advancements aim to enhance the overall performance and versatility of the robot in various real-world scenarios.

# Contents

# List of Figures

# List of Tables

# Chapter 1

# Introduction

Autonomous robots have found applications in various fields, such as precision agriculture [200,201], last-mile delivery [8], automated warehouses [106], search-and-rescue [71], and environmental monitoring [150], to name a few. Although navigation and exploration with obstacle avoidance have been extensively studied (e.g., [79, 86–88, 213]), autonomous robots that leverage physical interactions with the environment have attracted increasing interest from both academia and industry. Physical interactions involve instantaneous or constant external forces that are applied on the robots, which pose challenges to robot stability and navigation [161]. Robotic applications with physical interactions include but are not limited to human-robot [9, 182], robot-environment [3, 180] and robot-robot [51, 158] interactions. While service robots with human-robot interactions have been extensively studied and found successful industrial applications [68, 177], the scope of this study focuses on the robot-environment and robot-robot interactions. In the robot-environment interaction case, two separate topics are studied: 1) robots undergoing physical collisions in

cluttered environments; and 2) robots traversing rough terrains. In the robot-robot interaction case, this dissertation studies the topic of using a robot to capture another moving robot.

Compliant control of rigid joints using modern torque regulators have been successfully applied to manipulators [2, 21, 175, 187], legged robots [118, 178, 190] and aerial robots [9, 205]. In recent years, there is a growing interest in robotic systems with compliance or variable stiffness, which have the benefits of reducing impact and adapting to environments [168, 221]. In contrast to a large amount of research efforts in hardware designs based on advances in material science, model-based motion control and path planning of compliant robots that undergo physical interactions have been critically missing in the literature [39]. Furthermore, multiple limitations exist in the related studies on compliant robots with physical interactions as they usually fail to 1) study high-speed interactions with large contact forces, 2) incorporate frequent and periodic interactions, 3) consider robot-robot interactions, and 4) apply to agile robots such as multi-copters. This dissertation aims to address the aforementioned limitations. Overall, the scope of the study herein is threefold.

- **Focus 1**: Modeling, control and collision-inclusive planning of compliant aerial robots that can stabilize following high-speed collisions.
- **Focus 2**: Modeling, control and trajectory generation of an aerial robot with a soft gripper to catch flying micro-robots.
- **Focus 3**: Modeling, control and trajectory tracking of a soft legged robot that can traverse challenging terrains.

These topics exhibit some synergies as well as unique differences. First, **Focus 1** studies compliant robots while **Focus 2 & 3** consider variable-stiffness (soft) ones. Second, **Focus 1 & 2** apply to aerial vehicles while **Focus** 3 presents a multi-legged robot. Third, **Focus 1 & 3** consider robot-environment interactions while **Focus 2** studies the robot-robot case. Lastly, **Focus 1** studies high-speed interactions with environments while **Focus 3** covers the frequent and periodic case.

Specifically, in **Focus 1**, we introduce a novel aerial robot that is equipped with compliant arms to sense and survive from high-speed collisions with walls. Dynamics modeling for both compliant arms and contact is derived to quantify the impact reduction. An effective recovery method is utilized to stabilize the robot swiftly after collisions with aggressive maneuvers. Second, we study an impact-resilient aerial robot with an integrated compliant contact arm that features a real-time contact force estimator. Collision resilience is enhanced to wall and pole obstacles with a collision handling method proportional to the contact force intensity. Utilizing the impact resilience, a new collision-inclusive planning method that aims to prioritize contacts to facilitate aerial robot navigation in cluttered environments is proposed. A range of simulated and physical experiments demonstrate key benefits of the robot and the contact-prioritized (CP) planner.

In **Focus 2**, we present a method for safely catching an aerial micro-robot in mid-air using another aerial robot equipped with a universal soft gripper. To prevent aerodynamic disturbances that could push the target robot away, a horizontal grasping approach is employed. The gripper design is based on soft actuators, allowing it to maintain a horizontal position and bend when air pressure is applied. The work further introduces a planning

method that utilizes piecewise polynomial optimization to safely catch flying micro-robots while avoiding destabilizing the target. Experimental results of catching static and moving aerial targets are shown to demonstrate the efficacy of the developed method. Free flight performance of the robot is compared to that of a conventional quadrotor, considering different gripper and payload conditions.

In **Focus 3**, we introduce a pioneering pneumatically-actuated soft hexapedal robot equipped with 2-DoF soft pneumatic actuators. These actuators possess the capability to bend and extend, allowing for the generation of foot trajectory profiles that are well-suited for legged locomotion to traverse rough terrain. We then extend the motion capabilities of the robot by proposing a static model based on geometric constraints for feedforward position control. Additionally, we propose a pressure feedback controller and a closed-loop variable-height trajectory tracking method that rely on pneumatic pressure regulation.

## 1.1 Motivation and Related Works

**Impact-resilient Compliant Aerial Robots.** The use of aerial robots is expanding across various domains, particularly in challenging and cluttered environments [83, 133]. In these scenarios, ensuring the safety of the system and its surroundings is of utmost importance. Extensive efforts are being devoted to developing collision avoidance systems that are robust and high-performing. However, it is important to recognize that collisions cannot always be completely avoided, as supported by theoretical studies and observations of insects and birds that frequently experience impacts with their environment or with each other [35]. Several compliant aerial robots have been developed over the years. In Ref [12],

an aerial robot with a compliant contact arm was developed. Examples of works integrating compliant protective structure onto the robot include origami-inspired mechanisms [173,186] and an icosahedron tensegrity structure [215]. In Ref [37], an impact-resilient MAVs with external compliant flaps was studied. Compliance has also been included into the robot chassis to reduce impact. In Ref [26], a collision-resilient insect-scale compliant flapping-wing robot was developed, while a collision-resilient MAV with foldable arms was introduced in [147]. Soft aerial robots were developed for physical interactions [143, 166]. Further, insect-inspired multicopters are presented with compliant frames to handle collisions [131] whereas compliant frames based on tensegrity [174] are shown helpful to reduce impact. Our prior work developed a collision-resilient MAV with compliant arms [110].

**Collision-inclusive Planning.** Recent research has highlighted the advantages of incorporating collisions into various aspects of robotics. Studies have demonstrated the benefits of allowing collisions in motion planning and control [88, 141, 191], localization [123], and sensing [140,141]. Embracing collision behaviors can enhance agile movement [137], improve the robustness of planners [141], enable more precise localization [123], and facilitate obstacle sensing, especially for objects that are challenging to detect using long-range sensors like LiDAR [140]. In contrast to traditional collision avoidance approaches, incorporating contacts and embracing collisions can enhance the safety and effectiveness of navigation tasks. For instance, an integrated collision model with mixed-integer programming has been used to optimize trajectories [137]. Contacts can also be leveraged to improve velocity estimation [105]. Studies have explored the trade-offs between risk and reward for collision-inclusive trajectories [36, 115]. Local re-planning techniques, coupled with set-

point adjustment post-collision, have been proposed to enhance global planners such as A$^\star$ [114, 116] and sampling-based methods [214].

**Compliant Grasping of Flying Robots.** The ability of aerial robots to grasp objects has gained significant attention from research institutes and companies across various industries. This interest stems from the unique advantage of aerial robots operating in three-dimensional (3D) space, free from the terrain constraints that often limit ground robots and human operators [164]. Grasping plays a vital role in enabling aerial robots to interact with the environment, facilitating various important applications such as inspection [211], search-and-rescue [67], transportation [56], and construction [10]. In recent years, several micro aerial vehicles (MAVs) have been equipped with soft (compliant) end-effectors, including but not limited to impactive and ingressive [128], compliant multi-fingered [7, 24, 65, 101, 125, 152, 217], closed-structure compliant [103], origami-inspired [91], wasp-pedal-carrying [219], soft cable-driven [57, 157], and soft pneumatic [132] grippers. Physically catching flying robots in mid-air is challenging due to their irregular shapes and self-propulsion. The most common way to catch flying robots in mid-air is using nets, such as net bullets [44, 130], top nets [43, 162], side nets [209], and nets carried by cooperative vehicles [94, 163].

**Autonomous Soft Legged Robots.** Soft robotics technology has been extensively explored and developed for locomotion applications, with previous works focusing on soft robots powered by soft pneumatic actuators (SPAs) to achieve crawling and undulation gaits [58, 181, 204]. For instance, a starfish-like soft robot utilized shape memory alloys for

actuation to accomplish crawling gaits [120]. Legged robots leverage cable-driven actuators, such as the Sofia walking robot [50] and Puppy [15]. Past research on soft robots' modeling and control has mostly focused on single actuators or soft manipulators.Piecewise constant curvatures [22,122] and variable curvature models [119] have been proposed to achieve feedforward control. Other attempts include Cosserat rod [48], mass-damper-spring-based [69], linear parameter-varying [155], and finite element method-based [17] models. Those models have then been used to develop various feedforward or feedback control methods, including proportional-integral-derivative (PID) [17], sliding mode [188], model predictive control [16] and learning-based methods [203]. Research on motion control of soft pneumatic mobile robots has primarily focused on planar locomotion, featuring soft robotic snakes [117, 144, 156]. A recent work presents a continuum soft robot capable of tracking trajectories and interacting with the environment [39].

## 1.2 Objective and Significance

The objective of this dissertation is to systematically study compliant autonomous robots that leverage physical interactions with the environment. Aspects of this dissertation extend over robot design and fabrication, dynamic modeling, motion control, and motion/path planning. More specifically, the dissertation seeks to answer:

- **Aim 1**: What are the effects (positive and negative) of incorporating compliance in robotic tasks with physical interactions?
- **Aim 2**: How to precisely model the dynamics of autonomous robots while considering the added compliance and external forces?

- **Aim 3**: How to intelligently utilize the added compliance to facilitate motion planning tasks with physical interactions?

**Compliant Aerial Robots to Stabilize Collisions.** We start from the design of a novel actively resilient quadrotor, which incorporates passive springs within its arms to reduce impact and survive from collisions. We develop a method to fuse readings from Hall effect sensors to rapidly detect contact and characterize compliance changes due to impact. We also introduce dynamics modeling for both compliant arms and contact using Kelvin-Voigt (KV) and Hunt and Crossley (HC) [75] models for wall collisions. Taking advantage of the compliant airframe and a geometric tracking controller, we propose an effective recovery method to generate and track a setpoint post collision. Experimental results are shown to support the strong resilience to high-speed and large-angle collisions against vertical walls.

**Contact-Prioritized Planning of Impact-resilient Aerial Robots.** We present the design and dynamic modeling of an impact-resilient aerial robot with an integrated compliant arm to sense contacts and reduce collision impact. We further propose an estimator to estimate real-time contact force in presence of compliance. Owing to the impact reduction and real-time contact force estimator, we enhance the impact resilience to stabilize from high-speed wall and pole collisions. Further, we harness s-ARQ's strong collision resilience capability to propose a novel planning method that prioritizes contacts. Extensive simulated and physical tests are conducted to evaluate the planning method against representative collision-avoidance planning methods in partially-known cluttered environments.

**Compliant Aerial Grasping to Safely Catch Flying Targets.** We propose a technique for securely capturing an aerial micro-robot while it is in mid-air using another aerial robot equipped with a versatile soft gripper. In order to avoid any aerodynamic disturbances that might push the target robot away, we adopt a horizontal grasping approach. The gripper design is based on soft actuators, which enables it to maintain a horizontal orientation and flex when subjected to air pressure. Additionally, our work introduces a planning method that utilizes piecewise polynomial optimization to ensure a safe capture of flying micro-robots while avoiding destabilizing the target. We present experimental results that demonstrate the effectiveness of capturing both stationary and moving aerial targets. Furthermore, we compare the free flight performance of the robot to that of a conventional quadrotor under various gripper and payload conditions. The robot can be used in search-and-rescue of aerial robots or seize unidentified flying targets without damage. In the meantime, the robot can move fragile objects as a conventional aerial gripper, with potential applications in aerial transportation and construction.

**Soft Pneumatic Hexapedal Robot to Traverse Challenging Terrains.** Unlike rigid legged robots, soft legged robots have the ability to squeeze and bend, allowing them to overcome obstacles and explore narrow spaces. We introduce an innovative soft hexapedal robot (SoRX). The robot utilizes a novel 2-DoF soft pneumatic actuators, which can both bend and extend, enabling the creation of foot trajectory profiles suitable for legged locomotion. We propose an alternating tripod gait for the robot and demonstrate that the method is highly effective for locomotion in various terrains, including flat, rough, steep, and unstable surfaces.

**Model-based Motion Control and Trajectory Tracking of a Soft Legged Robot.** We extend the motion capabilities of a soft pneumatic legged robot SoRX, which has shown able to traverse rough, steep and unstable terrain. We present a static model for feedforward position control (body height and orientation) of our soft pneumatic legged robot SoRX. With the aim of deploying the robot in outdoor environments, we propose a fast and precise air pressure feedback controller that utilizes a custom low-cost pneumatic regulation board. We further propose a closed-loop trajectory tracking method to enable the robot to track variable-height trajectories trajectories.

## 1.3 Contributions

Overall, this dissertation contributes to multiple aspects, ranging from compliant robot design principles to collision-inclusive motion planning algorithms, aimed at handling modeling, control and planning of autonomous robots that are capable to leverage physical interactions via exploiting physical compliance embedded onto their bodies. These advancements can be applied to various robotic applications such as precision agriculture, last-mile delivery, automated warehouses, search-and-rescue, and environmental monitoring.

To achieve **Aim 1**, we investigate various types of compliant robotic platforms, including compliant aerial robots with either four compliant arms or one compliant arm, an aerial vehicle equipped with a compliant gripper, and a soft hexapedal robot. Our focus is on analyzing the impact of incorporating compliance in different robotic applications, such as collisions, grasping, and navigating rough terrain. Through experiments, we demonstrate the significant benefits of compliance in these areas. In **Focus 1**, compliant aerial robots

exhibit outstanding resilience, successfully stabilizing from high-speed, large-angle collisions. **Focus 2** showcases a groundbreaking solution: utilizing an aerial robot with a compliant gripper to safely capture another flying micro-robot. We also experimentally examine the compliant grasping in terms of closing speeds and success rates under disturbances compared to a commercial gripper. In **Focus 3**, we explore the influence of variable-stiffness legs on locomotion across rough terrain. Specifically, the developed soft legged robot achieves remarkable running speeds compared to its body length and effectively traverses challenging landscapes, including steep and unstable surfaces.

Furthermore, we expand our research to include dynamic modeling of both aerial and legged platforms, taking into account the added compliance and physical interactions (referred to as **Aim 2**). Specifically, we introduce dynamic models for compliant arms and contact interactions, employing Kelvin-Voigt and Hunt and Crossley models to analyze wall collisions. In **Focus 1**, we go a step further by deriving the dynamic model of the system while considering external forces of the compliant aerial robots to stabilize from high-speed collisions. Additionally, in **Focus 2**, we investigate the dynamics of an aerial vehicle equipped with an onboard manipulator and incorporate the presence of a target payload. Lastly, in **Focus 3**, we employ the finite element analysis technique to dynamically model the compliant legs, which utilize pneumatic actuation. This enables us to propose an effective static model for feedforward position control, specifically for navigating and exploring, by utilizing the innovative compliant legged robot.

To achieve **Aim 3**, we propose a motion planning framework to utilize collisions to facilitate navigation by taking advantage our developed compliant aerial robots' strong

resilience to impacts (**Focus 1**). Simulated and physical tests are conducted to evaluate the proposed contact-prioritized planning method in partially-known and cluttered environments, compared to representative collision avoidance algorithms such as A* and sampling-based planners. Results show that our solution can accelerate computation time while having shorter trajectory time and larger clearances compared to other planners with velocity constraints. Online planning tests in partially-known environments further demonstrate the preliminary feasibility in practical use cases. In **Focus 2**, we present a planning method based on piecewise polynomial optimization to catch the flying micro-robots without generating aerodynamic disturbances detrimental to the target's stability. We experimentally demonstrate the feasibility of using the robot to catch a hovering micro-robot and return with the target. To the best of our knowledge, the developed aerial robot (called SoAG) is the first MAV to demonstrate the feasibility of catching a flying micro-robot with a soft gripper. In **Focus 3**, we propose a closed-loop trajectory tracking method for the innovative soft legged robot. We experimentally demonstrate that the robot can track two planar trajectories (a straight line and a quarter circle), as well as variable-height trajectories.

## 1.4 Dissertation Layout

The remainder of this dissertation is organized as follows. Chapter 2 focuses on dynamic modeling and recovery control of a compliant aerial robot to stabilize from collisions (**Focus 1**). Chapter 3 extends the aerial resilience by including an estimator to estimate real-time contact forces in the presence of compliance. Further, we propose a novel planning method that prioritizes contacts. Extensive simulated and physical tests

are conducted to evaluate the planning method in partially-known cluttered environments (**Focus 1**). Then, Chapter 4 study effects of compliance on robot-robot interactions by presenting an innovative solution to utilize an aerial robot with a compliant gripper to safely capture another flying micro-robot (**Focus 2**). Furthermore, we compare the free flight performance of the robot to that of a conventional quadrotor under various gripper and payload conditions. Then, Chapter 5 introduces a novel soft hexapedal robot and an efficient gait for locomotion in various terrains, including flat, rough, steep, and unstable surfaces (**Focus 3**). Then, we extend the motion capabilities of the robot by including a static model for feedforward position control, as well as a closed-loop trajectory tracking method to enable the robot to track variable-height trajectories in Chapter 6 (**Focus 3**). Finally, Chapter 7 summarizes the contributions of this dissertation and provides pointers for further research enabled by the work presented herein.

# Chapter 2

# Modeling and Control of Compliant Impact-Resilient Aerial Robots

In this chapter, we study the compliance of aerial robots that collide with their environment. Specifically, we present a novel actively resilient quadrotor (ARQ), which incorporates passive springs within its arms to reduce impact and survive collisions. Dynamics modeling for both compliant arms and contact is derived to quantify the impact reduction. Physical collision experiments against both rigid walls and soft mats are used to verify the proposed modeling method. Extended simulation results show that compliant arms can reduce contact impact by 493 $m/s^2$ or 50.26 G (gravity constant) at a collision speed of 6 m/s. Owing to a nonlinear tracking controller and the compliant airframe, the robot can survive collisions against walls at speeds of up to 3.5 m/s. The robot can also

survive collisions with contact angles of up to 45° at a speed of 2 m/s. Repeated physical experiments demonstrate 100% success rates for all collision tests ranging from high-speed to large-angle ones. Further, the article includes comprehensive comparisons with a rigid MAV in both free flight performance and impact resilience.

This chapter is organized as follows: Section 2.1 discusses background and related works for impact-resilient aerial autonomy, as well as frames definition, key notations and assumptions; Section 2.2 introduces the overview design of the novel compliant aerial vehicle; Section 2.3 introduces the dynamic modeling of both rigid and compliant aerial robots, as well as the impact. In Section 2.4, we introduce methods to characterize the collision and estimate the compliance based on the Hall effect sensors on the compliant arms. In Section 2.6, we experimentally test the model identification and the resilience to high-speed and large-angle collisions with vertical walls.

## 2.1 Background

Micro Aerial Vehicles (MAVs) can serve as ubiquitous platforms for sensor-based exploration and navigation. In recent years, there has been a growing interest in deploying MAVs in challenging environments, including but not limited to confined [37, 105, 206] and cluttered [141, 220] ones. Collision risks get significantly higher for autonomous missions in these complex environments, especially at high speeds. To mitigate the risk, multiple impact-resilient vehicles [37, 147, 215] have been developed, with applications to collision-tolerant navigation [116, 214].

### 2.1.1 Related Work

Mechanical protective cages and reinforced frames [29, 40, 41, 90, 93, 140, 142] can help the hardware survive crashes. When high-speed collisions occur, however, the impact energy is still directly transferred to the robot, which in turn may damage sensitive electronic components (IMU, camera or LiDAR), despite the existence of protective mechanical designs [148]. A way to address this challenge is via novel MAV designs that integrate compliance into the airframe to reduce impact. Examples of compliant MAV include ones with purely soft frames [173,186], icosahedron tensegrity structure [215], external compliant flap [37], and foldable arms with passive springs [110, 147].

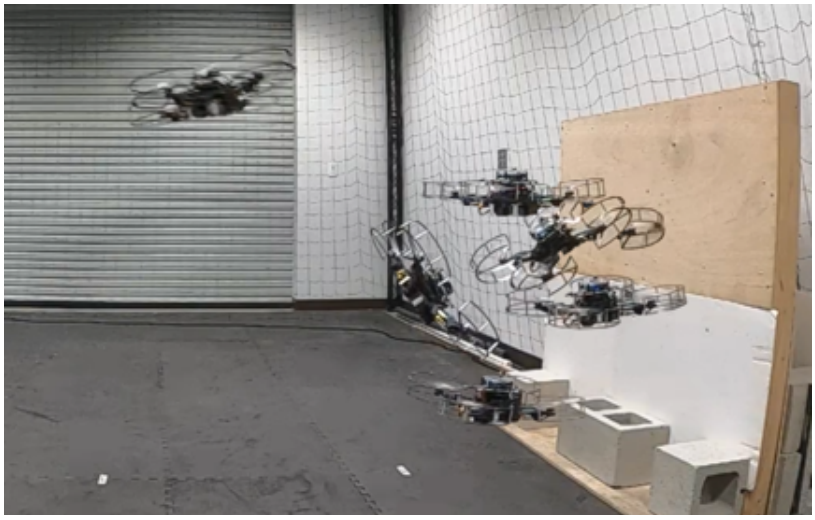

Figure 2.1: The compliant MAV developed in this work can rapidly stabilize from collisions with vertical walls at speeds of up to 3.5 m/s and sustain post-impact flight by tracking aggressive recovery trajectories. Composite images are made with a camera in 240 fps.

Compliant MAVs can reduce effects of impact and help survive collisions. Yet, multiple interesting questions remain open: impact modeling, and the ability to stabilize large-angle collisions, and lack of comparisons with rigid robots. The first question arises with respect to modeling collisions, as well as the added compliance. Although modeling

impacts has been thoroughly studied [66], only few existing works on rigid aerial robots take it into consideration. Notable examples include the impulse-momentum principle model in [141] and viscoelastic models in [29, 41]. The latter does not rely on the assumption of instantaneous collisions, therefore it can be applied to modeling the contact with a variety of compliant surfaces [1]. It is also necessary to model the added compliance to describe its effect on impact reduction. Prior work [147] uses a damper and spring model to describe the arm length, however, the method assumes massless compliant arms, which remains questionable to describe fast and periodic movements [27]. Furthermore, impact modeling is not included in the work [147] either.

Second, a majority of existing works on MAV collision and recovery share the assumption that the contact angle is close to zero. This restriction partly comes from linear flight controllers that rely on the small angle approximation near the hovering state [37]. However, fast autonomous flight of MAVs involves large accelerations and attitude changes [53, 102, 159]. The ability to stabilize large-angle collisions remains crucial for fast and autonomous missions of MAVs in challenging environments. Notable exceptions include related work on rigid aerial robots [40, 41] that show successful collision recovery with contact angles up to 30° in physical tests. On the other hand, none of the existing works studies the recovery success rates in different contact angles, which will promote the confidence in deploying MAVs in unknown environments.

Lastly, introducing compliance within the airframe can negatively affect the free flight performance. The increased weight may shorten flight time. The compliance may introduce modeling errors and degrade trajectory tracking performance based on model-based

control. For these reasons, it is important to study the free flight performance of compliant MAVs compared to rigid ones, however, such study is critically missing in the literature. Additionally, existing works fail to include comparisons with rigid robots as well when evaluating the impact resilience. Prior work [147] and our previous work [110] both utilize compliant robots to mimic rigid ones with additional reinforcement, however, reinforced compliant MAVs may not have similar performance as their conventional counterparts.

This work addresses the three open questions mentioned above, and provides a template for designing and developing compliant MAVs that can be applied to collision-tolerant navigation. Specifically, we present a novel actively resilient quadrotor (ARQ), which incorporates passive springs within arms to reduce impact and survive crashes (Fig. 2.1). The robot is equipped with Hall effect sensors to rapidly detect contact. We also introduce dynamics modeling for both compliant arms and contact using Kelvin-Voigt (KV) and Hunt and Crossley (HC) [75] models, respectively. Physical collision experiments against both rigid walls and soft mats are used to verify the proposed models.

An effective and intuitive recovery method is adopted to generate and track a setpoint post collision. Taking advantage of the compliant airframe and a geometric tracking controller, the robot can survive collisions against walls at speeds of up to 3.5 m/s. The robot is also observed to survive collisions with contact angles of up to 45° at a speed of 2 m/s. Repeated physical experiments demonstrate 100% success rates for all collision tests ranging from high-speed to large-angle ones. Further, the article includes comprehensive comparisons with a rigid MAV in both free flight performance and impact resilience.

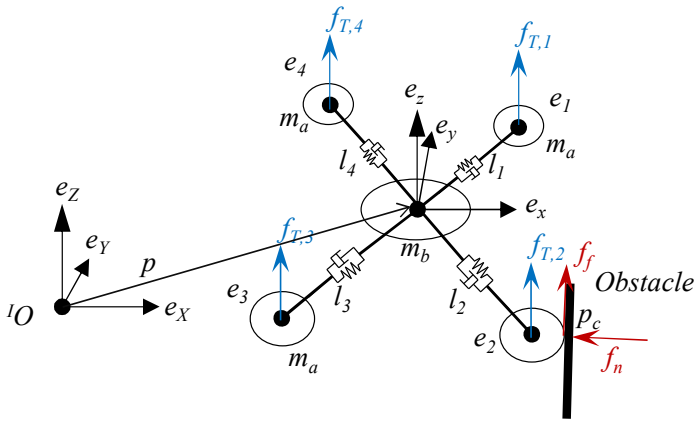


Figure 2.2: Inertial and body-fixed frames description. The robot is represented by five rigid bodies during impact. Thrust force (blue) and contact force (red) are shown in the body-fixed frame. Vector $e_j$ is the relative position of the arm $j$ in the body-fixed frame, while $p$ is the position of the main body in the inertial frame.

### 2.1.2 Frames, Key Notations and Assumptions

Different from dynamics of rigid quadcopter MAVs with elastic contacts [139], we study herein the added compliance along the MAV arms in a way similar to legged locomotion compliance modeling [207]. We study the dynamics in free flight and collision scenarios separately. Note that index $j = 1, 2, 3, 4$ is frequently used to represent the rigid body along the arm $j$. Key notation is shown in Tab. 2.1.

As shown in Fig. 2.2, the NWU (X North, Y West, Z Up) is used as the inertial frame $\mathcal{F}_I$ , while the FLU (X Forward, Y Left and Z Up) is selected for the body-fixed frame $\mathcal{F}_B$. We also define unit vectors $e_j \in \mathbb{R}^3$ to denote the direction of arm $j$ in body frame. For example, $\boldsymbol{e}_1 = [1/\sqrt{2}, 1/\sqrt{2}, 0]^T$, $\boldsymbol{e}_2 = [1/\sqrt{2}, -1/\sqrt{2}, 0]^T$. We make the following assumptions.

1. Rotor drag, moment generated by propeller angular speeds, and friction of the prismatic joint on compliant arms are ignored.

Table 2.1: Key Notation in Chapter 2

| | |
|---|---|
| $\mathcal{F}_I = \{\boldsymbol{e}_X,\ \boldsymbol{e}_Y,\ \boldsymbol{e}_Z\}$ | inertial frame |
| $\mathcal{F}_B = \{\boldsymbol{e}_x,\ \boldsymbol{e}_y,\ \boldsymbol{e}_z\}$ | body-fixed frame |
| $m_b \in \mathbb{R}$ | the mass of main body |
| $m_a \in \mathbb{R}$ | the mass of each arm |
| $\boldsymbol{p}_b \in \mathbb{R}^3$ | position of main body in inertial frame |
| $\boldsymbol{p}_j \in \mathbb{R}^3$ | position of arms $j$ in inertial frame |
| $\boldsymbol{e}_j \in \mathbb{R}^3$ | unit vector of arm $j$ in body frame |
| $\boldsymbol{p}_{c,j} \in \mathbb{R}^3$ | position of contact point along arm $j$ in inertial frame |
| $\boldsymbol{v}_b \in \mathbb{R}^3$ | velocity of main body in inertial frame |
| $\boldsymbol{v}_j \in \mathbb{R}^3$ | velocity of arms $j$ in inertial frame |
| $\boldsymbol{R} \in \mathsf{SO(3)}$ | rotation matrix from body to inertial frame |
| $\boldsymbol{\omega} \in \mathbb{R}^3$ | angular velocity in body frame |
| $\boldsymbol{q} \in \mathbb{R}^4$ | orientation of the robot in inertial frame |
| $l_j \in \mathbb{R}$ | length of arm $j$ in body frame |
| $L \in \mathbb{R}$ | free length of all arms |
| $r_0 \in \mathbb{R}$ | radius of the protect cage |
| $\boldsymbol{I} \in \mathbb{R}^{3\times3}$ | moment of inertia matrix |
| $f_{T,j} \in \mathbb{R}$ | thrust generated by arm $j$ in body frame along $e_z$ axis |
| $\boldsymbol{f}_{n,j} \in \mathbb{R}^3$ | normal force by contact on arm $j$ |
| $\boldsymbol{f}_{f,j} \in \mathbb{R}^3$ | frictional force by contact on arm $j$ |
| $\boldsymbol{\mathcal{Q}} \in \mathbb{R}^{10}$ | generalized coordinates in Euler-Lagrange |
| $\boldsymbol{F}_{\text{ext}} \in \mathbb{R}^{10}$ | generalized external force |
| $k_l, b_l \in \mathbb{R}$ | spring and damping coefficients of arms |
| $k_c, b_c \in \mathbb{R}$ | spring and damping coefficients of contact |

2. The motors are encircled by protective cages that retain the shape during collisions.

3. During impact, the robot is modeled as five distinct rigid bodies.

4. During impact, the rigid body of arm $j$ only has one degree of freedom (dof) along $e_j$.

5. In free flight, the robot remains a single rigid body.

6. The contact only results in kinetic friction with the obstacle.

## 2.2 Compliant Vehicle Design

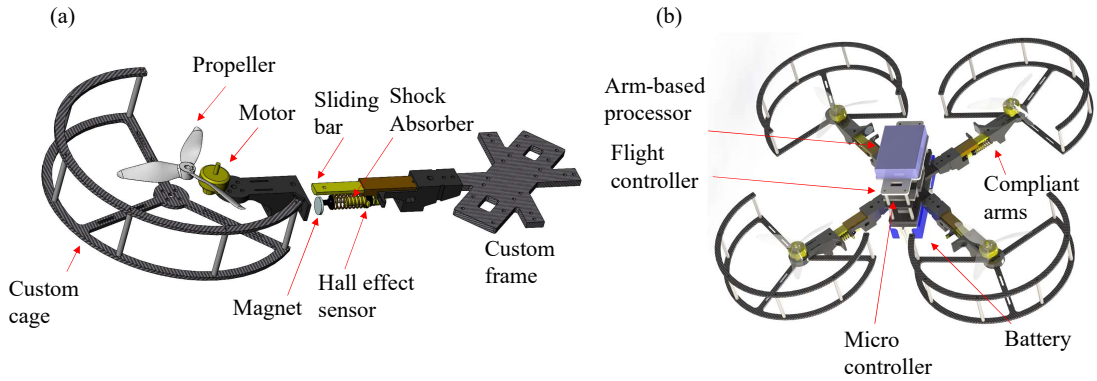


Figure 2.3: (a) The exploded view of the compliant arm design in the computer-aided design (CAD) software. (b) A CAD rendering image of the compliant MAV featuring the novel foldable arms to reduce impact.

With an eye to resilient autonomous flight in challenging environments, this project focuses on medium weight MAVs, which can carry popular perception devices and run navigation onboard. With a purpose to endure and reduce impact while retaining rigidity for model-based control in free flight, this work presents a novel compliant arm design.

Figure 2.3a shows an exploded view of the arm design in computer-aided design software. The compliant arms feature a prismatic joint, shock absorber, Hall effect sensor, magnet and custom protective cage. The prismatic joint is built based on a metallic sliding bar, while the shock absorber is directly taken from 1/18 radio-control cars. An A1302 ratiometric linear Hall effect sensor is fixed on the prismatic joint to measure the magnetic intensity. The adapters connecting the prismatic joint and shock absorber are 3D-printed (Markforged Mark II, onyx material with carbon fiber add-in). The custom cages and frames are fabricated in lightweight carbon fiber sheets (tensile strength 120,000-175,000 psi) using a Stepcraft D.600 CNC router with enclosure and milling bath.

The ability to detect and characterize collisions is critical to stabilize quadrotors and sustain flight. Aside from common methods based on IMU [40], this project utilizes Hall effect sensors to report collisions as in [20]. Hall effect sensors also measure the length of compliant arms in real-time and facilitate deformation estimation. Despite the relatively short distance, the Hall effect sensors are not affected by rotating motors. Additionally, Hall effect sensors and embedded magnets do not affect the IMU in the flight control unit as well, which makes the method feasible in outdoor environments [110].

Table 2.2: Key Features of Compliant and Rigid MAVs

| **Descriptions** | **ARQ** | **Quad** | **Units** |
|---|---|---|---|
| Arm length ($L$) | 0.19 | 0.19 | m |
| Size (cage tip to tip) | 0.60 | 0.60 | m |
| Weight w/o battery | 1.034 | 0.844 | kg |
| Weight w/ battery | 1.374 | 1.184 | kg |
| Moments of inertia ($I_{xx}$) | 0.0100 | 0.0092 | $\mathrm{kg} \cdot \mathrm{m}^2$ |
| Moments of inertia ($I_{yy}$) | 0.0116 | 0.0107 | $\mathrm{kg} \cdot \mathrm{m}^2$ |
| Moments of inertia ($I_{zz}$) | 0.0197 | 0.0179 | $\mathrm{kg} \cdot \mathrm{m}^2$ |
| Maximum takeoff weight | 2.787 | 2.857 | kg |
| Maximum payload | 1.38 | 1.64 | kg |
| Thrust to weight ratio | 2.03 | 2.41 | 1 |
| Flight Time (Hover) | 461 | 573 | sec |

Admittedly, using only one sensor for each arm may not allow to measure a collision precisely, unless the direction of collision is exactly aligned with the arm. However, it allows to detect whether the quadrotor is in contact with an obstacle or not, and give an approximation of the collision intensity. By utilizing four Hall effect sensors, the quadrotor

can approximate where the collision occurs in the body frame. We elaborate on the collision detection and compliance characterization in Sec. 2.4. Collision detection accuracy and limitations of various sensors including Hall effect and others reported in the literature are discussed in Sec. 2.6.

We prototype a impact-resilient robot featuring the novel compliant arms (Fig. 2.3b). The platform integrates an Arm-based multi-core processor (Odroid XU4 2Ghz) running high-level computing tasks. A flight controller (Pixhawk 4 Mini) is adopted for the open-source autopilot system (PX4). A lightweight microcontroller (Arduino Nano) is used for analog to digital conversion for Hall effect sensor data processing.

The free length of compliant arms measures 0.19 m and protective cages have a radius of 0.11 m, thus the robot measures 0.6 m from the cage tip to tip. The robot weighs 1.034 kg without the battery and has a flight time 461 sec (7.68 min) with a 5200 mAh LiPo battery.The flight time is measured using the battery range (10.20 to 12.15 V) recommended by PX4 firmware for 3-cell LiPo batteries. Key features of the robot are reported in Tab. 2.2. Note that the moment of inertial matrix is obtained in SOLIDWORKS after weighing all parts individually, as in [147].

## 2.3 Dynamics Modeling

### 2.3.1 Rigid MAV Modeling

Based on assumption (5) and experimental validation in Sec. 2.6, we model the compliant robot as a single rigid body in free flight with a total mass $m = m_b + 4m_a$. Note based on assumption (4), all rigid bodies share the same orientation and angular velocity,

thus $\omega$ and $q$ in Tab. 2.1 are independent of index $j$. Since the robot is represented by a single rigid body, the position, velocity and their derivatives share the same values (e.g., $\boldsymbol{p}_b = \boldsymbol{p}_1 = \boldsymbol{p}_2 = \boldsymbol{p}_3 = \boldsymbol{p}_4$). For simplicity, we drop the index for $\boldsymbol{p}$ and $\boldsymbol{v}$. Equations of motion are derived using the Newton-Euler formulation as

$$\begin{aligned} \dot{\boldsymbol{p}} &= \boldsymbol{v} \\ m\dot{\boldsymbol{v}} &= f_T \boldsymbol{R} e_z - mge_Z \\ \dot{\boldsymbol{R}} &= \boldsymbol{R}\hat{\boldsymbol{\omega}} \\ \boldsymbol{I}\dot{\boldsymbol{\omega}} + \boldsymbol{\omega} \times \boldsymbol{I}\boldsymbol{\omega} = \boldsymbol{\tau} &= \begin{bmatrix} \tau_\phi \\ \tau_\theta \\ \tau_\psi \end{bmatrix} \end{aligned} \tag{2.1}$$

where the operator $\times$ denotes cross product. The hat map $\hat{\cdot} : \mathbb{R}^3 \to \mathsf{SO(3)}$ is defined such that if $\boldsymbol{a}, \boldsymbol{b} \in \mathbb{R}^3, \boldsymbol{a} \times \boldsymbol{b} = \hat{\boldsymbol{a}}\boldsymbol{b}$. Since the robot uses the $\mathsf{X}$ configuration (Fig. 2.2), we can find $f_T$ and $\boldsymbol{M}$ as

$$\begin{bmatrix} f_T \\ \tau_\phi \\ \tau_\theta \\ \tau_\psi \end{bmatrix} = \begin{bmatrix} 1 & 1 & 1 & 1 \\ L^\star & -L^\star & -L^\star & L^\star \\ -L^\star & -L^\star & L^\star & L^\star \\ -c_\tau & c_\tau & -c_\tau & c_\tau \end{bmatrix} \begin{bmatrix} f_{T,1} \\ f_{T,2} \\ f_{T,3} \\ f_{T,4} \end{bmatrix}, \tag{2.2}$$

where $L^\star = L/\sqrt{2}$, and $c_\tau$ is the constant moment coefficient.

### 2.3.2 Compliant MAV Modeling

According to assumption (3), the system includes multiple rigid bodies under contact. In order to eliminate internal reaction forces, we study the dynamics modeling

using the Euler-Lagrange method. Equations of motion are similar to prior work [23], with the additional inclusion of compliance and impact terms. We use Euler angles to represent the orientation of the robot as $\boldsymbol{\eta} = [\phi, \theta, \psi]^T$ for roll, pitch and yaw angles, respectively. We also define a vector of the length of compliant arms $\boldsymbol{l} = [l_1, l_2, l_3, l_4]^T \in \mathbb{R}^4$. Note the derivative $\dot{\boldsymbol{l}} = [\dot{l}_1, \dot{l}_2, \dot{l}_3, \dot{l}_4]$ represents velocities of arm length changes in body frame. Similarly, we drop subscript $b$ for position $p$ and velocity $v$ of the main body for clarity of presentation. Then we can write the generalized coordinates in a vector $\mathcal{Q} \in \mathbb{R}^{10}$,

$$\mathcal{Q} = [\boldsymbol{p}, \boldsymbol{\eta}, \boldsymbol{l}]^T = [x, y, z, \phi, \theta, \psi, l_1, l_2, l_3, l_4]^T \ . \tag{2.3}$$

The Lagrangian $\mathcal{L}$ is calculated by the difference between kinetic $\mathcal{T}$ and potential $\mathcal{U}$ energy, that is

$$\mathcal{L}(\mathcal{Q}, \dot{\mathcal{Q}}) = \mathcal{T} - \mathcal{U} \ . \tag{2.4}$$

The kinetic energy of the system includes both translational $\mathcal{T}_T$ and rotational $\mathcal{T}_R$ motion of all rigid bodies. We have

$$\begin{aligned}
\boldsymbol{p}_j &= \boldsymbol{p} + l_j \boldsymbol{R} \boldsymbol{e}_j \\
\boldsymbol{v}_j &= \boldsymbol{v} + \dot{l}_j \boldsymbol{R} \boldsymbol{e}_j + l_j \boldsymbol{R} \hat{\boldsymbol{\omega}} \boldsymbol{e}_j \\
\mathcal{T}_T &= \frac{1}{2} m_b \boldsymbol{v}^T \boldsymbol{v} + \frac{m_a}{2} \sum_{i=1}^{4} \boldsymbol{v}_i^T \boldsymbol{v}_i \\
\mathcal{T}_R &= \frac{1}{2} \boldsymbol{\omega}^T \boldsymbol{I} \boldsymbol{\omega} \\
\mathcal{T} &= \mathcal{T}_T + \mathcal{T}_R
\end{aligned} \tag{2.5}$$

Note that the moment of inertia matrix $\boldsymbol{I}$ of compliant MAVs is dependent on $l$ (estimated via Hall-effect sensor readings).

There are two core contributions to the potential energy $\mathcal{U}$ in the system: masses contribute gravitational potential energy, and elastic springs add stored energy. We adopt

the Kelvin-Voigt (KV) model for compliant arms as in [27, 207]. Thus, we can write the arm compressing forces as

$$f_L = k_l \delta_L + b_l \dot{\delta}_L \tag{2.6}$$

where $\delta_L$ denotes the arm length changes in body frame, and $k_l$ and $b_l$ stand for the spring and damping coefficients, respectively. Then the potential energy $\mathcal{U}$ can be found as

$$\begin{aligned} z_j &= \boldsymbol{p}_j^T \boldsymbol{e}_Z \\ \mathcal{U} &= m_b g z + m_a g \sum_{i=1}^{4} z_i + \frac{1}{2} k_l \sum_{i=1}^{4} (L - l_i)^2 \ . \end{aligned} \tag{2.7}$$

We use $\boldsymbol{F}_{\text{ext}} \in \mathbb{R}^{10}$ to denote the generalized external force. Then, we can write the Euler-Lagrange equations as

$$\frac{\mathrm{d}}{\mathrm{d}t}\left(\frac{\partial \mathcal{L}}{\partial \dot{\mathcal{Q}}}\right) - \left(\frac{\partial \mathcal{L}}{\partial \mathcal{Q}}\right) = \boldsymbol{F}_{\text{ext}} = \frac{\partial}{\partial \dot{\mathcal{Q}}} \mathcal{P}_{\text{ext}} \tag{2.8}$$

Note that $\mathcal{P}_{\text{ext}}$ is the power generated by external forces. We can split $\mathcal{P}_{\text{ext}}$ into three parts: $\mathcal{P}_{\text{rigid}}$, $\mathcal{P}_{\text{arm}}$ and $\mathcal{P}_{\text{contact}}$. As in rigid MAVs [23], $\mathcal{P}_{\text{rigid}}$ consists of the force and torque generated by motors,

$$\mathcal{P}_{\text{rigid}} = [0, 0, f_T] \cdot \boldsymbol{v} + \boldsymbol{\tau}^T \boldsymbol{\omega} \tag{2.9}$$

where $f_T$ and $\boldsymbol{\tau}$ can be calculated similar to (2.2) as

$$\begin{bmatrix} f_T \\ \tau_\phi \\ \tau_\theta \\ \tau_\psi \end{bmatrix} = \begin{bmatrix} 1 & 1 & 1 & 1 \\ l_1^\star & -l_2^\star & -l_3^\star & l_4^\star \\ -l_1^\star & -l_2^\star & l_3^\star & l_4^\star \\ -c_\tau & c_\tau & -c_\tau & c_\tau \end{bmatrix} \begin{bmatrix} f_{T,1} \\ f_{T,2} \\ f_{T,3} \\ f_{T,4} \end{bmatrix} \tag{2.10}$$

with $l_j^\star = l_j/\sqrt{2}$, and $c_\tau$ the same as in (2.2). Using the Rayleigh dissipation function, we can write $\mathcal{P}_{\text{arm}}$ as

$$\mathcal{P}_{\text{arm}} = \frac{1}{2} b_l \sum_{i=1}^{4} \dot{l}_i^2 \ . \tag{2.11}$$

Note that we ignore the friction of the prismatic joints, therefore $\mathcal{P}_{\text{arm}}$ only includes springs along compliant arms.

Lastly, we study the power of contact force $\mathcal{P}_{\text{contact}}$. The obstacle is assumed to be a vertical wall perpendicular to the $\boldsymbol{e}_X$. Details about obstacles and generating contact forces will be elaborated in the next subsection. Here we summarize that there are $\boldsymbol{f}_n, \boldsymbol{f}_f \in \mathbb{R}^3$ in inertial frame, which represent normal and frictional forces generated by the contact (Fig. 2.2). Then we can calculate $\mathcal{P}_{\text{contact}}$ as

$$\begin{aligned} \mathcal{P}_{\text{contact}} &= \boldsymbol{f}_f \cdot (\boldsymbol{v}_c^T \boldsymbol{e}_Z) - \boldsymbol{f}_n \cdot (\boldsymbol{v}_c^T \boldsymbol{e}_X) \\ \mathcal{P}_{\text{ext}} &= \mathcal{P}_{\text{rigid}} + \mathcal{P}_{\text{arm}} + \mathcal{P}_{\text{contact}} \end{aligned} \tag{2.12}$$

### 2.3.3 Impact Modeling

Compared to the discrete impact model (impulse momentum principle), continuous impact models have the advantage of accounting for energy dissipation and contact with nonrigid surfaces [1]. We adopt the Kelvin-Voigt (KV) model for compliant arms as in [27, 207], while we use the Hunt and Crossley (HC) model [75] for partially elastic impact as in [29, 41]. HC model resolves the nonzero contact force problem of KV model at the start and end of the impact [1].

In this paper, we consider the obstacle to be a vertical wall perpendicular to the $e_X$ with a known distance $D$, similar to [29]. This selection simplifies the problem, however, our method can be extended to other obstacles by taking geometric constraints into account [41].

Experimental observations indicate that the robot has two types of collisions with a vertical wall: single arm and two arms in contact. The former is studied in detail next, and the latter can be achieved by directly extending the first case.

From assumption (2), the cages retain their shape during impact, thus the contact point $\boldsymbol{p}_{c,j}$ lies on the cage circle along arm $j$, and collinear with $\boldsymbol{e}_X$. The contact geometric elements of the robot with one arm in contact are shown in Fig. 2.4.

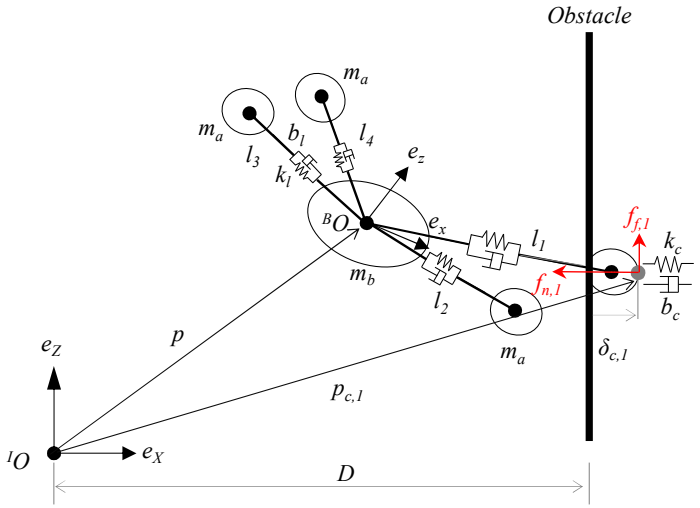


Figure 2.4: Contact geometry elements for a sample impact scenario at arm $j = 1$. The obstacle is a vertical wall perpendicular to the $\boldsymbol{e}_X$ at a known distance $D$. The contact point $\boldsymbol{p}_{c,1}$ lies on the cage circle along arm, and collinear with $\boldsymbol{e}_X$. The normal force $\boldsymbol{f}_{n,1}$ and frictional force $\boldsymbol{f}_{f,1}$ generated by contact in inertial frame are plotted in red.

To study the contact model, we need to find out the location and velocity of the contact point $\boldsymbol{p}_{c,j}$ along arm $j$ in inertial frame. The protective cage has a constant radius $r_0$, thus the contact point can be found by projecting the vector $r_0\boldsymbol{e}_j$ in body frame onto the $\boldsymbol{e}_X$ axis of the inertial frame.

$$
\begin{aligned}
\boldsymbol{p}_{c,j} &= \boldsymbol{p}_j + \Big((r_0 \boldsymbol{R} \boldsymbol{e}_j)^T \boldsymbol{e}_X\Big)\boldsymbol{e}_X \\
\boldsymbol{v}_{c,j} &= \boldsymbol{v}_j + r_0\Big(\boldsymbol{e}_j^T\Big(\frac{\mathrm{d}}{\mathrm{d}t}\boldsymbol{R}^T\Big)\boldsymbol{e}_X\Big)\boldsymbol{e}_X \\
\frac{\mathrm{d}}{\mathrm{d}t}\boldsymbol{R}^T &= \frac{\mathrm{d}}{\mathrm{d}t}\boldsymbol{R}^{-1} = -\boldsymbol{R}^T \boldsymbol{R}\hat{\boldsymbol{\omega}}\boldsymbol{R}^T
\end{aligned}
\tag{2.13}
$$

where $\boldsymbol{p}_j$ and $\boldsymbol{v}_j$ can be found using the (2.5). We compute the normal and tangential components of $\boldsymbol{v}_{c,j}$ in inertial frame as

$$
\begin{aligned}
\boldsymbol{v}_{c,j}^n &= (\boldsymbol{v}_{c,j}^T \boldsymbol{e}_X)\boldsymbol{e}_X \\
\boldsymbol{v}_{c,j}^t &= (\boldsymbol{v}_{c,j}^T \boldsymbol{e}_Z)\boldsymbol{e}_Z
\end{aligned}
\tag{2.14}
$$

Based on the HC model [75], the normal force $\boldsymbol{f}_{n,j}$ and frictional force $\boldsymbol{f}_{f,j}$ generated by contact on arm $j$ in inertial frame are modeled as

$$
\begin{aligned}
\boldsymbol{f}_{n,j} &= \begin{cases} \boldsymbol{0} & \text{for } \delta_{L,j} < 0 \\ k_c \delta_{L,j}^n - b_c \delta_{L,j}^n \dot{\delta}_{L,j} & \text{for } \delta_{L,j} \geq 0 \end{cases} \\
\boldsymbol{f}_{f,j} &= -\mu \boldsymbol{f}_{n,j} \frac{\boldsymbol{v}_{c,j}^t}{||\boldsymbol{v}_{c,j}^t||}
\end{aligned}
\tag{2.15}
$$

where $\delta_{L,j} = \boldsymbol{p}_{c,j}^T \boldsymbol{e}_X - D$, and $\dot{\delta}_{L,j} = \boldsymbol{v}_{c,j}^n$. Note that the constant $\mu$ denotes the coefficient of kinetic friction. Using (2.12), we can calculate the power of contact force if only arm $j$ collides with the wall.

For the two arms case, we can repeat (2.13) to (2.15) and calculate the velocities of the contact point $v_j$, as well as normal and frictional forces, respectively. For instance, if arms 1 and 2 are in contact, we can rewrite (2.12) as

$$
\begin{aligned}
\mathcal{P}_{\text{contact, j}} &= \boldsymbol{f}_{f,j} \cdot (\boldsymbol{v}_{c,j}^T \boldsymbol{e}_Z) - \boldsymbol{f}_{n,j} \cdot (\boldsymbol{v}_{c,j}^T \boldsymbol{e}_X) \\
\mathcal{P}_{\text{contact}} &= \mathcal{P}_{\text{contact, 1}} + \mathcal{P}_{\text{contact, 2}}
\end{aligned}
\tag{2.16}
$$

## 2.4 Collision Characterization and Compliance Estimation

Similar to our prior work [110], we utilize Hall effect sensors to detect collisions, while measuring arm length and estimating the moment of inertia. The Hall sensor used herein outputs a voltage proportional to the magnetic field strength through it. We fix a magnet at one side of the shock absorber and place the Hall sensor at the other end (see Fig. 2.3a). When a collision happens, the contact force will shorten the compliant arm, thereby reducing the distance between the Hall effect sensor and the magnet, thus increasing the output voltage recorded in the micro-controller.

### 2.4.1 Sensor Fusion and Impact Detection

Taking advantage of the Hall effect sensors, the robot can measure compliant arms length rapidly. Based on that, we propose a heuristic-like unit-less scalar value $h_j \in [0, 1]$ on arm $j$ to describe the sensor readings. The value $h_j$ is calculated following a continuous uniform distribution, where $h_j = 0$ denotes the longest arm ($l_j = L$), and $h_j = 1$ stands for the minimum arm length ($l_j = l_{min}$).

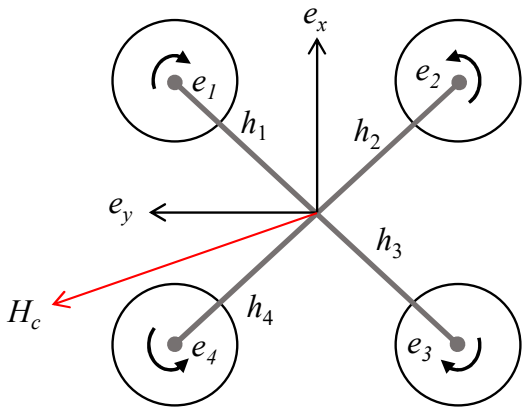


Figure 2.5: Impact characterization in the body frame by fusing data from Hall effect sensors.

Figure 2.5 illustrates how the robot fuses the readings from sensors on each arm. The contact from sensors $\boldsymbol{H}_c \in \mathbb{R}^3$ in the body frame is found by fusing all readings following the geometric relations $\boldsymbol{H}_c = \sum_{i=1}^{4} h_i \boldsymbol{e}_i$.

Similar to IMU-based methods, the robot uses an empirically-selected threshold on the norm of $\boldsymbol{H}_c$ to report impact. Specifically, the robot reports collision whenever $||\boldsymbol{H}_c|| \geq 0.1$. An experimental study on collision detection performance is detailed in Sec. 2.6.

### 2.4.2 Compliance Estimation

Hall effect sensors are also utilized to measure exact arm length and estimate the robot compliance under the contact. Despite the relatively small changes in the robot's shape and the short period of time during the impact, the ability to measure arm length accurately and rapidly can assist precise model-based control of compliant MAVs under contact.

The compliance estimation in this part is twofold: 1) measuring arm length in real time and 2) updating the moment of inertia matrix accordingly. We study the relation between arm length $l_j$ with the sensor reading $h_j$ along arm $j$ by model fitting based on experimental data. Motion capture is used to track the position of the two ends of the arm, while the robot records the arm length and Hall sensor readings in real time.

Experimental data of arm length $l_1$ and Hall sensor readings $h_1$ are shown in Fig. 2.6. Note that all arms are assumed to share the same relation, thus only arm $j = 1$ is studied here. The arm length $l_1$ shortens from the free length $L = 0.19$ m to its minimum

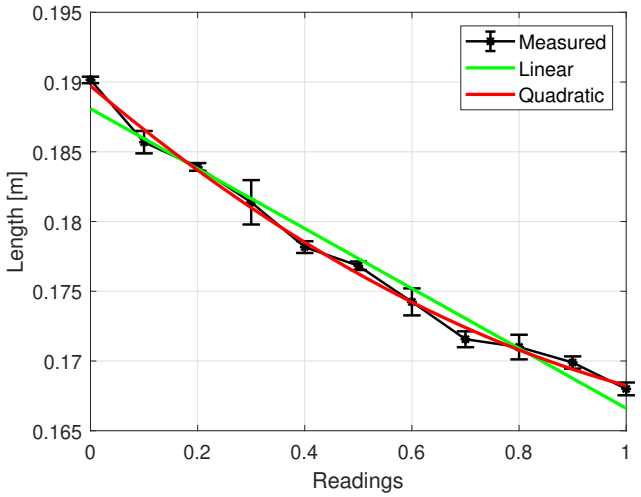


Figure 2.6: Relations between Hall effect sensor readings and arm length.

$l_{\min} = 0.168$ m. Two fitting models (linear, quadratic) are tested and visualized in two colors. We observe the quadratic fitting model has higher $R^2$ value compared to linear fit, $R^2_{\text{quadratic}} = 0.9948 > R^2_{\text{linear}} = 0.9753$. The relation between arm length $l_j$ with the sensor reading $h_j$ then is

$$l_j = 0.0109h_j^2 - 0.0324h_j + 0.1897 \quad \text{for } h_j \in [0,1] \ . \tag{2.17}$$

To study the moment of inertial matrix, we approximate arm rigid bodies by particles with a mass $m_a$, due to much smaller sizes and regular shapes. Given an arm length vector $\boldsymbol{l} = [l_1, l_2, l_3, l_4]^T$, we first define a map $\mathcal{I} : \mathbb{R}^4 \to \mathbb{R}^{3\times 3}$ as

$$\mathcal{I}(\boldsymbol{l}) = \sum_{i=1}^{4} \begin{bmatrix} m_a l_i^2/2 & & \\ & m_a l_i^2/2 & \\ & & m_a l_i^2 \end{bmatrix} \ . \tag{2.18}$$

We can find the moment of inertia matrix for the main body $\boldsymbol{I}_b = \boldsymbol{I}_0 - \mathcal{I}(l_L)$, where $\boldsymbol{I}_0 = \text{diag}(I_{xx},\ I_{yy},\ I_{zz})$ in Tab. 2.2 on ARQ and $\boldsymbol{l}_L = [L, L, L, L]^T$. The updated moment of inertial matrix based on variable arm lengths $\boldsymbol{I}$ is

$$\boldsymbol{I} = \boldsymbol{I}_b + \mathcal{I}(\boldsymbol{l}) \ . \tag{2.19}$$

## 2.5 Tracking Control and Collision Handling

In order to stabilize high-speed and large-angle collisions, the tracking control of the robot must be able to follow aggressive trajectories with large Euler angles. In this work, we adopt the cascaded tracking control method as in our prior work [110]. Note that only the rigid MAV modeling is utilized for the tracking control to simplify the problem. However, experimental results in Sec. 2.6 demonstrate that the same nonlinear tracking controller is appropriate for compliant robots to achieve solid performance in both free flight and after collision recovery, thanks to the proposed novel design.

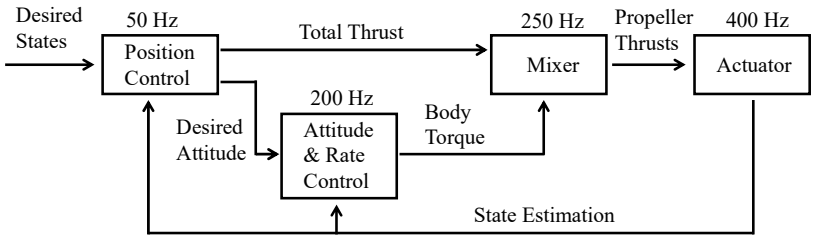


Figure 2.7: Cascaded tracking control used in this work for both free flight and stabilizing high-speed and large-angle collisions.

We employ a cascaded tracking control in this work (Fig. 2.7). Specifically, the planner generates desired states, including the desired position $p_{\text{des}}$, desired velocity $v_{\text{des}}$, desired acceleration $a_{\text{des}}$ and desired yaw angle $\psi_{\text{des}}$. Tracking control comprises high-level position control, mid-level attitude and bodyrate control, and a low-level mixer to output PWM signals to actuators. Readers are referred to the PX4 firmware [126] for details about the PID bodyrate control and mixer.

### 2.5.1 Tracking Control

The position controller takes advantages of geometric constraints for nonlinear tracking as in [104, 127, 202]. The controller reads estimated current states $(p, v, \psi)$ and desired states $(\boldsymbol{p}_{\text{des}}, \boldsymbol{v}_{\text{des}}, \ \boldsymbol{a}_{\text{des}}, \psi_{\text{des}})$, and outputs the desired total thrust $f_{\text{T, des}} \in \mathbb{R}$ and desired attitude $\boldsymbol{R}_{\text{des}} \in \mathsf{SO(3)}$. Note that the tracking control in this work differs from prior work [104] in the sense that the controller outputs desired attitude to the nonlinear attitude and bodyrate controllers, instead of direct thrust forces on each motors. The method adopted in this work to output bodyrate is more robust to modeling errors [60]. Computation of desired attitude is similar to [127], which is the simplified version of the controller in [104]. Readers may refer to [104] for a thorough analysis. First we find the desired thrust force vector $\boldsymbol{F}_{\text{des}} \in \mathbb{R}^3$ in the inertial frame

$$\boldsymbol{F}_{\text{des}} = -\boldsymbol{K}_d(\boldsymbol{v} - \boldsymbol{v}_{\text{des}}) - \boldsymbol{K}_p(\boldsymbol{p} - \boldsymbol{p}_{\text{des}}) + m\boldsymbol{a}_{\text{des}} + mg\boldsymbol{e}_Z \tag{2.20}$$

where $\boldsymbol{K}_d, \boldsymbol{K}_p \in \mathbb{R}^{3\times3}$ are diagonal, positive definite tuning matrices. Then we can calculate the desired total thrust $f_{\text{T, des}}$ in body frame as

$$f_{\text{T, des}} = \boldsymbol{F}_{\text{des}}^T \cdot \boldsymbol{e}_z = \boldsymbol{F}_{\text{des}}^T \cdot (\boldsymbol{R}^T \boldsymbol{e}_Z) \ . \tag{2.21}$$

Given that the MAV can only produce thrust along the $\boldsymbol{e}_z$ axis, we align $\boldsymbol{e}_{z,\text{des}}$ with $\boldsymbol{F}_{\text{des}}$, and align $\boldsymbol{e}_{y,\text{des}}$ to match the desired yaw $\psi_{\text{des}}$. Therefore, we can calculate the desired attitude $\boldsymbol{R}_{\text{des}}$ as

$$
\begin{aligned}
\boldsymbol{e}_{z,\text{des}} =& \frac{\boldsymbol{F}_{\text{des}}}{||\boldsymbol{F}_{\text{des}}||} \\
\boldsymbol{a}_{\psi} =& [\cos\psi_{\text{des}},\ \sin\psi_{\text{des}},\ 0]^T \\
\boldsymbol{e}_{y,\text{des}} =& \frac{\boldsymbol{e}_{z,\text{des}} \times \boldsymbol{a}_{\psi}}{||\boldsymbol{e}_{z,\text{des}} \times \boldsymbol{a}_{\psi}||} \\
\boldsymbol{R}_{\text{des}} =& [\boldsymbol{e}_{y,\text{des}} \times \boldsymbol{e}_{z,\text{des}},\ \boldsymbol{e}_{y,\text{des}},\ \boldsymbol{e}_{z,\text{des}}]
\end{aligned}
\tag{2.22}
$$

where the operator $\times$ denotes the cross product. Note that the singularity exists when calculating $\boldsymbol{e}_{y,\text{des}}$. Readers are referred to [202] to address the singularity problem.

We adopt a nonlinear attitude controller based on quaternion as in [19]. Note that we convert the rotation matrix $\boldsymbol{R}_{\text{des}}$ to the quaternion $\boldsymbol{q}_{\text{des}} \in \mathbb{R}^4$ to describe the desired attitude. The controller reads the estimated current attitude $\boldsymbol{q}$ and the desired attitude $\boldsymbol{q}_{\text{des}}$, and outputs the desired angular velocity $\boldsymbol{\omega}_{\text{des}}$. We summarize the results here, and readers are referred to the report [19] for a thorough analysis. We have

$$
\begin{aligned}
\boldsymbol{q}_e =& \boldsymbol{q}^{-1} \cdot \boldsymbol{q}_{\text{des}} \\
\boldsymbol{\omega}_{\text{des}} =& \frac{2}{\gamma} \text{sgn}(q_{e,0}) \cdot [q_{e,1},\ q_{e,2},\ q_{e,3}]^T \\
\text{sgn}(q_{e,0}) =& \begin{cases} 1 & \text{for } q_{e,0} \geq 0 \\ -1 & \text{for } q_{e,0} < 0 \end{cases}
\end{aligned}
\tag{2.23}
$$

where $\gamma$ is the first-order system time constant with a unit second, and $\boldsymbol{q}_e = [q_{e,0},\ q_{e,1},\ q_{e,2},\ q_{e,3}]^T$.

Bodyrate $\boldsymbol{\omega}_{\text{des}}$ are sent to the low-level PID bodyrate controller, which outputs the desired body torques. The mixer reads the desired total thrust $f_{\text{T, des}}$ and the desired body torques, and outputs direct control signals to the actuators.

### 2.5.2 Collision Handling

As mentioned in the Sec. 2.1, most existing works on MAV collision recovery are limited to small contact angles near hovering states. Notable exceptions include [40, 41] where a constant pitch angle is tracked by the attitude controller to stabilize large-angle collisions. To this end, this paper adopts an effective and intuitive recovery method that generates and tracks similar but more aggressive trajectories. Experimental results in Sec. 2.6 validate our recovery method as both rigid and compliant robots can stabilize collisions with larger contact angles compared to prior work [40, 41].

Collision handling to drive the robot to a safe position post collisions is based on [110, 205]. The recovery setpoint $p_{r,\text{des}}$ the inertial frame can be found as

$$\boldsymbol{p}_{r,\text{des}} = \boldsymbol{p}_c - \delta R \boldsymbol{H}_c \tag{2.24}$$

where $\delta \in \mathbb{R}$ is a user-defined coefficient that can be tuned empirically. The robot generates a minimum-snap trajectory for a smooth path to reach the setpoint [127, 159]. We follow the same optimization formulation with constraints to generate the trajectory to reach the setpoint and stop as in [110].

## 2.6 Experimental Results

To fully study the free flight performance and impact resilience of ARQ, we built another rigid robot termed herein as Quad. Perspective views of both ARQ and Quad prototypes are shown in Fig. 2.8. Key features of Quad are also listed in Table 2.2.

(a) ARQ (b) Quad

Figure 2.8: Our prototype of compliant (a) and rigid (b) robots. The robots share almost the same configuration except for their arms. Both robots measure 0.60 m from the cage tip to tip and 0.38 m from the motor tip to tip.

### 2.6.1 Model Validation

In this test, we fix both the rigid and compliant robots on a custom-made testbed with a linear slider that allows for horizontal-only (i.e. along the $\boldsymbol{e}_X$ direction) motion. As this part only focuses on the passive response to collisions, motors on both robots are not actuated during the tests. We examine collisions with two types of surfaces: rigid walls and soft mats. Motion capture at 200 Hz is utilized to measure positions and velocities of both the main body and arm. The distance $D$ of the obstacle is fixed and known before collisions ($D = 1.0$ m). Ten repeated tests are conducted for each collision type for each robot.

Table 2.3: Key Parameters of Model Validation Study

| $m_b$ | $m_a$ | $m_{\text{rigid}}$ | $\mu$ |
|---|---|---|---|
| 1.882 kg | 0.2 kg | 1.892 kg | 0.8 |
| $k_l$ | $b_l$ | $k_{c,\text{wall}}$ | $k_{c,\text{mat}}$ |
| $5 \times 10^3$ N/m | 90 Ns/m | $2 \times 10^5$ N/m | $1.2 \times 10^5$ N/m |

In this study, we only focus on the short period of time during which robots are in contact with obstacles. Thus, we ignore the friction of the slider. Both robots are manually

accelerated to velocities around 1.85 m/s right before collision with a zero contact angle $\theta = 0$. Note that the masses of both robots in this test also include the weight of the sliding bar. Several key parameters and their values are listed in Table 2.3. Similar to the related work [207], we set the order of the impact model $n = 1.5$ and damping coefficient $b_c = 1.5 \cdot c_a \cdot k_c$, where $c_a$ is usually between 0.01 - 0.5 depending on the materials and impact velocity.

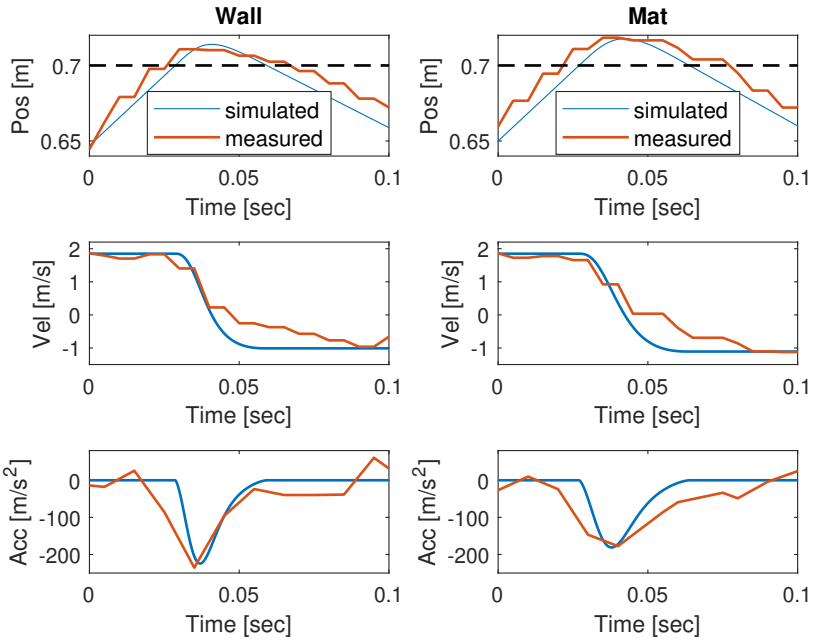


Figure 2.9: Positions, velocities and accelerations of the rigid robot (QUAD) in collisions with both rigid walls and soft mats.

Results of Quad colliding with rigid walls and soft mats are shown in Fig. 2.9. Positions, velocities and accelerations are shown in blue and red curves to describe results in simulation and physical tests, respectively. The black dashed lines are used to denote the position when the robot is in contact with obstacles. Note that the collision positions are different in the mat tests due to the thickness of mats, however, they are re-aligned to match those in the rigid wall tests. Deformation is observed in both cases with $\delta_{\text{wall}} = 14$ mm

and $\delta_{\text{mat}} = 18$ mm. We also observe very short contact time as $\text{dt}_{\text{wall}} = 0.031$ sec and $\text{dt}_{\text{mat}} = 0.037$ sec.

Despite the discontinuity in the measured data due to the frequency limitation of the motion capture, simulated results still fit the physical experimental data well. We list the coefficient of restitution (COR) and maximum absolute accelerations $a_{\max}$ of both simulated and physical tests in Table 2.4. COR is computed as the ratio of the absolute post velocity over the absolute prior one ($\text{COR} = |v_{\text{after}}|/|v_{\text{before}}|$). Based on the results, we conclude that the adopted continuous impact models can describe collisions with various surfaces well. However, we observe large impact for the rigid robot, especially in collisions with rigid walls ($a_{\max} = 235$ m/s$^2$), which may damage sensitive electronic components.

Table 2.4: Rigid and Compliant Robots Impact Study

| | Quad | | | | ARQ | | | |
|---|---|---|---|---|---|---|---|---|
| | Simulation | | Physical Test | | Simulation | | Physical Test | |
| | Wall | Mat | Wall | Mat | Wall | Mat | Wall | Mat |
| COR | 0.547 | 0.598 | 0.526 | 0.603 | 0.444 | 0.498 | 0.451 | 0.504 |
| $a_{\max}$ [m/s$^2$] | 224 | 168 | 235 | 177 | 144 | 137 | 146 | 142 |

Results from ARQ impact experiments with rigid walls and soft mats in both simulation and physical tests are shown in Fig. 2.10. Besides positions, velocities and accelerations of the main body, the length of the compliant arms are also included in the figure. Due to the compliant arms, larger deformation is observed for collisions with both surfaces ($\delta_{\text{wall}} = 29$ mm, $\delta_{\text{mat}} = 33$ mm). A longer contact time is also observed for compliant robot collisions as $\text{dt}_{\text{wall}} = 0.079$ sec and $\text{dt}_{\text{mat}} = 0.083$ sec. Despite noise in measured curves, simulated results generally fit those from physical tests well, including the

compliant arm length changes. Results validate the proposed model for compliant MAVs under contact.

The COR and maximum absolute accelerations of the compliant robot are also listed in Table 2.4. Simulated results again match the physical ones well. Compared to Quad, the compliant robot has smaller COR and $a_{\max}$, owing to the impact reduction afforded by the compliant arms. Moreover, smaller differences on both COR and $a_{\max}$ between different surfaces are observed, due to the presence of compliant arms.

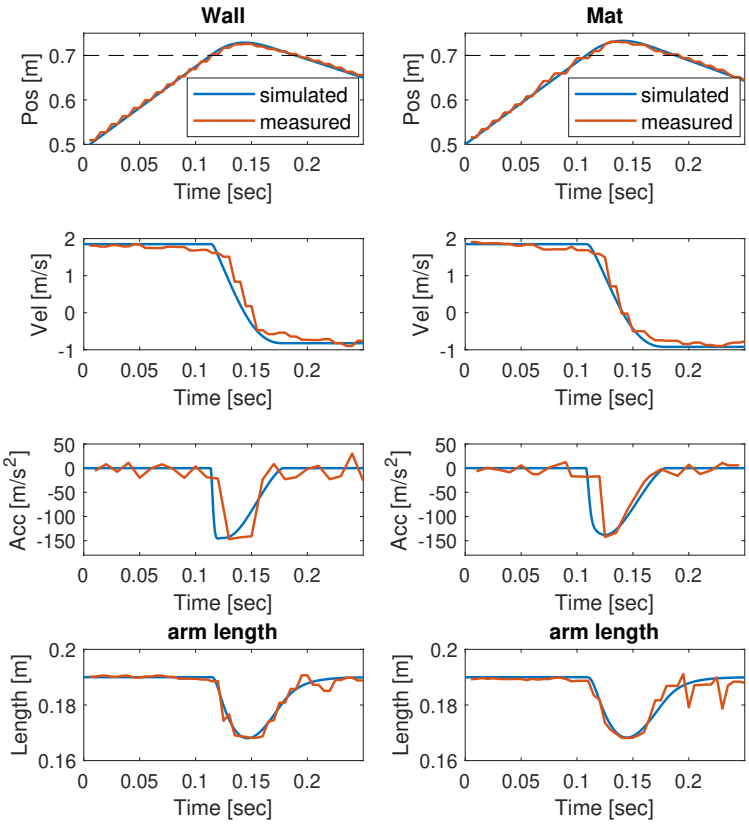


Figure 2.10: The states of the compliant robot's (ARQ) main body, as well as arm length, in collisions with both rigid walls and soft mats.

We notice that maximum absolute accelerations $a_{\max}$ are dependent on the contact velocity. We conduct additional simulated tests to record the maximum absolute acceler-

ations for both rigid and compliant robots in collision with rigid walls. Parameters in the simulation are the same to those in the study above, with one exception that we only include the masses of the robots (without the weight of the sliding bar).

Figure 2.11 visualizes the simulated results with collision speeds ranging from 1 m/s to 6 m/s. Blue bars denote the maximum absolute accelerations of the compliant robot while the red bars represent those of the rigid MAV. We also use yellow bars to visualize differences between compliant and rigid robots. Simulated results support our claim that the compliant arms play a big role in reducing the impact to the main body under high-speed contact, as we see a difference of $\mathrm{d}a_{\max} = 493$ m/s$^2$ or 50.26 G at a speed of 6 m/s.

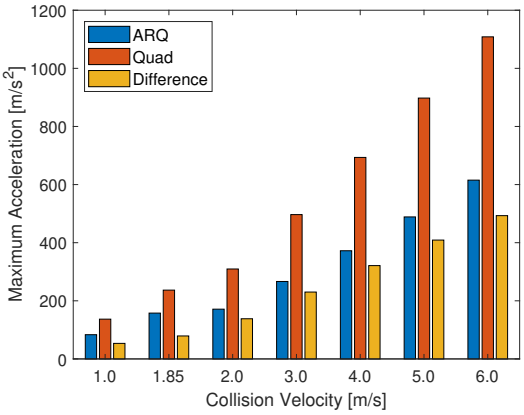


Figure 2.11: Maximum absolute acceleration in extended simulation tests.

### 2.6.2 Impact Resilience

We use a wooden wall as the obstacle (see Fig. 2.1), which has hardness close to rigid walls in the previous test. Both compliant and rigid robots are running the nonlinear tracking controller, and following trajectories generated offline before colliding with two arms in contact. The position of the wall is unknown to the robots before collisions; ground

truth is measured only for reference ($D = 2.75$ m). The compliant robot uses the detection method with Hall effect sensors while the rigid robot utilizes the accelerometer to report collisions. Both robots adopt the same recovery method with a constant distance $L_c = 0.1$ m. Note that the body-fixed frame $\mathcal{F}_B$ is aligned with the inertial frame $\mathcal{F}_I$ ($R = I_3$) before the robot starts collision tests, therefore both robots collide with the obstacle with two arms in contact (Fig. 2.1).

Two velocities (2.0 m/s and 3.5 m/s) are studied with a zero contact angle for both compliant and rigid robots. We also examine collisions at a constant velocity 2.0 m/s but with various pitch angles ($-45°, \pm 30°, \pm 15°$). Ten consecutive experimental trials are implemented for each case for both robots (e.g., Quad at 2 m/s with angle 0°).

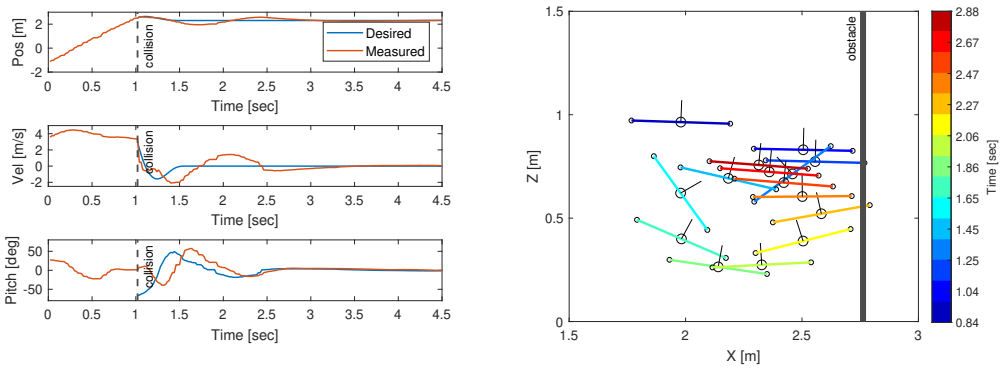


(a) States (b) Orientation

Figure 2.12: (a) States and (b) orientation of the compliant robot in a collision at the speed of 3.5 m/s.

Results show that ARQ can survive collisions and sustain flight at a speed of 3.5 m/s with zero contact angles, at 100% success rates. Composite images of a sample test can be found in Fig. 2.12. States (position $p_x$, velocity $v_x$ and pitch angles $\theta$) of the main body are shown in Fig. 2.12a.

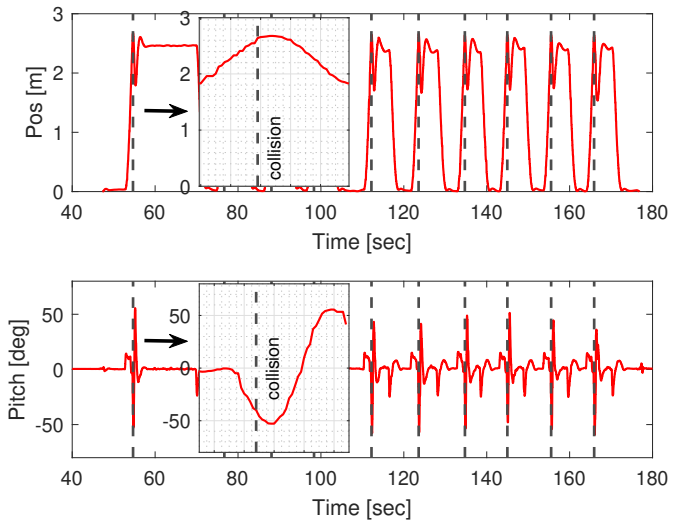


Figure 2.13: Repeated collision tests of the compliant robot with a contact angle of $-45°$. The boxes show detailed (zoomed-in) portions of states (within 1 sec) for the first collision.

We also visualize the projection of the robot's orientation onto the $e_X - e_Z$ plane, where short black lines denote the $e_z$ axis. Black circles in different sizes represent the main body (big) or arms (small). The color scale denotes the temporal duration of the collision recovery process. Note that we use a constant arm projected length $L^\star = L/\sqrt{2}$ to visualize orientation in Fig. 2.12b. Results also show that the collision handling method can generate pitch angle trajectories similar to but more aggressive than [41] (e.g., $-66°, 49°$). Taking advantage of the nonlinear tracking controller, ARQ can follow the aggressive recovery trajectory and stabilize itself rapidly, before hovering stably.

Compliant arms are also observed to make significant contributions to stabilizing from high-speed collisions, with reduced impact and elongated contact time. In comparison, we command the rigid robot to collide at the same speed, however, the robot fails to stabilize and sustain flight for all trials. Owing to the compliant airframe, ARQ has 100% success rates for both high-speed and large-angle collisions. The rigid robot has fairly good

performance within the pitch range $-30°$ to $30°$ at a speed of 2 m/s, however, the success rate drops when the pitch reaches $-45°$. We present the position $p_x$ and pitch $\theta$ values of ten consecutive recovery trials of ARQ with pitch angles $-45°$ in Fig. 2.13. The robot sustains flight and goes to the initial point $[0, 0, 1]^T$ after recovering from large-angle collisions. Then, the robot repeats a collision test without landing. In all, the 100% success rates for stabilizing high-speed and large-angle collisions significantly promote the confidence in deploying ARQ in unknown challenging environments.

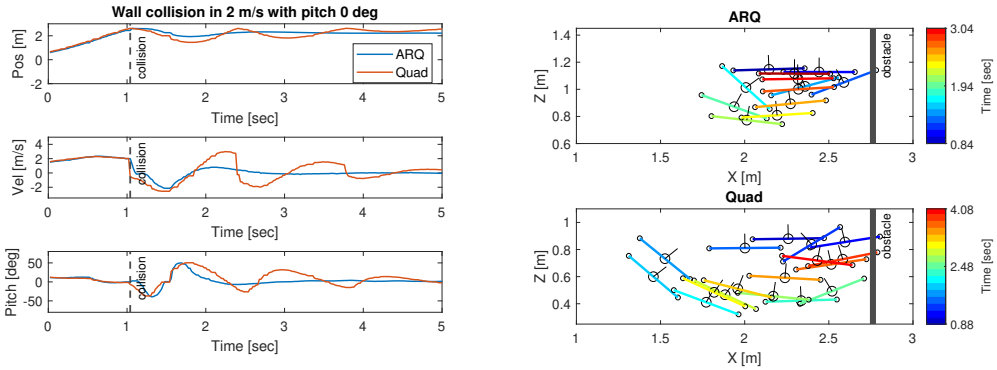


(a) States (b) Orientation

Figure 2.14: Sample states and orientation for the compliant and rigid aerial robots colliding at a speed of 2.0 m/s with zero contact angle.

Figure 2.14a shows measured states (position $p_x$, velocity $v_x$, and pitch $\theta$) of two robots in a sample collision test at a speed of 2 m/s with a $0°$ pitch angle. When a collision happens, the velocity of ARQ declines less sharply, thanks to the impact reduction offered by the compliant airframe. The reduced impact and elongated contact time enable the compliant robot to stabilize itself rapidly, while oscillations occur to the rigid robot, resulting in a longer settling time. Similarly, we present 2D orientation of both compliant and rigid robots after collision in Fig. 2.14b. Results show that the rigid robot swings back

farther compared to ARQ due to larger impact and shorter contact time. Although both robots track large pitch angles to recover, ARQ stabilizes itself much faster.

### 2.6.3 Free Flight

Table 2.5: Comparisons in Step Response and Planar Circle Tracking Tests

Step Response

| | Quad | | | ARQ pre-col | | | ARQ post-col | | |
|---|---|---|---|---|---|---|---|---|---|
| | $p_x$ | $p_y$ | $p_z$ | $p_x$ | $p_y$ | $p_z$ | $p_x$ | $p_y$ | $p_z$ |
| Rising time [sec] | 0.649 | 0.662 | 0.625 | 0.760 | 0.782 | 0.627 | 0.767 | 0.779 | 0.628 |
| MSE [m] | 0.090 | 0.094 | 0.059 | 0.098 | 0.107 | 0.064 | 0.108 | 0.108 | 0.062 |

Planar Circle Tracking (MSE $\times 10^{-3}$)

| | | Quad | | ARQ pre-col | | ARQ post-col | |
|---|---|---|---|---|---|---|---|
| | | $x$ | $y$ | $x$ | $y$ | $x$ | $y$ |
| Slow | Position [m] | 0.88 | 3.80 | 1.10 | 6.10 | 2.00 | 6.20 |
| | Velocity [m/s] | 1.20 | 23.90 | 1.80 | 23.70 | 1.80 | 24.40 |
| Fast | Position [m] | 9.70 | 13.80 | 15.90 | 17.00 | 22.20 | 19.90 |
| | Velocity [m/s] | 46.10 | 100.80 | 74.50 | 99.50 | 95.40 | 102.80 |

This experiment studies the free flight performance of ARQ before or after collisions, in comparison with the rigid robot Quad. Five repeated trials are recorded for each test. Note that the compliant robot is studied before (pre-col) and after (post-col) collisions separately. ARQ undergoes free falls at 1 m before the post-collision free flight performance study (see supplemental video). In the step response test, both robots hover at the point $[0, 0, 1]^T$ before the planner sends discrete setpoints $[0, 0, 2]^T$, $[1, 0, 2]^T$ and $[1, 1, 2]^T$ at 5 sec intervals. Two planar circle trajectories are generated for the second test with periods of $2\pi$ and $\pi$ sec, respectively. Both trajectories have radius of 1 m, and start at $[1, 0, 1]^T$. (Note that positions in both tests are expressed in meters.)

We calculate the rising time and mean squared errors (MSE), which are listed in Table 2.5. Note that the rising time is measured as the time the response takes to rise from 10% to 90% from the initial value to the steady-state one. Compared to the rigid robot, ARQ is observed to have slightly worse but in general very close performance for the step response test, in terms of both rising time and mean squared errors. Meanwhile, pre- and post-collision step response for ARQ closely matches each other.

Similar observations can be made for the planar circle tracking test. Positions and velocities of both robots are tracked well for the slow circle, despite the shared tracking errors resulted from the discontinuity of the desired velocities. Compared to the rigid robot, ARQ is observed to have slightly worse but in general very close performance for the step response test, in terms of both rising time and mean squared errors. However, both rigid and compliant robots are observed to have a minor difference in $x, y$ axis, resulting from the asymmetric hardware design.

## 2.7 Conclusions

In this chapter, we study a novel impact-resilient MAV with passive springs within the compliant arms to reduce impact and protect sensitive electronic devices onboard. The compliant robot is equipped with Hall effect sensors to rapidly detect collision and estimate compliance. Furthermore, this article presents dynamic modeling for both rigid and compliant MAVs, as well as continuous models to estimate impact with various surfaces. Taking advantage of the nonlinear geometric tracking controller, the paper adopts an effective recovery method to generate and track post-impact setpoint to stabilize.

Proposed models and methods are extensively studied in both simulated and physical tests. A conventional rigid robot using the same configuration is fabricated using lightweight carbon fiber sheets to provide a comprehensive comparison between rigid and compliant robots. Free flight tests show that the compliant robot has very close tracking performance compared to the rigid counterpart. In the meantime, collisions have almost no negative effect on free flight performance. Simulated and physical tests of both rigid and compliant robots validate the proposed modeling method for the robot under contact with various surfaces. Results also support our claim that the added compliance can reduce impact and elongate contact time, which are beneficial for rapid post-impact stabilization. Results show that ARQ can stabilize high-speed and large-angle collisions rapidly and sustain post-impact flight. The compliant robot also has 100% success rates for recovering from collisions at speeds of up to 3.5 m/s or with contact angles up to 45°. Detailed comparisons with a rigid robot further demonstrate the role of the compliant airframe to survive collisions.

In the next chapter, we extend the aerial resilience by including an estimator to estimate real-time contact force in presence of compliance. Further, we propose a novel planning method that prioritizes contacts. Extensive simulated and physical tests are conducted to evaluate the planning method in partially-known cluttered environments.

# Chapter 3

# Contact-Prioritized Planning of Compliant Impact-resilient Aerial Robots

In this chapter, we extend the study to address collision-inclusive motion planning of compliant aerial robots. In detail, we present an impact-resilient aerial robot equipped with a compliant arm to sense contacts and reduce collision impact. The robot features a real-time contact force estimator and a non-linear motion controller to handle collisions while performing aggressive maneuvers and stabilize from high-speed wall collisions. Further, a new collision-inclusive planning method that aims to prioritize contacts to facilitate aerial robot navigation in cluttered environments is proposed. A range of simulated and physical experiments demonstrate key benefits of the robot and the contact-prioritized (CP) planner. Results show that the proposed compliant robot and contact-prioritized planning

method can accelerate computation time while having shorter trajectory time and larger clearances compared to A* and sampling-based planners with velocity constraints. Online planning tests in partially-known environments further demonstrate the preliminary feasibility of our method to apply in practical use cases.

This chapter is organized as follows: Section 3.1 discusses background and related works for compliant aerial autonomy, contact force estimation and collision-inclusive planning; Section 3.2 presents the overview of the aerial platform with the integrated compliant contact arm; Section 3.3 summarizes the motion control and the collision handling based on the real-time force estimator. In Section 3.4, we introduce a novel planning method to prioritize contact to facilitate navigation. In Section 3.5, we experimentally study the impact reduction, collision resilience and the contact-inclusive planning in partially-known environments.

## 3.1 Background

Micro Aerial Vehicles (MAVs) can support sensor-based exploration and navigation, and en route to robust autonomous navigation, aerial autonomy with interactive behavior has been studied [12,92,145]. There has been a growing interest in deploying MAVs in challenging environments, including but not limited to confined [37,105] and cluttered [141] ones. Collision risks get significantly higher for autonomous missions in these complex environments. Compliant resilient robots attract growing attention due to the merits of reducing impact and protecting sensors [147]. Research efforts on collision-inclusive motion planning have started to be proposed [114,116,214]. In this work, we introduce a lightweight

compliant arm to sense contacts and reduce high-speed collision impact. Equipped with the integrated compliant arm, we develop an impact-resilient aerial robot (named s-ARQ). The compliant robot has only a 4% weight increase compared to its rigid counterpart, however experimental results show that the compliant arm can reduce around 40% impact. The compliant arm incorporates a passive spring and a laser ranging sensor to enable contact force estimation. Employing a force estimator and non-linear motion controller, s-ARQ can stabilize from high-speed wall collisions at 3.0 m/s with a success rate of 100%. We consolidate the impact resilience by including pole obstacle collisions, as well as different yaw angles. Further, we harness s-ARQ's strong collision resilience capability to propose a novel planning method that prioritizes contacts. Physical tests and extended simulations demonstrate that our proposed compliant robot and contact-prioritized (CP) planner can accelerate computation while achieving shorter trajectory time and larger clearances compared to collision-avoidance methods with velocity constraints. Online planning tests in partially-known environments were studied to support application toward practical use cases. Simulated results further validate the efficiency of the proposed CP planner.

### 3.1.1 Related Work

Several compliant aerial robots have been developed over the years. In Ref [12], an aerial robot with a compliant contact arm was developed. Examples of works integrating compliant protective structure onto the robot include origami-inspired mechanisms [173,186] and an icosahedron tensegrity structure [215]. In Ref [37], an impact-resilient MAVs with external compliant flaps was studied. Compliance has also been included into the robot chassis to reduce impact. In Ref [26], a collision-resilient insect-scale compliant flapping-

wing robot was developed, while a collision-resilient MAV with foldable arms was introduced in [147]. Soft aerial robots were developed for physical interactions [143, 166]. Further, insect-inspired multicopters are presented with compliant frames to handle collisions [131] whereas compliant frames based on tensegrity [174] are shown helpful to reduce impact. Our prior work developed a collision-resilient MAV with compliant arms [110]. Compliant MAVs can reduce the effect of impact and help survive collisions; however, these robots cannot estimate contact force and handle impacts accordingly.

This work focuses on estimating contact force (excluding external torque). One way is to map robot control inputs to external contact forces offline [14]. However, this applies only when the robot is in contact. In a different approach, momentum-based external wrench estimators with second-order estimation dynamics [105, 205] and a Lyapunov-based nonlinear external wrench observer including also inertia shaping [212] have been proposed. Unscented Kalman filters are also utilized for estimation [124]. A nonlinear disturbance observer has been proposed to estimate contact force [54]. Recently, the feasibility of using cameras to estimate contact force was shown [193]. Yet, external force estimation in presence of compliant frames is an open task for aerial robots.

Aerial robots are equipped with end-effectors to physically interact with environments. In Ref [12], a compliant manipulator for impact reduction was studied. Flying robots with end-effectors are utilized to apply a force to vertical walls [70, 210], inspection [153] and sensor placement [193]. However, these projects focus on low-speed interactions, while high-speed collisions involve large impact forces and attitude changes. The interactions fail to assist with motion tasks such as planning and exploration.

Contrary to collision avoidance, impact-resilient robots can embrace contacts to improve overall safety and navigation task effectiveness. In Ref [137], the collision model into mixed integer programming for trajectory optimization was studied. Contacts can be also used to improve velocity estimation [105] and mapping [140]. Risk reward trade-offs have been studied for collision-inclusive trajectories [36, 115]. Local re-planners with setpoint adjustment post collision can be adopted to improve global planners like A$^\star$ [114, 116] and sampling methods [214]. However, these methods directly extend global planners and can bound to their constraints.

### 3.1.2 Frames and Notations

Similarly, the chapter uses the NWU (X North, Y West, Z Up) as the inertial frame $\mathcal{F}_I$ , and the FLU (X Forward, Y Left and Z Up) as the body-fixed frame $\mathcal{F}_B$. Key notation is shown in Tab. 3.1.

Table 3.1: Key Notation in Chapter 3

| | |
|---|---|
| $\mathcal{F}_I = \{\boldsymbol{e}_1,\ \boldsymbol{e}_2,\ \boldsymbol{e}_3\}$ | inertial frame |
| $\mathcal{F}_B = \{\boldsymbol{x}_b,\ \boldsymbol{y}_b,\ \boldsymbol{z}_b\}$ | body-fixed frame |
| $\mathcal{M} \in \mathbb{R}$ | mass of the robot |
| $\boldsymbol{R} \in \mathsf{SO}(3)$ | rotation matrix from body to inertial frame |
| $\boldsymbol{r} \in \mathbb{R}^3$ | position in inertial frame |
| $\boldsymbol{f}_T \in \mathbb{R}^3$ | thrust force in inertial frame |
| $\boldsymbol{f}_e \in \mathbb{R}^3$ | external force in inertial frame |
| $\hat{f}_e \in \mathbb{R}$ | estimated contact force along contact arm |
| $\boldsymbol{m}_T \in \mathbb{R}^3$ | moment by thrust force in inertial frame |
| $\boldsymbol{m}_e \in \mathbb{R}^3$ | moment by external force in inertial frame |
| $\mathcal{I} \in \mathbb{R}$ | inertia of the robot |

## 3.2 Development and Key Features of S-ARQ

### 3.2.1 Design

Inspired by prior works on compliant end-effectors [12], we introduce a lightweight compliant arm design and embed it onto a custom-made quadrotor to enable the latter to both estimate contact forces and stabilize from high-speed collisions [111]. The robot introduced in this work is named single-arm Active Resilient Quadrotor (s-ARQ). When moving forward in static environments (the robot's front faces the moving direction), robots mostly have contacts only in the front direction. We revise our earlier compliant aerial robot design [110] to attach one compliant arm onto the (rigid otherwise) chassis (Fig. 4.3).

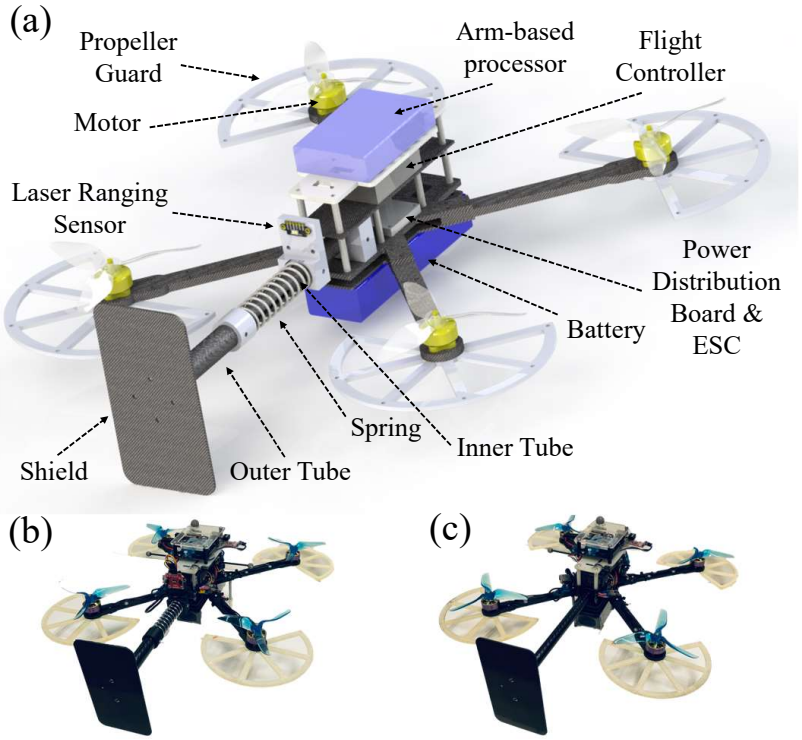


Figure 3.1: The impact-resilient aerial robot introduced in this work. (a) CAD rendering of the robot. Physical prototypes of the (b) compliant robot and (c) its rigid counterpart.

The new arm design consists of two carbon fiber tubes, a compression steel spring, a laser range sensor, and a carbon fiber shield. Carbon fiber tubes (tensile strength 125,000-175,000 psi) are assembled in a concentric manner. The outer tube has an outer diameter (OD) of 14.5 mm while the inner tube has an OD of 17.5 mm. The inner tube includes a linear slot to limit rotational motion with negligible friction, thus both tubes comprise a prismatic joint. A steel compression spring (OD 21.5 mm, free length 76 mm) connects both tubes. A lightweight fiber sheet ($75 \times 140$ mm) is fabricated with a Stepcraft D.600 CNC router with enclosure and milling bath, to work as the end-effector (shield) to contact with obstacles. Multiple custom adapters are 3D-printed with a Markforged Mark 2 printer. A laser range sensor (VL53L1X) is attached to the inner tube to measure the length of the compliant arm. Our design differs from works [12,193] in its capacity to enable stabilization from high-speed collisions with large impact, and estimate contact forces in presence of frame compliance.

The robot chassis is shared with our prior work [113] and consists of custom carbon fiber frames, a flight controller (Pixhawk), and an ARM-based multi-core processor (Odroid). The four frame arms measure 0.19 m, and the contact arm measures 0.28 m in free flight. The compliant robot weighs 890 g without batteries. For comparison purposes, we also build a rigid version (Quad), which shares the same quadrotor platform but a rigid contact arm of the same length (Fig. 3.1c). S-ARQ is 50 g heavier (4% of the total weight with batteries) compared to its rigid counterpart. We use a 5200 mAh Lipo battery yielding a flight time of approximately 610 sec.

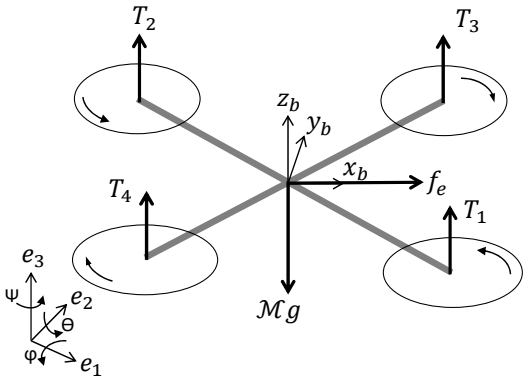


Figure 3.2: Dynamic model of the system.

### 3.2.2 Modeling

With reference to Fig. 3.2, the equations of motion for our robot following notation [205] are

$$\begin{aligned} \mathcal{M}\ddot{\boldsymbol{r}} &= -\mathcal{M}g\boldsymbol{e}_3 + \boldsymbol{R}\boldsymbol{f}_T + \boldsymbol{R}\boldsymbol{f}_e \\ \mathcal{I}\dot{\boldsymbol{\omega}} &= \mathcal{S}(\mathcal{I}\boldsymbol{\omega})\boldsymbol{\omega} + \boldsymbol{m}_T + \boldsymbol{m}_e \\ \dot{\boldsymbol{R}} &= \boldsymbol{R}\mathcal{S}(\boldsymbol{\omega}) \end{aligned} \tag{3.1}$$

where $\boldsymbol{r} = [x\ y\ z]^T$ is the position in the inertial frame (East-North-Up), $\mathcal{M}$ is the mass, and $\boldsymbol{R} \in SO(3)$ denotes the rotation matrix from body (Forward-Left-Up) to inertial frame. $\mathcal{S}(\cdot)$ is the skew-symmetric operator, $g = 9.81$ m/s$^2$ is the gravity constant, $\boldsymbol{e}_3 = [0\ 0\ 1]^T$, $\boldsymbol{f}_T$ and $\boldsymbol{f}_e = [f_e\ 0\ 0]^T$ are the thrust and external force vectors in body frame, respectively, and $\boldsymbol{m}_T$ and $\boldsymbol{m}_e$ are the moments generated by the thrust and external force vectors, respectively. Note that, as in [61], the external moment ($\boldsymbol{m}_e$) is not considered herein.

### 3.2.3 Contact Force Estimation

The contact force along the compliant arm can be measured utilizing Hooke's law

$$\hat{f}_e = -k_l(\delta l + l_0) \ ,$$

where $\delta l = l_{\max} - \hat{l}$ is the arm length difference ($l_{\max} = 0.28$ m) and $\hat{l}$ is the estimated arm length measured by the onboard distance sensor. To prevent oscillations, we pre-load the compliant arm ($l_0 = 2$ mm). The selected spring constant is $k_l = 3.80$ N/mm. The distance sensor has precision of 1 mm with accuracy of $\pm 5$ mm. To mitigate sensor noise we apply a recursive filter ($w = 0.6$) to sensor readings ($h_i$) as

$$\hat{l}_i = w h_i + (1 - w)\hat{l}_{i-1} \ . \tag{3.2}$$

The distance sensor has a frequency of around 25 Hz. Admittedly, this design can only estimate forces along the contact arm ($\boldsymbol{x}_b$ axis) in body frame. When flying toward known obstacles, the robot can face obstacles along its $\boldsymbol{x}_b$ axis utilizing yaw control. Although the compliant arm is of no help to estimate external torques, the prismatic joint does not affect estimating methods such as [205, 212].

## 3.3 Motion Control and Collision Handling

To stabilize after high-speed collision, the tracking controller of the robot must be able to follow aggressive trajectories with large attitude angles. In this work, we adopt the cascaded tracking control method as in our prior work [110]. Note that the attitude is described as roll ($\phi$), pitch ($\theta$) and yaw ($\psi$) angles, such that $\boldsymbol{R} = \boldsymbol{R}_z(\psi)\boldsymbol{R}_y(\theta)\boldsymbol{R}_x(\phi)$, where $\boldsymbol{R}_x, \boldsymbol{R}_y, \boldsymbol{R}_z$ are elementary rotation matrices about the coordinate axis (see Fig. 2.4). The planner generates desired states (position $\boldsymbol{r}_{\text{des}}$, velocity $\dot{\boldsymbol{r}}_{\text{des}}$ acceleration $\ddot{\boldsymbol{r}}_{\text{des}}$ and yaw angle $\psi_{\text{des}}$). The tracking controller comprises high-level position control, mid-level attitude and bodyrate control, and a low-level mixer to output PWM signals to actuators.

The position controller harnesses geometric constraints for nonlinear tracking [104, 127] as in Chapter 2. After calculating the desired attitude, we input it into a nonlinear attitude tracking controller to regulate the orientation of the robot. A Quaternion-based controller [19] is adopted in this work, but other attitude tracking methods can achieve similar performance. We refer the reader to the PX4 firmware [126] for details about the PID bodyrate control and mixer.

When collisions occur, the compliant arm compresses with increased estimated contact force ($\hat{f}_e$). Collisions are detected when $\hat{f}_e$ reaches a threshold ($\hat{f}_e^* = 25$ N). The maximum estimated contact force is measured ($\hat{f}_{e,\max}$), and the collision handling starts when the estimated contact force falls below $\hat{f}_e^*$ following the detection. We revise the collision handling to generate trajectories to reach a setpoint at a distance proportional to $\hat{f}_{e,\max}$. We use $\boldsymbol{r}_c, \dot{\boldsymbol{r}}_c$ to denote the position and velocity of the robot in the inertial frame when the collision handling is started, as well as the rotation matrix ($\boldsymbol{R}_c$). The new setpoint ($\boldsymbol{r}_n$) in the inertial frame can be written as

$$\boldsymbol{r}_n = \boldsymbol{r}_c - (\eta \hat{f}_{e,\max} + d_0)\boldsymbol{R}_c \boldsymbol{x}_b \ , \tag{3.3}$$

where $\eta$ and $d_0$ are constants ($\eta = 0.01$ m/N, $d_0 = 0.2$ m). During collision handling, the robot tracks a smooth (polynomial) trajectory so that for $t \in [t_0, t_T]$, $\boldsymbol{r}(t_0) = \boldsymbol{r}_c$, $\dot{\boldsymbol{r}}(t_0) = \dot{\boldsymbol{r}}_c$ and it stops at $\boldsymbol{r}(t_T) = \boldsymbol{r}_n$. The time interval is computed based on maximum accelerations and velocities [159].

## 3.4 Contact-Prioritized Planning

Contrary to collision-inclusive local re-planners [114, 214], this work proposes an intuitive global planner to exploit impact resilience. We draw motivation from the use case of aerial robots rapidly traversing forest-like environments, whereby maps contain isolated cylindrical obstacles with constant radius ($d_r$). With an intention to utilize the impact resilience, our proposed contact-prioritized (CP) planner prioritizes collisions to facilitate navigation.

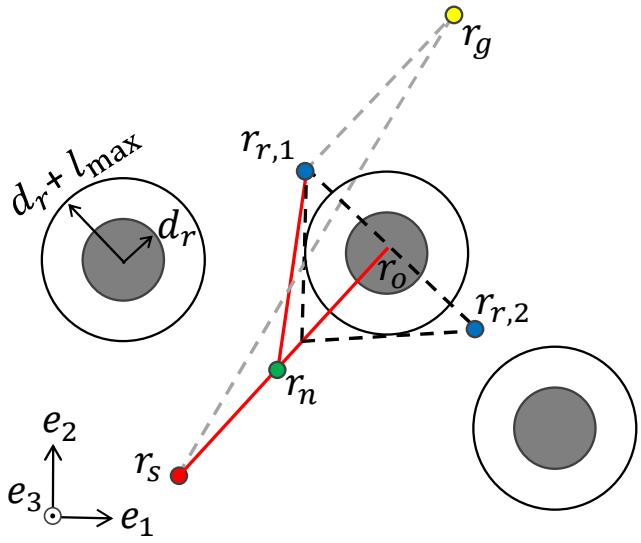


Figure 3.3: A novel planning method (CP) to prioritize contact to facilitate navigation in cluttered environments.

As shown in Fig. 3.3, the robot starts at $\boldsymbol{r}_s$ while the goal is at $\boldsymbol{r}_g$, which share the same altitude ($\boldsymbol{e}_3$), thus the navigation is simplified as 2-dimensional (2D) with constant $\boldsymbol{e}_3$. Note that the collision recovery has varying altitude but the setpoint $\boldsymbol{r}_n$ shares the same $\boldsymbol{e}_3$ value. The robot is simplified as a ball with a radius of $l_{\max}$, thus augmented obstacles have a radius of $d_r + l_{\max}$. The planner starts with drawing a line $\overleftrightarrow{\boldsymbol{r}_s\boldsymbol{r}_g}$ (gray

**Algorithm 1** ContactPrioritizedPlan($\boldsymbol{r}_s, \boldsymbol{r}_g, \boldsymbol{r}_o$)

**procedure** FIND WAYPOINT $\mathcal{W}$ FROM $\boldsymbol{r}_s$ TO $\boldsymbol{r}_g$
  **while** `isCollided`($\boldsymbol{r}_s, \boldsymbol{r}_g$) **do**
    $\mathcal{W} \leftarrow \mathcal{W} \cup \{\boldsymbol{r}_s\}$, $\boldsymbol{r}_t = \boldsymbol{r}_g$
    **while** `isCollided`($\boldsymbol{r}_s, \boldsymbol{r}_t$) **do** $\boldsymbol{r}_t \leftarrow$ `getFirstObstacle`()
    **end while**
    $\mathcal{W} \leftarrow \mathcal{W} \cup \{\boldsymbol{r}_t\}$
    $\boldsymbol{r}_{r,1}, \boldsymbol{r}_{r,2} =$ `getAddedWaypoint`($\boldsymbol{r}_t$)
    $\boldsymbol{r}_s \leftarrow \arg\min(|\overleftrightarrow{\boldsymbol{r}_{\mathrm{r},1}\boldsymbol{r}_g}|, |\overleftrightarrow{\boldsymbol{r}_{\mathrm{r},2}\boldsymbol{r}_g}|)$
  **end while**
  $\mathcal{W} \leftarrow \mathcal{W} \cup \{\boldsymbol{r}_g\}$
  **return** $\mathcal{W}$
**end procedure**

dashed), and checks if the line intersects with any augmented obstacles. If intersections occur, the robot moves toward the center of the first obstacle $\boldsymbol{r_o}$ while controlling yaw to face $\boldsymbol{r}_o$ along $\boldsymbol{x}_b$ axis, collides and stabilizes at $\boldsymbol{r}_n$ as described in (3.3). After recovery, two added waypoints $\boldsymbol{r}_{r,\{1,2\}}$ are found, which lie on the line perpendicular to $\overleftrightarrow{\boldsymbol{r}_s\boldsymbol{r}_o}$ (black dashed) with a distance of $\sqrt{2}(d_r + l_{\max})$. The robot moves to the added waypoint closer to the goal ($\boldsymbol{r}_{r,1}$ in this case), and repeats exploration with a new starting point ($\boldsymbol{r}_s = \boldsymbol{r}_{r,1}$) until no obstacles are found along the line $\overleftrightarrow{\boldsymbol{r}_s\boldsymbol{r}_g}$. Details can be found in the Alg. 1. The robot follows minimum-snap polynomial trajectories with the desired colliding velocities at the center of the in-contact obstacles.

## 3.5 Experimental Results

We present results from four experimental tests: force estimation, impact reduction, collision resilience, and planning. A 12-camera VICON motion capture system over WiFi was used for odometry feedback at a rate of 100 Hz. The feedback is only used to estimate the state of the robot, which can also be achieved by cameras or laser sensors in outdoor environments. Note that we use accelerometer data $\hat{\boldsymbol{a}}_b$ of the rigid robot for collision detection. Hence, collisions are detected whenever $||\boldsymbol{R}\hat{\boldsymbol{a}}_b + g\boldsymbol{e}_3|| \geq 2g$. The rigid robot employs the same collision handling method with a constant maximum force ($\hat{f}_{e,\max}$ = 80 N) as it cannot directly estimate contact forces.

### 3.5.1 Force Estimation

First, we study the force estimation of the compliant arm. Two cases are considered: when s-ARQ is placed on the ground (static) and while hovering (dynamic). We use a digital force gauge for ground truth. We apply constant forces to s-ARQ at $30, 40, 50$ N in the static case; in the dynamic case we apply impact forces (hit and release) of the same values. Table 3.2 shows the mean and standard deviation values of ten consecutive trials for each case. Despite sensor noise, results show relatively accurate contact force estimation

Table 3.2: Contact Force Estimation Statistics (10 trials).

| Case \ Impact | 30 N | 40 N | 50 N |
|---|---|---|---|
| Static (N) | $30.18 \pm 1.08$ | $39.76 \pm 1.62$ | $50.61 \pm 1.38$ |
| Dynamic (N) | $30.78 \pm 3.16$ | $40.66 \pm 4.06$ | $52.11 \pm 4.68$ |

when the robot is static. The estimation accuracy deteriorates in the dynamic case. This can be associated with vibrations in flight; yet, impact forces also contain larger errors when the robot is flying. Nevertheless, experimental results validate the feasibility of estimating contact forces using the developed compliant arm while in flight.

Further, we study the effect of the embedded compliance on the response to external impacts. We apply an impact force of 50 N along the $\boldsymbol{e}_1$ axis to both s-ARQ and its rigid counterpart, Quad (Fig. 3.4a top and bottom panels, respectively). Note that both robots have the same weight in the current and all following tests. Figure 3.4b depicts the position, velocity, and acceleration along the $\boldsymbol{e}_1$ axis of the compliant (blue solid) and rigid (red dashed) robots while the yellow-colored curve shown on the top panel denotes the estimated contact force on the s-ARQ robot. Note that accelerations are computed based on velocity data from motion capture in the current and all following tests.

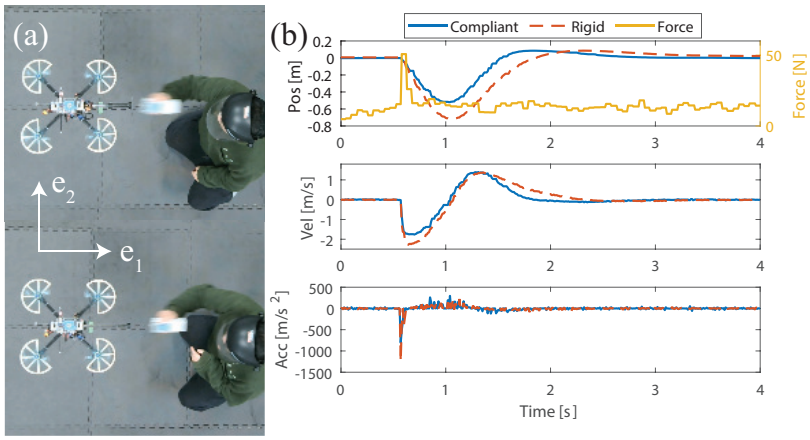


Figure 3.4: (a) Snapshots and (b) states tracking of a sample test to evaluate contact force estimation.

Results show that s-ARQ can detect a contact force of about 50 N, as desired. In addition, the compliant robot has fewer changes in all states under impact forcing owing

to the embedded compliance. This comparison indicates that existing methods that rely on robot states alone may underestimate impact contact forces when there is embedded compliance.

### 3.5.2 Impact Reduction

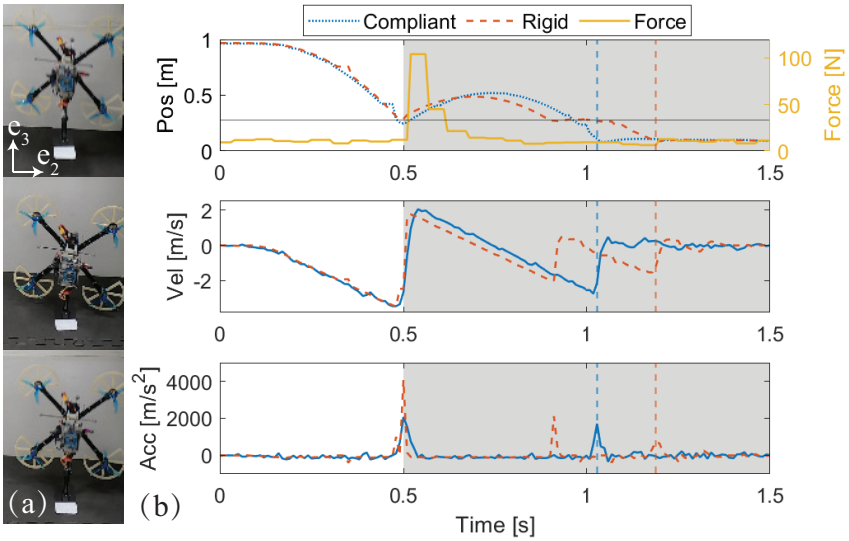


Figure 3.5: (a) Snapshots and (b) states tracking of a 0.7 m drop test to study impact reduction. Grey-shaded area denotes states post impact.

In the second set of tests we seek to study the impact reduction afforded by the embedded compliance. To this end, we employ drop tests. Both robots are fixed vertically ($\boldsymbol{x}_b$ facing $-\boldsymbol{e}_3$ and $\boldsymbol{z}_b$ facing $\boldsymbol{e}_1$) before falling to the ground (hard floor mat) from $0.3, 0.5$ and 0.7 m along $\boldsymbol{e}_3$ axis.

Figure 3.5a shows snapshots from one of the 0.7 m drop tests for s-ARQ. The compliant arm touches the ground (top), compresses to the minimum length (middle), and then bounces back (bottom). Figure 3.5b depicts position, velocity and acceleration tracking along the $\boldsymbol{e}_3$ axis of s-ARQ (blue solid) and Quad (red dashed) for a sample 0.7 m drop

test, as well as the estimated contact force (curve in yellow at the top panel). A horizontal black line denotes the $\boldsymbol{e}_3$ value (0.28 m) when the robot is placed vertically on the ground.

Results show that both robots have identical position and velocity profiles before touching the ground with a velocity of $-3.46$ m/s. The compliant arm length reduces to its minimum, followed by a saturated force estimation of 104 N. During the impact, s-ARQ has a maximum acceleration of $2,069$ m/s$^2$ while Quad reaches $4,063$ m/s$^2$. Blue and red vertical dashed lines denote that the robot flips to a horizontal state ($\boldsymbol{z}_b$ facing $\boldsymbol{e}_3$), and therefore lower $\boldsymbol{e}_3$ values are observed.

Table 3.3: Recorded Maximum Acceleration Statistics (10 trials).

| Robot \ Drop Height | 0.3 m | 0.5 m | 0.7 m |
|---|---|---|---|
| Compliant (m/s$^2$) | $1,017 \pm 103$ | $1,545 \pm 129$ | $2,177 \pm 140$ |
| Rigid (m/s$^2$) | $1,809 \pm 186$ | $2,774 \pm 169$ | $3,649 \pm 175$ |

Further, we repeat ten drop tests at different $\boldsymbol{e}_3$ values for both robots and record the mean and standard deviation of maximum accelerations attained (Tab. 3.3). Results show that the compliant arm design can help reduce impact by 43.8%, 44.3%, and 40.3% in the drop tests at $0.3, 0.5$, and 0.7 m, respectively. Results demonstrate that our compliant aerial robot design can reduce impact by around 40% with only 4% weight increase.

### 3.5.3 Collision Resilience

We also study the s-ARQ robot's collision resilience using extensive physical collision tests against vertical walls and poles at different velocities and yaw and pitch angles, and compare against the rigid robot, Quad. In wall tests, we place a vertical wall at the

$\boldsymbol{e}_1$ position of 2.45 m and perpendicular to $\boldsymbol{e}_1$ axis. Both robots take off at the $\boldsymbol{e}_1$ position of $-1$ m and fly along the $\boldsymbol{e}_1$ axis before hitting the wall with zero Euler angles (identity rotation matrix). Owing to the embedded compliance's utility to reduce impact, s-ARQ can sustain wall collisions at a speed of 3.0 m/s with a 100% success rate for ten consecutive trials (see supplemental video). In contrast, the rigid Quad robot can fail at the highest speed collision of 3.0 m/s because of IMU malfunctions caused by the impact.

With reference to Fig. 3.6a, s-ARQ has the compliant arm compressed when colliding with the wall, followed by recovering with large attitude angles and stabilizing at a safe position. Figure 3.6b depicts the position and velocity of s-ARQ along the $\boldsymbol{e}_1$ axis, as well as the pitch angle $\theta$. Blue solid curves denote the actual states while the red dashed ones represent the desired states from the planner. A yellow curve denotes the estimated contact force (top panel), and a grey-shaded area means the recovery control is enabled.

Results show that s-ARQ touches the wall at a speed of 3.0 m/s at time $t = 1.35$ s. The robot stops and bounces back at a speed of $-1.60$ m/s, during which a maximum contact force of 90 N is recorded. Recovery control is enabled (desired states) when the estimated force drops below the threshold ($\hat{f}_e^* = 25$ N) at $t = 1.51$ s. The recovery trajectory begins at current position, velocity and attitude states, and stabilizes rapidly at a distance proportional to $\hat{f}_{e,\max}$.

In addition, we conduct wall collision tests at velocities of $1.5, 2.0$, and 2.5 m/s along $\boldsymbol{e}_1$ axis for both s-ARQ and Quad. Figure 3.7a shows a top view of s-ARQ robot wall collision test, where the compliant arm compresses to reduce impact and protect onboard sensors. Figure 3.7b visualizes sample trials of wall collision tests at a velocity of 2.5 m/s for

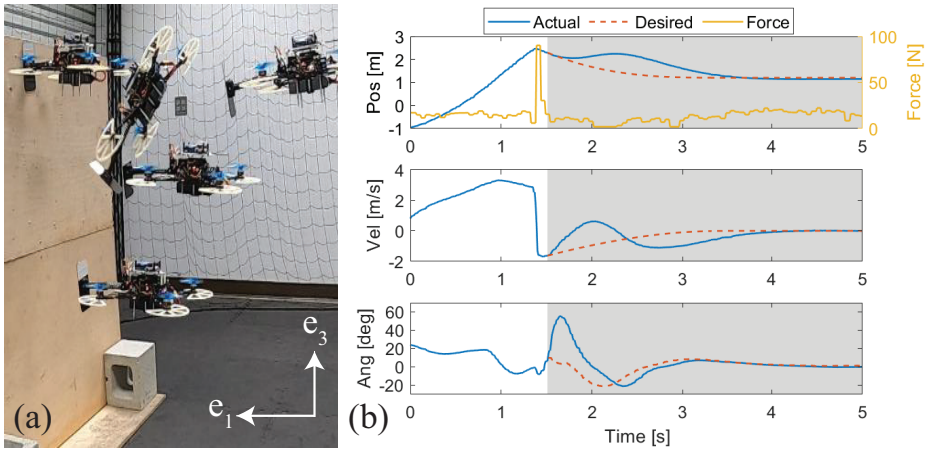


Figure 3.6: (a) Snapshots and (b) states tracking of a sample wall collision test at a speed of 3.0 m/s for s-ARQ.

both robots, where solid curves denote measured states while dashed ones represent desired states from the planner. Similarly, blue and red curves visualize position, velocity, and acceleration states of s-ARQ and its rigid counterpart, respectively. Blue and red vertical dashed lines denote the time when recovery controls are enabled for s-ARQ and Quad, and the yellow curve shows the estimated force on s-ARQ.

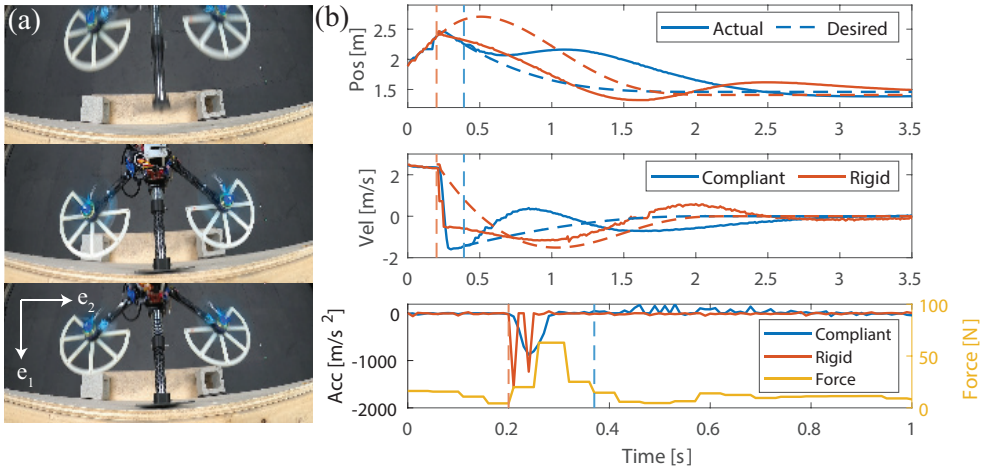


Figure 3.7: (a) The compliant arm compressing during a collision. (b) State tracking of both s-ARQ and Quad for 2.5 m/s wall collisions.

Results show that both robots have identical states before the contact at time $t = 0.2$ s, when a collision is detected for the rigid robot. The velocity of Quad changes sharply from 2.5 to $-0.5$ m/s in 0.05 s, resulting in a maximum acceleration of $-1,570$ m/s$^2$. Due to the short contact time, the 100 Hz motion capture feedback causes discontinuity in the velocity tracking. On the contrary, the compliant arm elongates the contact time to 0.1 s, and reduces the impact to $-876$ m/s$^2$. A maximum contact force of 63 N is estimated; however, there is a slight delay in the force estimation due to the filter (3.2). The recovery control of s-ARQ is enabled at $t = 0.37$ s, when the estimated contact force falls below the threshold. s-ARQ collision handling is started 0.17 s later than Quad's. Still, s-ARQ stabilizes at $t = 3.0$ s with a settling time of 2.5 s, compared to 3.3 s of Quad. In sum, these findings demonstrate that s-ARQ can stabilize from collisions faster while also mitigating impacts, as compared to the rigid robot. In an effort to demonstrate the preliminary feasibility of our method to apply in practical use cases where high-accuracy localization feedback from motion capture is not available, we experimentally determined that the robot has same success rates when motion capture position feedback was processed (degraded) prior to be sent to the robot in a way that emulates key differences with visual inertial odometry feedback (namely lower accuracy and larger delay).

Despite frequently missing in related works, we study collisions against pole obstacles, as well as different yaw and pitch collision angles for s-ARQ. The pole obstacle has a radius of 0.15 m. We drive the s-ARQ robot to have yaw angles 10° (left), 0° (middle) and $-10°$ (right) collisions against wall and pole obstacles (see supplemental video). Note that the robot has a collision velocity of 2.0 m/s in all tests. Results show that the robot

can stabilize from collisions against walls and poles with different yaw angles. Larger angle changes occur during wall collisions in non-zero yaw angles due to the flat geometry of the shield. The collision handling records the current yaw angle at the time of triggering and sustains the angle for stabilization. On the contrary, large angle changes are observed with zero colliding yaw angle in pole collisions, since the robot is not ideally pointing to the geometric center. In addition, s-ARQ can survive wall collisions with yaw angles up to 30° (see supplemental video). However, direct contacts between obstacles and propellers occur at larger yaw angles, which pose danger to the robot. Further, the robot was experimentally found able to stabilize from large-pitch collisions of ±30° as well (see supplemental video).

### 3.5.4 Contact-Prioritized Planning

In the final set of tests, we study the proposed CP planning method, and compare against A* [107] and RRT* [81] in both simulated and physical experiments. The latter help validate the proposed method in practice whereas simulations help better understand the behavior of our CP planning algorithm in terms of its scalability in increasingly cluttered maps, all in relation to standard-of-practice planning algorithm baselines.

#### Offline Planning

The experimental map has a size of $4 \times 3$ m. Four uniform pole obstacles with a radius of 0.15 m are located as shown in Fig. 3.8. The robot starts at $[-2, 0]$ and the goal is at $[-2, -0.2]$. We discretize the map with a resolution of 0.1 m, and run the three algorithms on a Windows machine with an Intel Xeon Processor (3.50 GHz). Four metrics are used to evaluate different methods: planning time, trajectory time, path length and minimum

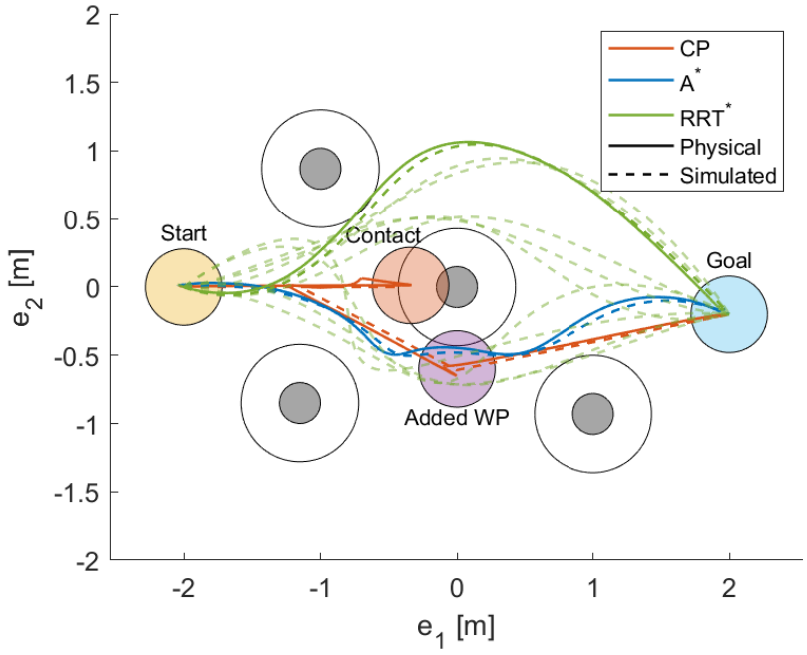


Figure 3.8: Physical and simulated trajectories for different planners.

distance to obstacles (clearances). The planning time records the time to find paths in milliseconds, excluding the time for trajectory generation. The trajectory time records the time for robots to reach the goal following the trajectories in seconds. Path lengths denote the Euclidean distance among waypoints (WP). Lastly, we record the clearances between trajectories and augmented obstacles to evaluate the safety against potential collisions as in [176]. Note that in-contact obstacles are excluded in the CP planner due to the strong resilience to controlled collisions.

Figure 3.8 depicts physical (solid) and simulated (dashed) trajectories of the three planning methods. Note that RRT* results are stochastic with all simulated trials are visualized, however, and only one sample trial is included in the physical testing. Note that polynomials are generated based on waypoints from A* and RRT* planners at a maximum velocity of 1.5 m/s, while the CP method collides with obstacles at 2.5 m/s. The robot

Table 3.4: Comparison Metrics for the Planning Methods.

| Metrics \ Method | **CP** | A* | RRT* |
|---|---|---|---|
| Plan. Time (ms) | 2.0 | 48.9 | $28.3 \pm 0.9$ |
| Simul. Traj. Time (s) | 9.4 | 10.0 | $11.3 \pm 1.4$ |
| Phys. Traj. Time (s) | 9.3 | 10.1 | 12.3 |
| Path Len. (m) | 5.5 | 4.2 | $4.4 \pm 0.2$ |
| Simul. Cl. (m) | 0.09 | 0.05 | $0.01 \pm 0.03$ |
| Phys. Cl. (m) | 0.10 | 0.01 | $-0.02$ |

recovers at position $\boldsymbol{r}_n = [-1.25, 0]$ and moves to added WP $\boldsymbol{r}_r = [0, -0.61]$ before reaching the goal.

Comparison metrics of all methods are shown in Tab. 3.4. It can be observed that simulated results generally match with the physical ones. Results show that our proposed method requires only around 4% and 7% planning time compared to A* and RRT* planners. In addition, results show that CP leads to the lowest trajectory time. Despite having a larger path length due to the collision recoveries, the CP planner has almost double obstacle clearances, indicating the enhanced safety of the trajectories. This is in fact a benefit of our controlled collision-inclusive planning: by selecting where to collide (safely), the risk for future (unsafe) collisions (as measured by clearances to other obstacles) can be reduced.

We extend planning tests to simulated cluttered maps. The maps have a size of $20 \times 20$ m with 30 pole obstacles (see supplemental video). The obstacles have a uniform radius of 0.3 m, and are randomly distributed with a clearance of 2.5 m from center to center. The start is at $[-8, -8]$ while the goal is at $[8, 8]$. Ten trials are run for each map

and planning method with a discretization resolution of 0.5 m. Note that $|v_{\max}|$ of simulated trajectories by A* and RRT* planners were capped at 1.5 m/s, and a collision speed of 3.0 m/s was used for trajectories of the CP planner as our prior work indicated higher velocities with collision resilience [114].

Simulated results are listed in Fig. 3.9 where different planners are evaluated in four metrics as mentioned above. Note that two cases of the CP planner are studied in the trajectory time comparison. The compliant robot (CP C.) has a maximum velocity of 3.0 m/s and recovery time 2.5 s, while the rigid robot (CP R.) uses the velocity 2.5 m/s and time 3.3 s, as we measured in the collision tests. Results show that the CP planner cost around 30% planning time compared to other methods. In the meantime, the results show that the compliant aerial robot with the CP planner saves about 36% and 45% trajectory time compared to A* and RRT* planners, respectively. The compliant robot saves about 10% trajectory time compared to its rigid counterpart under the same planner. On the other, the CP planner has longer path lengths than A* method in the simulation, similar to the observations in the physical test. However, the results show that the trajectories generated by the CP planner have doubled the clearances compared to other methods. To sum up, simulated results help demonstrate that our proposed CP planner can outperform collision-avoidance planning methods A* and RRT* in terms of planning time, trajectory time and path safety, despite longer path lengths than the A* planner.

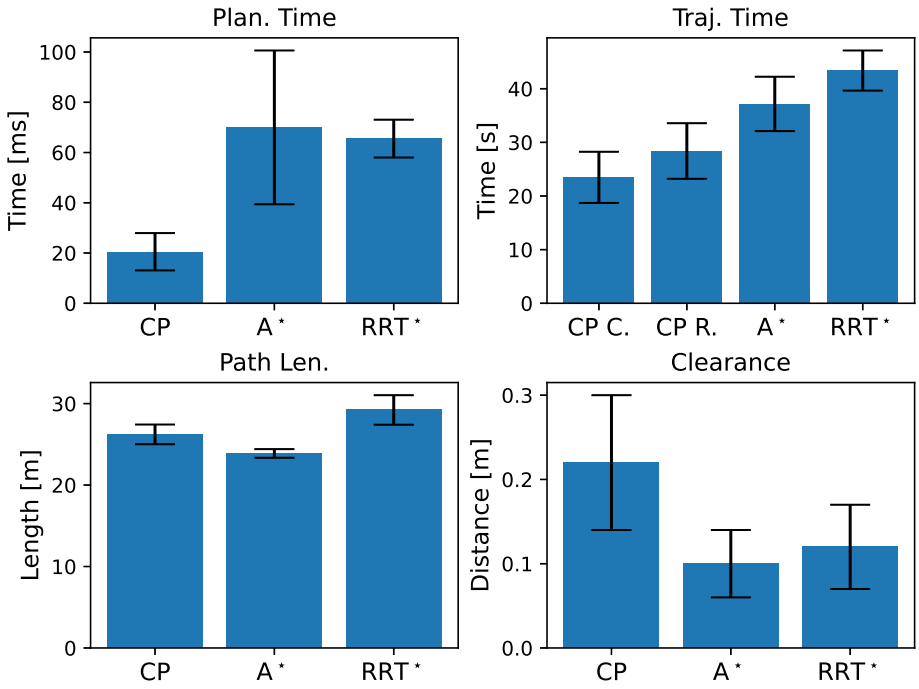


Figure 3.9: Comparison metrics for simulated studies on cluttered maps.

**Online Planning**

In support of our method's preliminary feasibility to apply in practical use cases, we also include a simulated study where the robot operates in partially-known maps. The robot can localize obstacles only within a sensing range of 5 m, which is consistent with practice when the robot relies on cameras or (short-range lightweight and airborne) LiDAR sensors for localization. Both CP and A* methods are run online with a re-planning interval of 5 s. Similarly, ten random maps with 30 obstacles are studied for each planner.

We list the simulated results for both offline and online tasks in Tab. 3.5. Note that we also include the trajectory generation time, which stands for the process to convert waypoints to polynomial-based trajectories by solving a constrained optimization problem. Results show that both planning methods have lower planning time in the online task.

Table 3.5: Comparison Metrics for Different Environments.

| | Metrics | Offline | Online | Units |
|---|---|---|---|---|
| **CP** | Plan. Time | $20.50 \pm 6.43$ | $16.78 \pm 4.41$ | ms |
| | Traj. Gen. Time | $0.079 \pm 0.026$ | $0.318 \pm 0.122$ | s |
| | Traj. Time | $23.48 \pm 4.77$ | $31.04 \pm 5.27$ | s |
| | Path Len. | $26.22 \pm 1.21$ | $28.64 \pm 2.98$ | m |
| A* | Plan. Time | $70.02 \pm 30.61$ | $38.51 \pm 4.52$ | ms |
| | Traj. Gen. Time | $32.80 \pm 2.65$ | $26.17 \pm 7.40$ | s |
| | Traj. Time | $37.17 \pm 5.07$ | $40.30 \pm 4.37$ | s |
| | Path Len. | $23.88 \pm 0.53$ | $24.25 \pm 1.22$ | m |

The A* planning method has a larger decrease, indicating high sensitivity to map size. Results also show that the CP method has lower planning time in both settings. Despite the increased trajectory generation time in partially-known environments, the CP planner costs around 1% time of the A* method in generating trajectories, indicating improved efficiency. Both planners have longer trajectory time in the online task due to the limited knowledge of the map. Still, trajectories generated by the CP planner save about 23% of the time compared to A* trajectories, despite longer path lengths in both settings.

## 3.6 Conclusions

In this chapter, we present a lightweight compliant arm to sense contacts and reduce collision impact. Equipped with the integrated arm, we develop a novel impact-resilient aerial robot, named s-ARQ, to stabilize from high-speed collisions. Experimental results show that the compliant robot has only a 4% weight increase but around 40% impact reduction compared to a rigid counterpart. Further, when equipped with a real-time contact

force estimator and a non-linear motion controller, the compliant robot can handle collisions while attempting aggressive maneuvers, and stabilize from high-speed wall collisions at 3.0 m/s with a success rate of 100%. This impact resilience is also verified with pole obstacle collisions, as well as with different yaw and pitch angles.

We also propose and validate in both simulated and physical experiments a planning method for impact-resilient robots that prioritizes contacts to facilitate navigation. Physical tests and extended simulations demonstrate that our proposed compliant robot and contact-prioritized planning method can accelerate the computation while achieving shorter trajectory time by relaxing velocity constraints. Despite having a larger path length due to the collision and follow-on recovery, the CP planner leads to higher clearances, indicating enhanced safety. Online planning tests in partially-known environments were also studied. Simulated results further validated the efficiency of the proposed CP planner, with reduced planning and trajectory generation time, shorter trajectory time and increased clearances. Admittedly, the CP planner has longer trajectory time compared to collision-avoidance planning methods when applying velocities constraints. However, the significant saving in computational time and increased trajectory safety may outweigh the increasing path length limitation. The proposed CP planner thus provides positive results to study how to utilize contacts to facilitate navigation, especially when computational time is of essence.

In the next chapter, we study effects of compliance on robot-robot interactions by presenting an innovative solution to utilize an aerial robot with a compliant gripper to safely capture another flying micro-robot.

# Chapter 4

# Motion Control and Planning of Compliant Aerial Grasping

This chapter focuses on the compliance between robot-robot interactions. Specifically, we present an innovative solution on catching safely an aerial micro-robot in mid-air using another aerial robot that is equipped with a universal soft gripper. We first introduce a gripper design based on soft actuators that can stay horizontally straight with a single fixture and maintain sufficiently compliance in order to bend when air pressure is applied. Further, we develop an aerial robot equipped with the developed soft end-effector and that features an onboard pneumatic regulation system. Static grasping tests study the soft gripper's robustness in capturing aerial micro-robots under aerodynamic disturbances. We experimentally demonstrated the feasibility of using the SoAG robot to catch a hovering micro-robot with or without propeller guards. The feasibility of dynamic catching is also shown by capturing a moving aerial micro-robot with a velocity of 0.2 m/s. The free flight

performance of the SoAG robot is studied against a conventional quadrotor and in different gripper and payload status.

This chapter is organized as follows: Section 4.1 discusses background and related works for aerial grasping and flying target captures; Section 4.2 presents the overview of the aerial platform with soft gripper, as well as the pneumatic actuation; We discuss the dynamic modeling in Section 4.3, as well as the planning in 4.5. Finally, we experimentally study the mid-air capture of both hovering and moving aerial targets, as well as the free flight performance test.

## 4.1 Background

Grasping with aerial robots attracts increasing interest from both research institutes and companies across industry sectors, owing to these robots' unique capability to operate in 3-dimensional (3D) space while avoiding terrain constraints that often limit access to ground robots (and humans) [164]. Grasping can be defined as a sequence of three key consecutive steps: 1) approaching a target, 2) establishing contact with the object, and 3) securing and holding the object firmly [129]. Grasping is also a crucial ability for aerial robots to interact with the environment and facilitate several key applications such as inspection [211], search and rescue [67], transportation [56], and construction [10].

### 4.1.1 Related Work

The most common way to achieve aerial grasping is to directly mount robotic manipulators onto appropriate aerial robots. Notable examples include multirotor aerial

vehicles with mostly servo-driven robotic arms [11, 64, 78, 92, 99, 165, 192, 216]. To overcome payload limitations, unmanned helicopters have been utilized to carry industry manipulators [13, 97, 151]. Aerial robots have also been equipped with dual robotic arms for precise manipulation [98, 195] as well as parallel manipulators [33, 34, 61]. Multi-link robotic arms can provide precise position control of the end-effector with improved reachability. However, mounting robotic arms on aerial robots requires larger scales thereby leading increasing costs and compromising mobility in confined environments. Such aerial manipulators often employ ordinary multi-finger end-effectors; studying the ability to grasp irregularly-shaped micro-objects has received less attention. A fixed-wing aerial vehicle is equipped with a passive claw for high-speed grasping [194]. However, the robot is still constrained to grasping regular objects such as poles. In a different line of work, multi-robot systems can be leveraged to grasp and move objects [62, 160, 183, 218]. However, cooperative grasping increases the computational effort on control and planning, and requires significant system integration efforts to be practical. The aerial grippers are often constrained to vertical grasping, which limits potential applications.

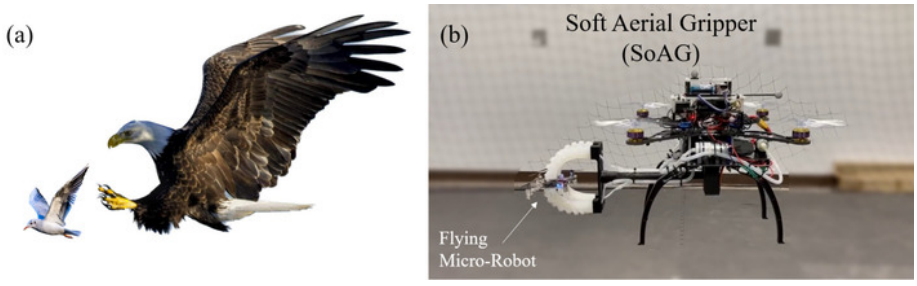


Figure 4.1: Bio-inspiration and prototype of the project. (a) An eagle is horizontally catching a small bird in mid-air. (b) To enable horizontal grasping, we develop an micro-aerial vehicle (MAV) equipped with a soft end-effector and onboard pneumatic regulation named Soft Aerial Gripper (SoAG).

Distinctly from rigid aerial robot grasping, soft (compliant) grasping has been receiving increased attention due to its advantages of being robust and safe to irregularly-shaped objects [185]. Several micro aerial vehicles (MAVs) have been equipped with soft (compliant) end-effectors, including but not limited to impactive and ingressive [128], compliant multi-fingered [7, 24, 65, 101, 125, 152, 217], closed-structure compliant [103], origami-inspired [91], wasp-pedal-carrying [219], soft cable-driven [57,157], and soft pneumatic [132] grippers. However, these aerial grippers have been limited to vertical grasps directly underneath the robot, which, besides limiting applicability, is also impacted by aerodynamic disturbances.

In recent years, there is a growing interest in developing non-military tools to capture aerial robots in mid-air with applications to recover malfunctioning aerial robots and intercept and contain unidentified flying targets [146]. Physically catching flying robots in mid-air is challenging due to their irregular shapes and self-propulsion. Notable attempts include a soft gripper fixed on a ground manipulator to catch flying micro-robots [55]. However, the solution is limited by vertical grasping, as well as the workspace of the ground manipulator. The most common way to catch flying robots in mid-air is using nets, such as net bullets [44,130], top nets [43,162], side nets [209], and nets carried by cooperative vehicles [94, 163]. Despite the proved effectiveness, these solutions primarily focus on catching aerial robots with diagonal sizes (including propellers) over 500 mm (e.g. DJI Mavic Pro and Phantom 4). However, little attention is paid to capturing flying micro-robots such as Crazyflie 2.1 with diagonal sizes around 100 mm, which are relatively more challenging to detect and intercept [146]. In addition, capturing by nets involve relative motion to

targets that will inevitably create impact and possibly damage target robots. Flying robots with nets are usually unable to grasp, move and release objects compared to ones with conventional grippers. A recent work studies catching aerial micro-robots with a passive gripper [25]. However, the capture relies on contact with the propeller guard of the target, which is usually missing with commercially available aerial vehicles. After capturing, the suspending target will compromise the free fly performance of the catcher [92]. Similarly, the method requires relative velocities to the target, and creates impact.

In this work, we aim to address the challenge of catching aerial micro-robots safely in mid-air using flying robots with a universal soft gripper. To this end, we introduce a soft actuator and pneumatic four-fingered end-effector designs to enable horizontal grasps. As shown in Figure 4.1, we develop a quadrotor MAV equipped with a soft end-effector named Soft Aerial Gripper (SoAG). The hardware design of SoAG is introduced, as well as the dynamic modeling and control. Piecewise-polynomial-based optimal planning is studied to facilitate catching of flying targets. Static grasping results are compared to a commercially-available gripper to validate the efficacy of grasping irregular objects. Experimental trials also demonstrate the feasibility of using the SoAG robot to catch a target aerial micro-robot while both agents are flying without relative velocities to mimimize impact. We study the robustness of the soft gripper with catching tests of flying targets with or without propeller guards. Furthermore, we study the feasibility of dynamic catching by capturing a moving aerial micro-robot in the mid-air. Lastly, free flight performance of the SoAG robot is studied and compared to a conventional quadrotor to validate the design and evaluate the effect of the gripper on flight mechanics, control, and energetics.

### 4.1.2 Frames and Key Notations

We considered NWU (X North, Y West, Z Up) as the world frame, denoted with $\mathcal{W} : \{\boldsymbol{O}_W; \boldsymbol{x}_W, \boldsymbol{y}_W, \boldsymbol{z}_W\}$ (see Figure 4.2a). The body frame of the robot is denoted with $\mathcal{B} : \{\boldsymbol{O}_\mathcal{B}; \boldsymbol{x}_\mathcal{B}, \boldsymbol{y}_\mathcal{B}, \boldsymbol{z}_\mathcal{B}\}$; its origin coincides with the robot's center of mass. We also define the end-effector frame $\mathcal{E}$ with its origin at the center of the gripper. Also let $\mathcal{T} : \{\boldsymbol{O}_\mathcal{T}; \boldsymbol{x}_\mathcal{T}, \boldsymbol{y}_\mathcal{T}, \boldsymbol{z}_\mathcal{T}\}$ be the frame attached to the target. We use $\boldsymbol{R}_{WB} \in \mathsf{SO(3)}$ to denote the orientation of the body frame in the world frame.

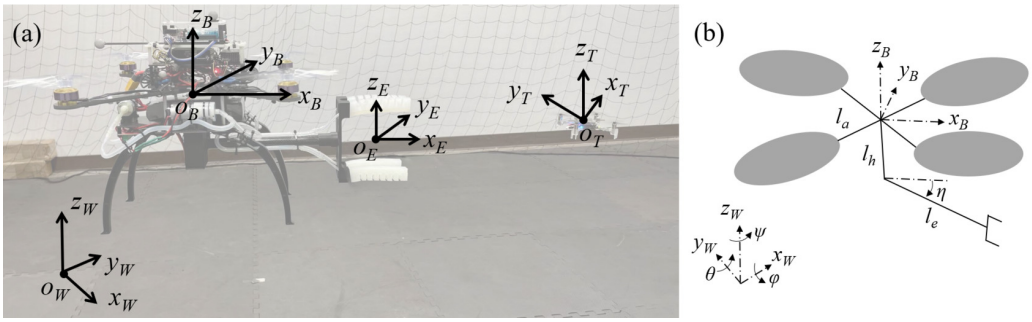


Figure 4.2: Frames and modeling description. (a) Four frames are defined in this work: world, robot, end-effector and target frames. (b) Dynamic model of the system.

## 4.2 Development and Key Features of SoAG

This project exploits soft robotic grippers to catch flying micro-robots safely. However, horizontal grasps are challenging for most soft grippers because they cannot stay horizontally straight with a single fixture. As mentioned earlier, horizontal captures are critical to avoid aerodynamic disturbance (downwash), which can make targets crash. Thus, this paper revises the Pneumatic Network (PneuNet) design [136, 149] to enable horizontal grasps.

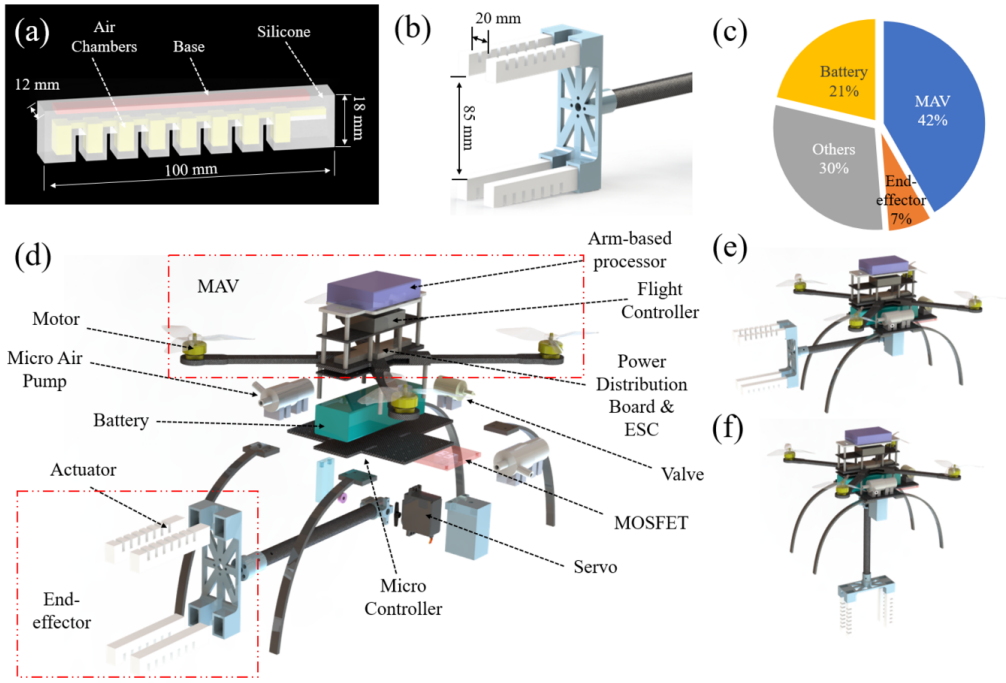


Figure 4.3: Details of the system design. (a) Actuator design. (b) End-effector design. (c) Weight distribution of the SoAG robot. (d) An exploded view of the SoAG robot. (e and f) The robot with the arm up and down.

### 4.2.1 Actuator Design and Fabrication

Two improvements to the PneuNet design are made to achieve horizontal grasps. To minimize deformation by gravity and keep the softness for safe interactions, appropriate stiffness of the actuators is achieved by combining two materials with different shore hardness. As shown in Figure 4.3a, the main body (white) is made of Smooth-On Dragon Skin 20 silicone with shore hardness of 20A (A here meaning the type A indenter and scale) to maintain the softness for adaptive grasps. In the PneuNet design, there is an inextensible layer to assist bending, which is made of thin fabric or paper [149]. However, the thin inextensible layer fails to increase the stiffness sufficiently for horizontal grasps. In this work, we replace the thin inextensible layer with a solid flexible cuboid base (part shown

in red in Figure 4.3a), which is 3D-printed using the Formlabs flexible 80A resin. The base has a shore hardness of 80A. Despite increased hardness, the actuators still maintain enough compliance to bend relatively fast under pneumatic inflation. Moreover, the actuator's width is reduced and base thickness is increased to accelerate actuation response and support the horizontal-grasping potential. Details of the revised dimensions can be found in Figure 4.3a, where parts in yellow denote the implanted air chambers.

The fabrication of actuators follows the conventional method of casting with molds. The custom molds are 3D-printed in polylactic acid (PLA) while bases are directly 3D-printed with flexible 80A resin as mentioned earlier. With molds and bases ready, we mix the elastomer and process it using a degassing chamber. After cured, the two casted parts of the actuator (chamber and base layers) are bonded with an adhesive (Sil-Poxy). Note that the flexible 80A base should be surrounded by silicone in the manufacturing of the base layer.

### 4.2.2 End-effector Design

Similar to conventional grippers, our four-fingered soft end-effector consists of two opposing claws. When inflated, the tips come together on opposite sides (top and bottom) of flying micro-robots to grasp them. Each claw of the gripper has two actuators in parallel with a gap of 20 mm while the two opposite sides have a distance of 85 mm as shown in Figure 4.3b. All actuators are fixed by a 3D-printed adapter connecting to the aerial platform using a carbon fiber rod. The end-effector weighs 0.115 kg, accounting for only 7% of the total weight (see Figure 4.3c). We evaluated the end-effector performance by comparing it to a commercially available gripper, as detailed in Section 4.6.

### 4.2.3 SoAG Robot Design

We mount the end-effector on a custom quadcopter MAV to develop the SoAG robot. The robot has a total weight of 1.64 kg, which consists of four types of components: MAV, battery, end-effector, and other parts (see Figure 4.3c). A hardware overview of SoAG is shown in Figure 4.3d. The custom-made MAV features frames that are fabricated with lightweight carbon fiber sheets (tensile strength $120,000 - 175,000$ psi) using a Stepcraft D.600 CNC router with enclosure and milling bath. The MAV measures 380 mm from the motor tip to tip. It integrates a flight controller (Pixhawk 4 Mini) running the corresponding open-source autopilot system. The vehicle also includes an ARM-based multi-core processor (Odroid XU4) for high-level computing tasks.

In addition to the MAV and end-effector (highlighted in red boxes in Figure 4.3d), the robot also includes pneumatic regulating components necessary to power the soft gripper. The onboard pneumatic regulation consists of two micro air pumps, one solenoid valve, and one MOSFET module. The air pumps have a flow rate of 2.0 L/min with a low weight of about 0.07 kg. When the robot tries to catch a target, the two pumps will inflate four actuators to bend (one pump per two actuators) and close the gripper. All actuators are also connected to the normally-closed solenoid valve, of which the other side is directly open to the atmosphere air. When pumps are off and the valve is on, the pressure values inside the actuators will decrease to the atmospheric one so that the gripper will open. The MOSFET module reads PWM signals and regulates the DC voltages of the pumps and valves. SoAG has one revolute joint to move the position of the end-effector to the main robot (see Figure 4.3e&f). A MG 996R servo motor controls the angle of the revolute joint between

the vehicle and the arm. We use a micro-controller (Arduino Nano) to control both the pneumatic actuation and the arm angle.

## 4.3 Modeling

The $\boldsymbol{R}_{WB}$ can be written following the Z-X-Y sequence as

$$\boldsymbol{R}_{WB} = \begin{bmatrix} c_\phi c_\psi - s_\phi s_\theta s_\psi & -c_\theta s_\phi & c_\phi s_\psi + c_\psi s_\phi s_\theta \\ c_\psi s_\phi + c_\phi s_\theta s_\psi & c_\phi c_\theta & s_\phi s_\psi - c_\phi c_\psi s_\theta \\ -c_\theta s_\psi & s_\theta & c_\theta c_\psi \end{bmatrix} , \tag{4.1}$$

where $c$ denotes the cosine, $s$ stands for sine, and Euler angles $\phi, \theta$, and $\psi$ denote rotating angles along the axis $x, y$ and $z$, respectively.

The generalized coordinate variables comprise the position of $\boldsymbol{O}_{\mathcal{B}}$ ($\boldsymbol{p} = [x,\ y,\ z]^T \in \mathbb{R}^3$), the Euler angles ($\Phi = [\phi,\ \theta,\ \psi]^T \in \mathbb{R}^3$) of the aerial robot in the world frame, as well as the joint angle $\eta \in \mathbb{R}$ with respect to the zero position as in Figure 4.2b. For simplicity, we drop the superscript $W$ for the world frame. The vector that contains all the generalized coordinate variables can be written as $\boldsymbol{\xi} = [\ p^T,\ \Phi^T,\ \eta\ ]^T \in \mathbb{R}^7$.

As shown in Figure 4.2b, the revolute joint lies along the axis $z_B$ and its distance from the robot's center of mass $\boldsymbol{O}_B$ is $l_h$. Let $l_e$ be the length between the joint and the center of the end-effector $\boldsymbol{O}_E$. The arm of the end-effector is constrained within the $x_B - z_B$ plane of the body frame. Thus, we can find the position of $\boldsymbol{O}_E$ ( $\boldsymbol{p}_E \in \mathbb{R}^3$ ) in the world frame as

$$\boldsymbol{R}_{BE} = \mathrm{Rot}(\boldsymbol{y}_B, \eta) = \begin{bmatrix} c_\eta & 0 & s_\eta \\ 0 & 1 & 0 \\ -s_\eta & 0 & c_\eta \end{bmatrix} \tag{4.2a}$$

$$^{B}p_E = [\ 0,\ 0,\ -l_h\ ]^T + \boldsymbol{R}_{BE}[\ l_e,\ 0,\ 0\ ]^T \tag{4.2b}$$

$$= [\ l_e c_\eta,\ 0,\ -l_h - l_e s_\eta\ ]^T \tag{4.2c}$$

$$\boldsymbol{p}_E = \boldsymbol{p} + \boldsymbol{R}_{WB}\ ^{B}\boldsymbol{p}_E\ . \tag{4.2d}$$

Using the Euler-Lagrange formulation, we can derive the equations of motion as

$$\frac{d}{dt}\frac{\partial \mathcal{L}}{\partial \dot{\boldsymbol{\xi}}} - \frac{\partial \mathcal{L}}{\partial \boldsymbol{\xi}} = \boldsymbol{F} = \begin{bmatrix} 0 \\ 0 \\ f_T \\ \tau \\ \tau_\eta \end{bmatrix} \in \mathbb{R}^7 \tag{4.3}$$

$$\mathcal{L} = \mathcal{K} - \mathcal{U}$$

where $f_T \in \mathbb{R}$ is the total thrust along $z_\mathcal{B}$ axis, $\boldsymbol{\tau} = [\tau_x,\ \tau_y,\ \tau_z]^T \in \mathbb{R}^3$ includes the torque vector generated by the four motors, and $\tau_\eta \in \mathbb{R}$ is the torque of the revolute joint. The kinetic $\mathcal{K}$ and potential $\mathcal{U}$ energy of the system are functions of the generalized coordinate variables. For the kinetic energy we have

$$\begin{aligned} \mathcal{K} &= \mathcal{K}_B + \mathcal{K}_E\ , \\ \mathcal{K}_B &= \frac{1}{2} m_B\ \dot{p}^T\ \dot{p} + \frac{1}{2}\ (^{B}\boldsymbol{\omega})^T I_B\ ^{B}\boldsymbol{\omega}\ , \\ \mathcal{K}_E &= \frac{1}{2} m_E\ \dot{p}_E^T\ \dot{p}_E + \frac{1}{2}\ (^{B}\boldsymbol{\omega}_E)^T \boldsymbol{R}_{BE}\ I_E\ \boldsymbol{R}_{BE}^T\ ^{B}\boldsymbol{\omega}_E\ , \end{aligned} \tag{4.4}$$

where $m_B$ and $m_E$ stand for the mass of the main body and end-effector, respectively. The arm that connects to the end-effector has very small mass (less than 10 g) and it is hence excluded from the overall dynamics calculations. The velocity of the end-effector $\dot{p}_{\mathcal{E}}$ can be found by taking the derivative of (4.2d). Here, ${}^{B}\boldsymbol{\omega} \in \mathbb{R}^3$ denotes the angular velocity of the main robot in the body frame while ${}^{B}\boldsymbol{\omega}_E \in \mathbb{R}^3$ stands for the end-effector angular velocity in the body frame. Both angular velocities can be related to the generalized coordinate variables as

$$\begin{aligned} {}^{B}\boldsymbol{\omega} &= (R_{WB})^T T \dot{\Phi} \,, \\ {}^{B}\boldsymbol{\omega}_E &= J_E \dot{\eta} \,, \end{aligned} \tag{4.5}$$

with $T \in \mathbb{R}^{3\times3}$ being the transformation matrix such that $\boldsymbol{\omega} = T\dot{\Phi}$, and $J_E \in \mathbb{R}^{3\times1}$ relating the angular velocity of the end-effector in the body frame to the manipulator's joint angle. The potential energy $\mathcal{U}$ can be calculated as

$$\mathcal{U} = m_B g \; z_W^T \; p + m_E g \; z_W^T \; p_E \,, \tag{4.6}$$

where $z_W = [0 \; 0 \; 1]^T$ denotes the unit vector along $z$ axis in the world frame and $g$ is the gravity constant. By combining the equations above, we can rewrite the dynamic modeling of the entire system as

$$M(\boldsymbol{\xi})\ddot{\boldsymbol{\xi}} + C(\boldsymbol{\xi}, \dot{\boldsymbol{\xi}})\dot{\boldsymbol{\xi}} + G(\boldsymbol{\xi}) = \boldsymbol{F} \tag{4.7}$$

where $M(\boldsymbol{\xi}) \in \mathbb{R}^{7\times7}$ is the inertia matrix, $C(\boldsymbol{\xi}, \dot{\boldsymbol{\xi}})$ is the Coriolis matrix and $G(\boldsymbol{\xi})$ includes gravitational forces. Readers are referred to [92] for details about calculating these matrices.

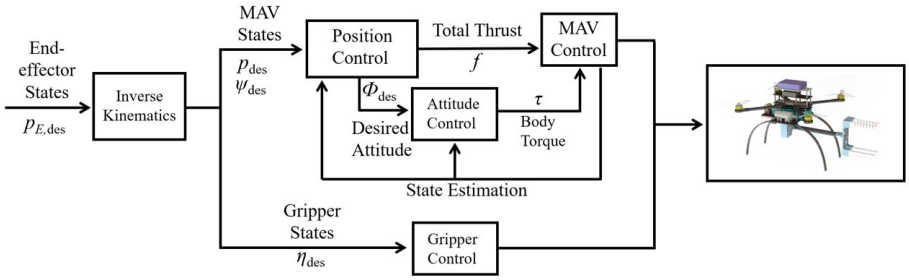


Figure 4.4: A cascaded tracking controller is used in this work to regulate both the vehicle and gripper.

## 4.4 Control

As detailed in Figure 4.4, the controller reads desired states of the end-effector $\boldsymbol{p}_{E,\text{des}}$ from the planner, which will be elaborated in Section 4.5. From (4.2a)—(4.2d), $\boldsymbol{p}_{E,\text{des}}$ is decided by the desired states of MAV $\boldsymbol{p}_{\text{des}}$ and gripper $\eta_{\text{des}}$. Note that both $\boldsymbol{p}_{\text{des}}$ and $\eta_{\text{des}}$ are free variables that can change the end-effector position. We opt to fix the desired angle of the gripper ($\eta_{\text{des}} = 0$ or $\frac{\pi}{2}$). The orientation of the MAV $\boldsymbol{R}_{WB}$ also affects (4.2d). Considering the differential flatness of the MAV system [189], the controller uses a constant desired yaw angle $\psi_{\text{des}} = 0$ while the desired roll $\phi_{\text{des}}$ and pitch $\theta_{\text{des}}$ angles will be calculated based on the desired and actual states of the robot.

To eliminate the assumption of small angles near hovering states, we adopt a nonlinear cascaded tracking control method based on geometric constraints as in [104, 127, 202]. As shown in Figure 4.4, the cascaded control method includes position and attitude controllers. The position controller reads the desired position $\boldsymbol{p}_{\text{des}}$, velocity $\dot{\boldsymbol{p}}_{\text{des}}$, acceleration $\ddot{\boldsymbol{p}}_{\text{des}}$ and yaw angle $\psi_{\text{des}}$, and outputs total thrust $f \in \mathbb{R}$ in body frame and desired attitude $\Phi_{\text{des}} \in \mathbb{R}^3$ as in Chapter 2. The attitude control reads the desired and actual attitude and outputs body torque $\tau$ as in (4.3). With the desired yaw $\psi_{\text{des}}$ directly from the planner,

the desired attitude in Euler angles $\Phi_{\text{des}} = [\phi_{\text{des}},\ \theta_{\text{des}},\ \psi_{\text{des}}]^T$ can be calculated based on the Z-X-Y sequence as

$$\begin{aligned} \boldsymbol{R}_{\text{des}} &= \begin{bmatrix} R_{11} & R_{12} & R_{13} \\ R_{21} & R_{22} & R_{23} \\ R_{31} & R_{32} & R_{33} \end{bmatrix} \\ \phi_{\text{des}} &= \arctan\Big(-\frac{R_{12}}{R_{22}}\Big) \\ \theta_{\text{des}} &= \arctan\Big(\frac{R_{32}}{\sqrt{1-R_{32}^2}}\Big) \end{aligned} \tag{4.8}$$

We adopt a nonlinear attitude control method as in [19]. The attitude controller reads the estimated actual and desired attitude, and outputs the desired angular velocity to the low-level PID bodyrate controller. The nonlinear controller is asymptotically stable, and readers are referred to the report [19] for a thorough analysis. The low-level bodyrate controller is implemented in the PX4 firmware [126].

## 4.5 Planning

Aerial micro-robots are vulnerable to aerodynamic disturbances (e.g., downwash and ground effect) generated by other aerial vehicles [154] or rigid surfaces [82, 85]. Thus, planning for the catching task seeks to generate smooth trajectories that satisfy catching constraints, without producing downwash effect that may destabilize the target aerial robot and while remaining out of ground effect regions that depend on the robot size, propeller length and forward velocity [80]. Trajectory generation for aerial robots has been extensively studied (e.g., [72, 100, 133]). The planner generates smooth desired trajectories for the end-effector based on piecewise polynomials as in [127, 159]. Assuming the path has $m$ segments

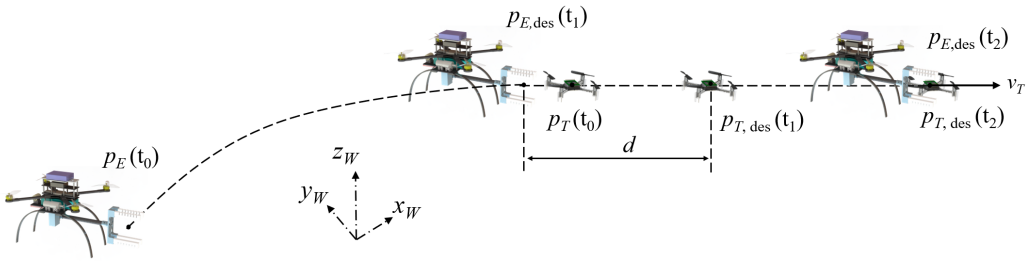


Figure 4.5: Piecewise-polynomial-based planning for a sample catching scenario.

(and therefore we have $m+1$ key frames to apply constraints $t \in \{t_0, t_1, \cdots, t_m\}$), we use $n$-th order polynomial functions to describe the segment $i$ on axis $\mu \in \{x, y, z\}$, considering the desired yaw always set to zero ($\psi_{\text{des}} = 0$). That is,

$$\boldsymbol{\sigma}_{\mu,i}(t) = \boldsymbol{c}_{\mu,i}^T \begin{bmatrix} 1 \\ t \\ \vdots \\ t^n \end{bmatrix}, \quad t \in [t_{i-1}, t_i] \,, \tag{4.9}$$

where $\boldsymbol{c}_{\pi,i} \in \mathbb{R}^{n+1}$ contains coefficients of the polynomial segment. Thus, the desired trajectories can be found by optimizing the objective function

$$J = \sum_{\mu \in \{x,y,z\}} \int_{t_0}^{t_m} || \frac{d^k \boldsymbol{\sigma}_{\mu,i}(t)}{dt^k} ||^2 dt \,. \tag{4.10}$$

Following the minimum-snap formulation [127], we minimize the snap along the trajectory, so $k = 4$ and $n = 7$. Then, the trajectory generation can be reformulated as a quadratic program,where $\boldsymbol{c} \in \mathbb{R}^{3m(n+1)\times 1}$ that contains all polynomial constants can be found as

$$\begin{aligned} \min \quad & \boldsymbol{c}^T H \boldsymbol{c} \\ \text{s.t.} \quad & A\boldsymbol{c} \leq b \,, \end{aligned} \tag{4.11}$$

$$\boldsymbol{c}_i = \begin{bmatrix} c_{x,i} \\ c_{y,i} \\ c_{z,i} \end{bmatrix} \quad \boldsymbol{c} = \begin{bmatrix} \boldsymbol{c}_1 \\ \boldsymbol{c}_2 \\ \vdots \\ \boldsymbol{c}_m \end{bmatrix} . \tag{4.12}$$

The constraint $A\boldsymbol{c} \leq b$ in (4.11) is described next. As shown in Figure 4.5A, the target aerial robot is assumed to follow a constant velocity $\boldsymbol{v}_T = \dot{\boldsymbol{p}}_T$ in the world frame. The position of the target is measured as $\boldsymbol{p}_T(t_0)$ in the world frame at time $t_0$. Projected positions of the flying target are denoted as $\boldsymbol{p}_{T,\text{des}}(t)$ at time $t$ based the constant velocity assumption. We use $\boldsymbol{p}_E(t_0)$ to denote the initial gripper position where $t_0$ is the starting time. Similar to related work [162], we separate a catching task into three segments (`chase`, `close` and `grasp`), with three key frames to apply optimization constraints ($t_1$ and $t_2$). In the `chase` part ($t \in [t_0, t_1]$), the end-effector of the robot tracks a trajectory from $\boldsymbol{p}_E(t_0)$ to the position $\boldsymbol{p}_{E,\text{des}}(t_1)$, which lies along the direction of $\boldsymbol{v}_T$ with a distance of $d \in \mathbb{R}$.

$$\begin{aligned} \boldsymbol{p}_{E,\text{des}}(t_1) =& \boldsymbol{p}_{T,\text{des}}(t_1) - \boldsymbol{R}_{WT}(d\frac{\boldsymbol{v}_T}{||\boldsymbol{v}_T||}) , \\ \boldsymbol{p}_{T,\text{des}}(t_1) =& \boldsymbol{p}_T(t_0) + (t_1 - t_0)\boldsymbol{v}_T , \\ \dot{\boldsymbol{p}}_{E,\text{des}}(t_1) =& \boldsymbol{v}_T . \end{aligned} \tag{4.13}$$

In the `close` segment ($t \in [t_1, t_2]$), the end-effector moves from $\boldsymbol{p}_{\mathcal{E},\text{des}}(t_1)$ to the projected position of the flying target $\boldsymbol{p}_{E,\text{des}}(t_2) = \boldsymbol{p}_{T,\text{des}}(t_2)$ with the constant velocity $\dot{\boldsymbol{p}}_{E,\text{des}}(t_2) = \boldsymbol{v}_{\mathcal{T}}$. At time $t_2$, the end-effector is automatically triggered to start inflating to grasp the target. The key frame $t_1$ is calculated where $t_2 = t_1 + \tau_1$, $t_3 = t_2 + \tau_2$, where $\alpha$, $\tau_1, \tau_2 \in \mathbb{R}$ are constants.

$$t_1 = t_0 + \alpha||P_{\mathcal{T}} - P_{\mathcal{E}}(t_0)||_2 , \tag{4.14}$$

## 4.6 Experimental Results

Results are categorized based on three types of tests: grasping, catching, and flyability. In the grasping test, the soft gripper is studied against a commercially available gripper, mounted on a Kinova Gen3-lite robot for response and static catching tests. In the catching experiment, the target aerial robots hovers at a fixed position with tracking errors. After taking off manually, the developed SoAG robot generates and tracks a trajectory automatically to catch the flying target as described in Section 4.5. Finally, we study the free flight tracking performance of the robot with different arm and gripper states compared to a conventional quadrotor.

All experiments rely on motion capture camera systems (VICON and OptiTrack) for odometry feedback. The feedback is only used to estimate the states of the robots, which can also be achieved by cameras or laser sensors in outdoor environments. The Crazyflie 2.1 with MoCap deck is used as the target aerial robot, with a total weight of 0.035 kg. The developed SoAG robot measures 0.38 m from the motor tip to tip, with a total weight of 1.64 kg. A 3-cell 5200 mAh LiPo battery is used to power the entire system. Key parameters for different tasks can be found in Tab. 4.1.

Table 4.1: Key Parameters of the Developed SoAG Robot

| $m_{\mathcal{B}}$ | $m_{\mathcal{E}}$ | $l_e$ | $l_h$ | $d$ | $\alpha$ | $\tau_1$ | $\tau_2$ |
|---|---|---|---|---|---|---|---|
| 1.526 kg | 0.115 kg | 0.32 m | 0.14 m | 0.5 m | 2 | 1.5 s | 2 s |

### 4.6.1 Grasping

In this experiment, both grippers are placed vertically at the same 3D position. The position of both claw tips is measured using the OptiTrack motion capture feedback in 100 Hz. We use gaps in millimeter to denote the position difference along the $z_{\mathcal{W}}$ axis. Figure 4.6a presents the result of the response test, where black solid and dashed curves denote the gaps of the soft and Gen3-lite grippers, respectively. Similarly, orange solid and dashed curves stand for the input signals for the soft and Gen3-lite grippers. The input value of 1 means both grippers close (inflate) at the fastest speed. For the input value of 0, the valve opens to enable ventilation of the actuators for the soft gripper, and for the gripper mounted on the Gen3-lite, it opens at the fastest possible speed.

As shown in Fig. 4.6a, we command the soft gripper to close and open for 3 s, while the Gen3-lite gripper is controlled to close for 3 s and open for 5 s. The Gen3-lite gripper has an initial opening of 136 mm, larger than the one of the soft gripper (117 mm). However, the soft gripper completely closes after 0.72 s, while it takes 1.90 s for Gen3-lite gripper to do so, with closing velocities 162.50 and 71.58 mm/s for the soft and Gen3-lite grippers, respectively. Large amounts of noise are observed when the soft gripper completely closes. The noise comes from the rigid-body-based motion capture system model, and the fact that inflated soft actuators have shape changes which introduce measuring errors. On the other hand, unlike the same speeds of the Gen3-lite gripper, the soft gripper has a much faster response for opening, with only 0.24 s to reach 85% of the initial gap. The normally-straight actuators with the flexible 80A support recover very fast with basic ventilation. Admittedly, the response of both grippers can be improved by having more powerful motors or inflators.

However, the low-cost soft gripper introduced in this work has good performance powered by lightweight air pumps, compared to commercially available end-effectors like the Gen3-lite gripper.

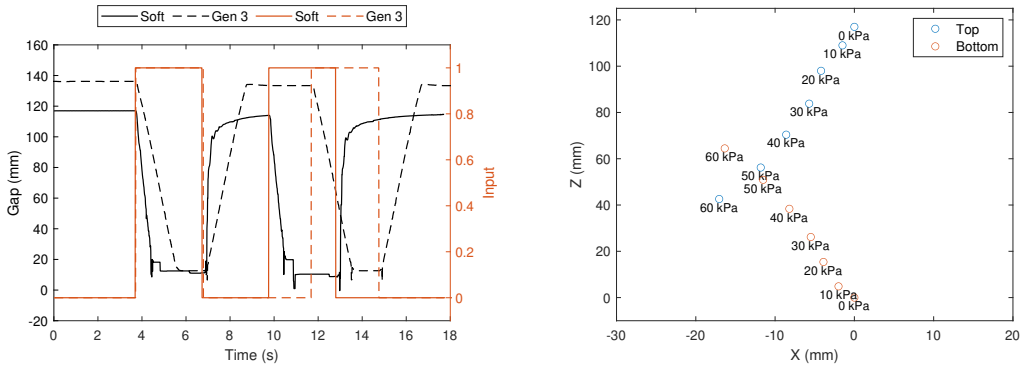


(a) Response (b) Relative Position

Figure 4.6: Grasping test for the soft and Gen3-lite grippers. (a)Step response for both grippers. (b) Relative positions of the soft gripper's two claws with respect to different pressure values.

Second, positions of the soft gripper's two claws (top and bottom) are studied with respect to different pressure values. Gauge pressure, which is the pressure relative to atmospheric pressure. The end-effector is placed vertically along $z_{\mathcal{W}}$ with the gap facing $-x_{\mathcal{W}}$, while the origin is located at the bottom claw in absence of pressurization. Figure 4.6b shows relative positions of top (blue) and bottom (red) claws when pressurized separately. The results indicate that the top claw has larger vertical deformation than the bottom one with the same pressure value due to gravity. However, both claws have much smaller horizontal deformation than the vertical one. The results also indicate the gripper completely closes when the pressure value reaches 50 kPa.

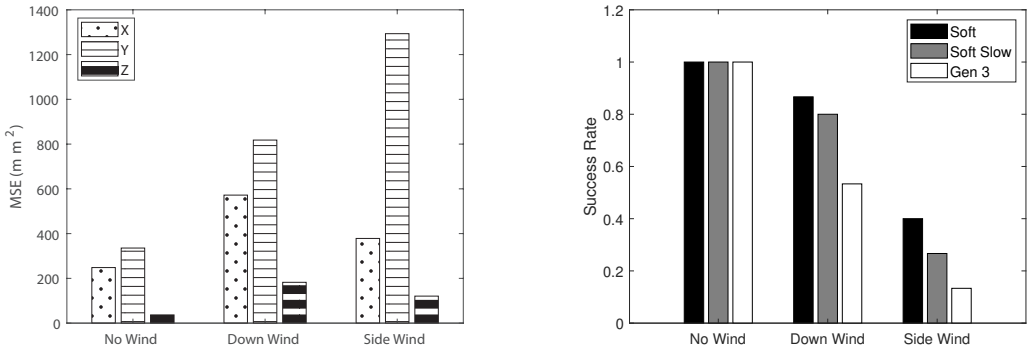


(a) MSE

(b) Success Rate

Figure 4.7: Mean squared error for a hovering micro-robot under disturbances. (b) Success rates for horizontal grasping of a flying micro-robot using both grippers.

Figure 4.7a presents the mean squared error (MSE) between actual and desired hovering positions in three cases. Results show that the hovering micro-robot has larger tracking errors under these disturbances, especially along $y_{\mathcal{T}}$ axis. Fifteen grasping trials are conducted for each gripper in each case, and all success rates are visualized in Fig. 4.7b. Both grippers have good performance in the no-wind case. However, the soft gripper shows advantages in both down- and side-wind cases, owing to its ability to adapt to different shapes. Both grippers struggle in grasping in the side-wind case, due to the large tracking errors and grippers' limited reachability along $y_{\mathcal{T}}$ axis. To study the individual contributions of both the softness and closing velocity, one additional case (Soft Slow) is studied when we slow the closing speed of the soft gripper to 71.58 mm/s by outputting only 0.88% of the maximum voltage (10.56 /12 V) to air inflators during pressurization. Results show that the soft gripper has similar grasping performance in the down-wind case with a reduced closing speed, however, the success rate drops when the disturbance rises in the side-wind case, supporting the significance of a fast closing speed.

Lastly, we study the maximum force applied by both grippers to validate the catching safety. A digital force gauge is used to measure vertical force along $z_{\mathcal{W}}$ axis applied by the top claws of both grippers. Results show that the Gen 3-lite gripper has a maximum grasping force of 23.7 N while the soft gripper can only produce forces up to 0.63 N, which result in safe interactions with aerial targets. In the meantime, the developed soft gripper is experimentally proven able to grasp and hold (both horizontally and vertically) irregular objects such as multi-meters, pressure gauges and game controllers, with masses up to 280 g. The test validates the developed soft gripper can grasp most aerial micro-robots, as well as other irregular objects to function as a universal gripper.

### 4.6.2 Catching

#### Static Case

In this test, we study the feasibility of using the developed SoAG robot to catch an aerial micro-robot that is hovering. The target $p_{\mathcal{T}}$ hovers at the position $[1.0,\ 1.0,\ 1.0]^T$ with tracking errors as in Fig. 4.7a. The target's position and velocity information are available to the catcher via motion capture feedback at all times. The end-effector of the catcher $p_{\mathcal{E}}$ starts with an initial position $[-0.68,\ 0,\ 1.0]^T$. The catcher robot generates and follows trajectories as in Section 4.5 with parameters listed in Tab. 4.1.

A sample trial is presented in Fig. 4.8, where images depict events when the SoAG robot approaches the target (A), grasps the target (B), and returns (C) with the target. Figure 4.8a shows the state tracking for the end-effector and target, where black solid and dashed curves denote the actual and desired positions of the end-effector in $x_{\mathcal{W}}$ and $y_{\mathcal{W}}$

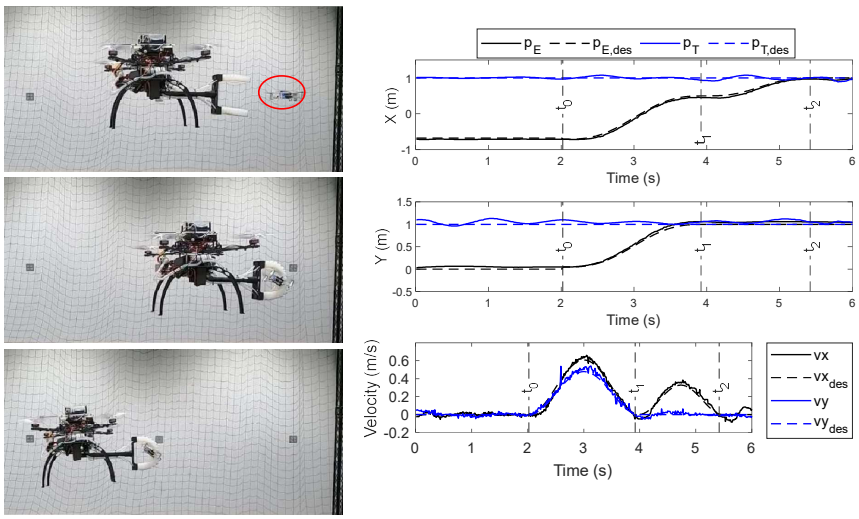


(a)

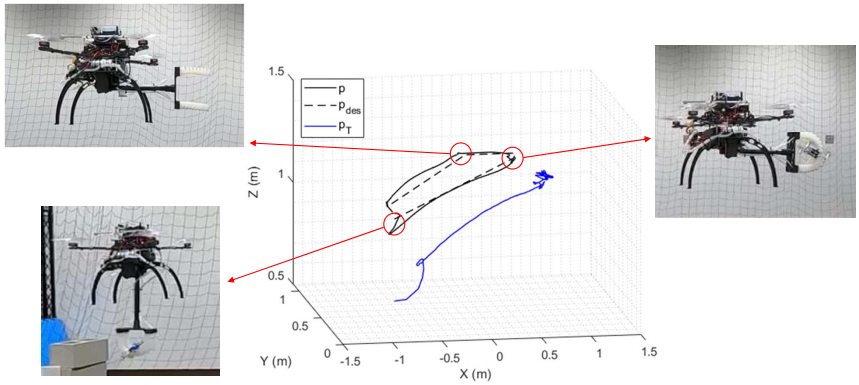


(b)

Figure 4.8: A sample trial of the static catching test. (a) The snapshots of SoAG robot approaching the target, grasping the target, and returning with the target, as well as states tracking for the end-effector and target. (b) 3D positions of the SoAG robot and the target aerial robot.

directions. Similarly, blue solid and dashed curves represent the actual and desired positions of the target. The bottom figure shows the actual and desired velocities of the end-effector along $x_{\mathcal{W}}$ and $y_{\mathcal{W}}$ axis. The time gap $\tau_1$ is calculated per (4.14). Since $\tau_2$ is a constant, key frames to apply constraints are found as $t_1 = 3.92$ s, $t_2 = 5.42$ s and $t_3 = 7.42$ s with a starting time $t_0 = 2.02$ s. The figure demonstrates the good tracking performance of the SoAG robot with the planned smooth trajectory. The results also show the target

has very small tracking errors before and during the grasping, which supports the claim that horizontal grasps do not produce aerodynamic disturbances detrimental to the target's stability.

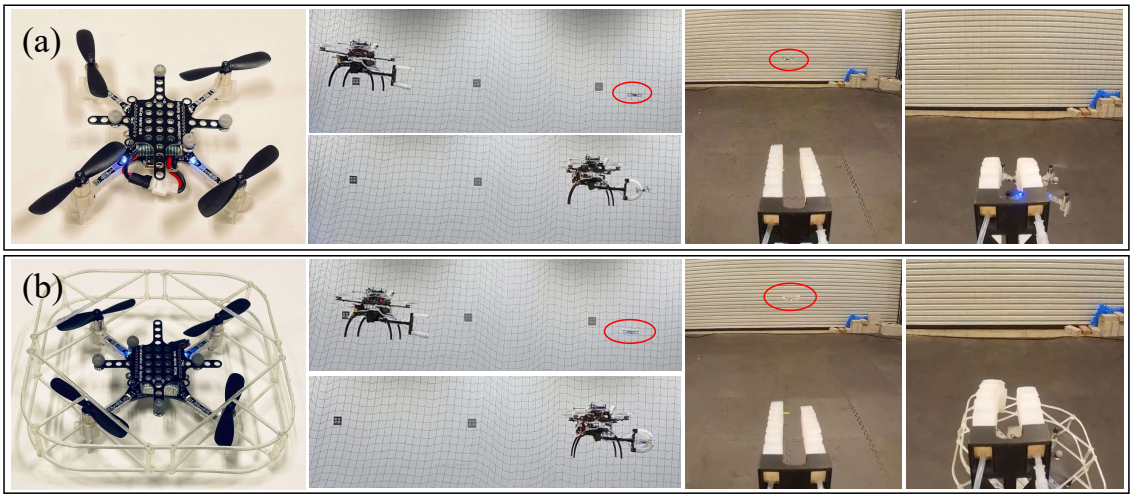


Figure 4.9: Close-up images of the flying targets without (A) or with (B) propeller guards, as well as side views and first-person views of the aerial captures.

The actual and desired 3D positions of the SoAG robot are plotted in Fig. 4.8b, as well as the target's 3D position. The robot has larger tracking errors during the `chase` segment, and smaller errors for the `close` part. The results back up the planning method in piecewise polynomials to achieve small tracking errors before the grasping. Note that random noise is still present in the target's hovering position, which makes aerial catching more challenging. Owing to the robustness of the soft gripper, the catcher robot manages to grasp the target and return with it. At the end of the trajectory, SoAG rotates the arm to place the target at a lower position and gets ready to drop the target safely.

While the related work [25] relies on the contact with the propeller guards, our method can catch flying micro-robots with or without protective frames. In this part, we

study the robustness of the soft gripper by introducing the catching test of flying targets with propeller guards. Figure 4.9 shows close-up images of the flying targets used in the tests with (B) or without (A) propeller guards. The flying micro-robot with the protective frame has a dimension of $130 \times 130 \times 40$ mm, and a total mass of 40 g. The custom propeller guard is 3D-printed using the Form 3 in clear resin, which has the post-cured ultimate tensile strength 65 MPa. We repeat the static catching tests on flying targets, and the robot can successfully capture hovering micro-robots regardless of the propeller guards. Figure 4.9 presents side and first-person views of the aerial catching in both cases, where red ellipses mark hovering micro-robots. As shown in first-person views, the robot can catch flying targets even though the gripper is not in align with the center of the target, thanks to the robustness of the soft grasping. In the meantime, the observation that aerial catching does not damage the fragile propeller guards further support the safety of our method.

**Dynamic Case**

In this test, we study the feasibility of dynamically catching an aerial micro-robot that is following a path. The flying target takes off at the position $[-1.0, 0, 1.0]^T$ and moves along $x_{\mathcal{W}}$ with a constant velocity of 0.2 m/s. The SoAG robot hovers at the position $[-2.0, 0, 1.0]^T$ before the dynamic catching is manually triggered. The robot reads the actual position and velocity of the target via motion capture feedback at time $t_0$ and plans the trajectory as described in Section 4.5.

A sample dynamic catching trial is shown in Fig. 4.10, where the SoAG robot triggers the catching (a), starts inflating (b), finishes grasping (c), and enters hovering state

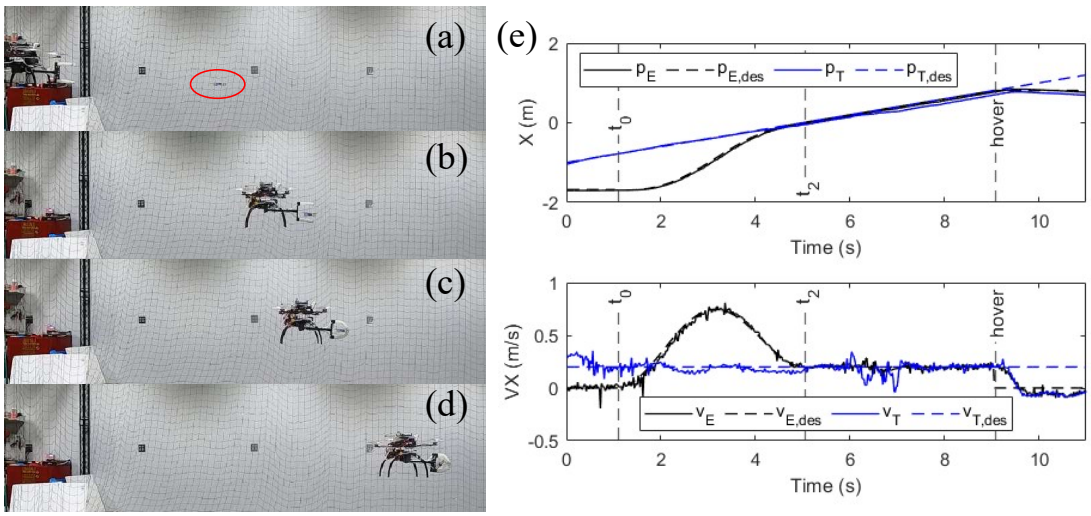


Figure 4.10: A sample trial of the dynamic catching test. (a to d) The SoAG robot approaches, reaches and grasps the moving aerial target. (e) State tracking for the end-effector and moving target.

(d). Figure 4.10e visualizes the actual and desired states tracking of both the catcher and target robots. Due to the limited space of the experimental area, the catcher robot hovers at a position relatively close to the flying target, thus the planning skips the `chase` segment. The results show that the planner generates a smooth trajectory for $t \in [t_0, t_2] = [1.1, 5.2]$ to reach the same position and velocity of the target. At time $t_2$, the SoAG robot starts inflating the end-effector to grasp the target, and keeps the constant velocity for another 4 s before the hovering state.

The position profile in Fig. 4.10e shows that the robot is tracking the desired trajectory well. After the grasping, the target's position has a small deviation from the desired one. Both the catcher and target robots remain the same position during the hovering. On the other hand, velocities tracking shows that the target has relatively larger tracking errors compared to the catcher, especially after the grasping. The catcher robot follows the smooth desired velocities well to reach and maintain the target velocity $v_{\mathcal{T}}$ before

the hovering state. The dynamic catching test supports the robot's potential applications to rescue or intercept moving aerial targets. Compared to the related work [25], our method can capture moving aerial targets while staying relatively static to minimize impact.

### 4.6.3 Flyability

In this experiment, we study the effect of the arm and target on the free flight tracking performance of the catcher. Five cases are considered in the test: conventional quadrotor (Quad), SoAG with arm up and without target (Up w/o), SoAG with arm up and seized target (Up w/), SoAG with arm down and without target (Down w/o), and SoAG with arm down and seized target (Down w/). The angle $\eta = 0$ when the arm is up, and $\eta$ is $\frac{\pi}{2}$ for the arm-down case. Note that Quad (conventional quadrotor built in-house without any gripper) has a total weight of 1.035 kg including the battery while the target's weight is 35 g. Due to a smaller weight, tuning parameters are different for Quad , while other four cases share all variables. The experiment comprises two parts: step response and planar circle tracking. In the step response test, all robots hover at the point $[0, 0, 1]^T$ before the planner sends discrete setpoints $[0, 0, 2]^T$, $[1, 0, 2]^T$ and $[1, 1, 2]^T$ at 5 s intervals. For the second test, all robots track a planar circle trajectory centered at the point $[0, 0, 1]^T$ with a radius of 1 m. The circle starts from the point $[1, 0, 1]^T$ with a period of $2\pi$ s.

Figure 4.11 shows the states for all robots in the step response test. Green dashed curves show desired states from the planner, and black dashed and solid curves show the response of the SoAG robot with the arm lifted. Blue dashed and solid curves denote the response of the robot when the arm is down. Note that the time is synchronized solely

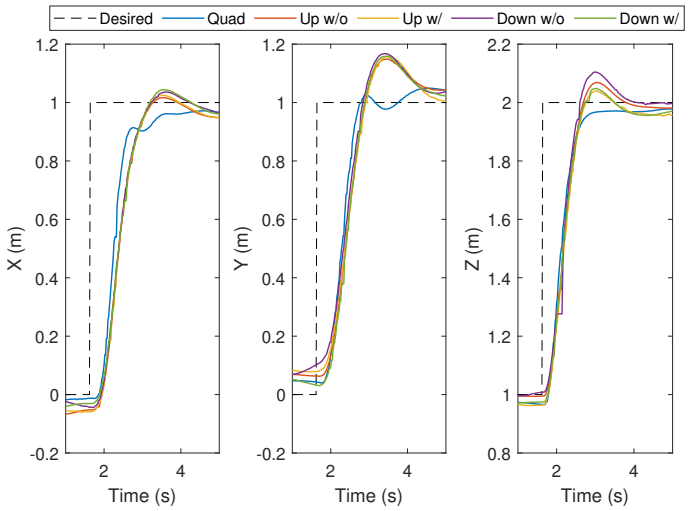


Figure 4.11: Mean squared error for a hovering micro-robot under disturbances. (b) Success rates for horizontal grasping of a flying micro-robot using both grippers.

in the visualization for better comparison. The results show that Quad has a faster rising time compared to the other four cases in both $x_{\mathcal{W}}$ and $y_{\mathcal{W}}$ directions due to reduced weight. However, the response along $z_{\mathcal{W}}$ axis is similar for all robots since it aligns with the thrust direction. On the other hand, the SoAG robot has a very close step response in different arm and gripper states, which demonstrates that the rigid arm and soft gripper designs do not compromise the flyability of the aerial robot. A similar conclusion can be made in the planar circle test as shown in Fig. 4.12, which visualizes positions and velocities on $x_{\mathcal{W}}$ and $y_{\mathcal{W}}$ axis. The green dashed curve shows the desired states for the circle trajectory, with a jump on the velocity along $y_{\mathcal{W}}$ in the beginning. Due to the discontinuity, the SoAG robot has a slower converging rate compared to Quad in the first 2 s. All robots have good position and velocity tracking on $y_{\mathcal{W}}$ axis afterwards. The desired trajectory is smooth in the $x_{\mathcal{W}}$ direction, thus, all robots have good tracking performance throughout the test.

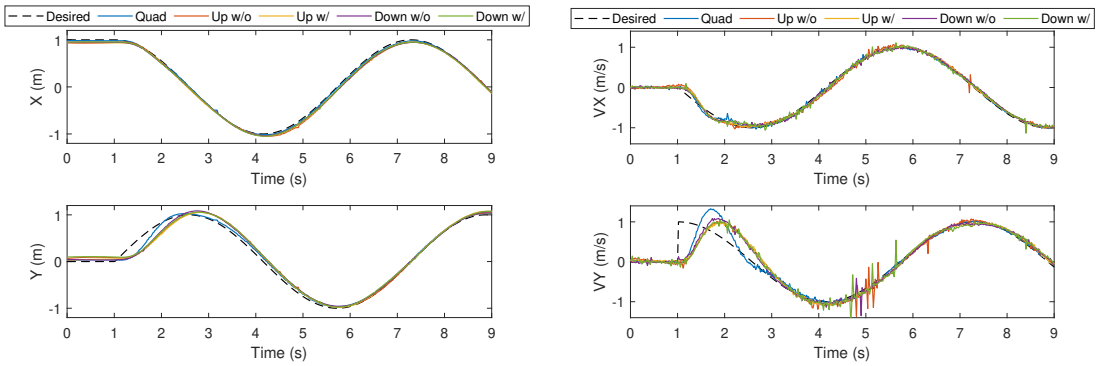


(a) Position (b) Velocity

Figure 4.12: Mean squared error for a hovering micro-robot under disturbances. (b) Success rates for horizontal grasping of a flying micro-robot using both grippers.

## 4.7 Conclusions

In this chapter, we focus on addressing studying effects of compliance on robot-robot interactions. In other words, we present an innovative solution on catching aerial micro-robot in mid-air using another MAV equipped with a soft gripper. Specifically, we introduce a gripper design based on soft actuators that keep a horizontally straight shape with a single fixture and maintain sufficiently compliance when bending. To enable horizontal grasping, we further develop a MAV equipped with the end-effector and onboard pneumatic regulation named Soft Aerial Gripper (SoAG). The hardware design is introduced, as well as the dynamic modeling and control. We present a planning method based on piecewise polynomial optimization to catch the flying micro-robots without generating aerodynamic disturbances detrimental to the target's stability.

Experimental results show the low-cost soft gripper, powered by light weight air pumps that are onboard the robot, has fast opening and closing responses as compared to commercially available end-effectors. Static grasping tests study the soft gripper's ro-

bustness in capturing aerial micro-robots under the influence of aerodynamic disturbances. We experimentally demonstrate the feasibility of using the SoAG robot to catch a hovering micro-robot and return with the target. The free flight performance of the SoAG robot is studied against a conventional quadrotor and in different gripper and payload status to validate the design. To the authors' knowledge, the SoAG robot is the first MAV to demonstrate the feasibility of catching a flying micro-robot with a soft gripper. The robot can be used in search and rescue of aerial robots or seize unidentified flying targets without damage. In the meantime, the robot can move fragile objects as a conventional aerial gripper, with potential applications in aerial transportation and construction.

In the next chapter, we extend the study to variable-stiffness legged robots for traversing rough terrain. We introduce an innovative soft hexapedal robot (SoRX) that utilizes a novel 2-DoF soft pneumatic actuators. We propose an alternating tripod gait for the robot and demonstrate that the method is highly effective for locomotion in various terrains, including flat, rough, steep, and unstable surfaces.

# Chapter 5

# Gait Generation and Motion Control of a Soft Hexapedal Robot

In this chapter, we examine the compliance in the legged locomotion to traverse rough terrain. Specifically, we develop i) a new 2-degree-of-freedom soft pneumatic actuator, and ii) a novel soft robotic hexapedal robot called SoRX that leverages the new actuators. Simulation and physical testing confirm that the proposed actuator can generate cyclic foot trajectories that are appropriate for legged locomotion. Consistent with other hexapedal robots (and animals), SoRX employs an alternating tripod gait to propel itself forward. Experiments reveal that SoRX can reach forward speeds of up to 0.44 body lengths per second. The motion capabilities of SoRX are evaluated through five experiments: running, step climbing, and traversing rough terrain, steep terrain, and unstable terrain.

This chapter is organized as follows: Section 5.1 discusses background and related works for compliant legged robots; Section 5.2 shows the design and properties of the novel

actuator, as well as simulated results based on finite element analysis; We discuss the robot and the gaits in Section 5.3. Finally, we evaluate the motion capabilities of the robot in Section 5.4.

## 5.1 Background

Multi-legged robots show promise in application areas such as search-and-rescue where operation over rough and unstructured terrain is expected. However, achieving all-terrain mobility remains a challenging task, especially as robots scale down in size [96]. Adaptation to terrain variations is key for taking the robots outside of the protected laboratory environment, and deploying them in real-world settings. Studies have indicated that incorporating compliant legs, as animals do, can significantly improve the speed and stability of these robots in varying environmental conditions [167]. Among the first efforts to incorporate passive mechanical compliance within a robot's legs was the springy C-leg in the hexapedal robot RHex [5, 134, 171], which is still commonly used nowadays. Tunable devices were proposed to adjust the stiffness of legs [52, 63, 76]. Direct-drive legged robots were also developed to achieve variable compliance (e.g., [6, 77, 89, 179]). There have been other attempts to achieve tunable stiffness using antagonistic pneumatic actuators such as McKibben actuators and pleated pneumatic artificial muscles [198, 208]. However, these compliant legs come together with rigid parts, which limit the contact area along the length of legs, therefore reducing the ability to navigate rough terrain.

Soft robots are particularly appropriate for locomotion in uneven and/or sensitive environment, because their soft structure allows them to bend and squeeze to fit their shape

around obstacles, and reduce the stress induced by contact over both surroundings and the robot's surface [31]. In particular, soft robotics have been investigated and developed for locomotion applications. Prior work includes soft robots powered by soft pneumatic actuators (SPA) to achieve crawling and undulation gaits [58, 181, 204]. A starfish-like soft robot was developed to complete crawling gaits actuated by shape memory alloys [120]. However, the actuators of these robots only have only one degree of freedom (DoF). Meanwhile, they are unable to traverse over rough terrain as more rigid legged robots do. Notable exceptions include a robot that combines soft legs with wheels for navigation on uneven terrain [169], and a soft-material 3D-printed pneumatic legged robot able to lift its legs off the ground and walk over unstructured terrain [46]. Nevertheless, these robots rely on either rigid wheels or multiple leg configurations to achieve all-terrain locomotion. Moreover, unlike hexapedal robots, they cannot sustain a large support area, as with an alternating tripod gaits, which can be advantageous when traversing uneven terrain [197].

There are other attempts to achieve soft legged locomotion by leveraging cable-driven actuators. The Sofia walking robot [50] and Puppy [15] utilize model-based optimal control to achieve walking locomotion. The cable-driven legs have 2 DOFs: bending and extension. Compared to pneumatic ones, cable-driven actuators may be more direct to model and control. However, cable-driven actuators can be challenged when it comes to varying leg stiffness to adapt to terrain variations. Moreover, the necessary motors may render cable-driven robots top-heavy and thus unstable [15].

## 5.2 Actuator Design and Analysis

### 5.2.1 Design

To design an all-terrain soft legged robot, each leg must be sufficiently compliant to adapt to obstacles, while stiff enough to support the robot's weight. One promising way to balance this trade-off is by utilizing soft pneumatic actuators (SPAs). Prior works on SPAs for legged locomotion have relied on pneumatic networks (PneuNets) [181] and multiple bellowed chambers [46]. However, these actuators can only bend but not extend, which may constrain the locomotion capabilities of the robot in practice.

To mitigate this challenge, we introduce the SPA design shown in Fig. 5.1. The actuator consists of two parts: 1) the bending part, which is adopted by the original PneuNet design with one cut remaining, and 2) the extension part, which employs a Hyper-Elastic Bellows (HEB) actuator design [42]. When the two parts are pressurized, the actuator can both bend and extend; different pressurization/depressurization cycles can then yield a multitude of distinct foot trajectory profiles.

### 5.2.2 Simulated and Physical Analysis

Simulation was conducted to guide the design and to ensure the proposed design can work as intended in real-time. We used Finite Element Method (FEM) analysis to simulate large non-linear deformations undergone by soft structures, by following the analysis in [49]. In sum, at each step $i$ of the real-time simulation, the internal forces are linearized as

$$f(x_i) \approx f(x_{i-1}) + K(x_{i-1})dx \ , \tag{5.1}$$

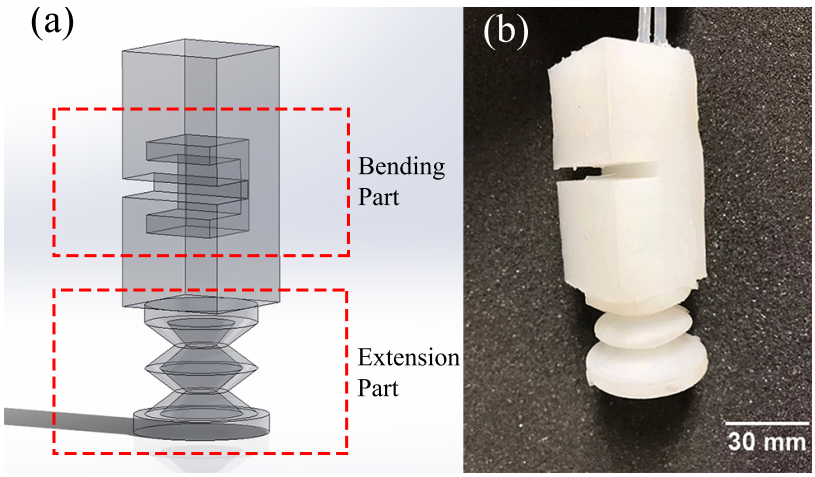


Figure 5.1: (a) CAD rendering, and (b) a physical actuator prototype.

where $f$ is the volumetric internal stiffness force at the nodes, and $K(x)$ represents the tangent stiffness matrix. Assuming quasi-static motions, the model is in equilibrium in terms of internal and external forces, that is

$$-K(x_{i-1})dx = p + f(x_{i-1}) + J^T\lambda \ , \tag{5.2}$$

where $p$ stands for the external forces, $\lambda$ represents the contributions of the actuators and the contact forces (if applicable) and $J$ gathers the directions [49].

To solve for node displacements, we first find a free configuration $x^{\text{free}}$ by solving (5.2) with $\lambda = 0$. The result also yields $\delta^{\text{free}}$ which is the violation for constraints. Then, a constraint-based solver computes $\lambda$ given laws of the constraint between $\delta$ and $\lambda$, that is

$$\delta = \underbrace{\left[JK^{-1}J^T\right]}_{W}\lambda + \delta^{\text{free}} \ . \tag{5.3}$$

Finally, node displacements are calculated using the value of the constraint response [49]

$$x_t = x^{\text{free}} + K^{-1}J^T\lambda \ . \tag{5.4}$$

All steps are implemented in SOFA [4] with SoftRobotPlugin [32]. The mesh file consists of $13,344$ tetrahedra and $3,352$ nodes. To build a precise simulation, elastic and inertial parameters have to be tuned in simulation. The Young's modulus is obtained from silicone's properties while the mass of the actuator is measured experimentally [17]. shows simulation results when the actuator is pressurized and depressurized. Comparisons between trajectories in simulation and in physical testing are given in Sec. 5.3. The actuator's properties regarding extension, bending, and stiffness-varying have a significant impact on its utility to soft legged robots. To this end, we conducted empirical tests to validate simulation results, and to evaluate the performance of the physical prototype.

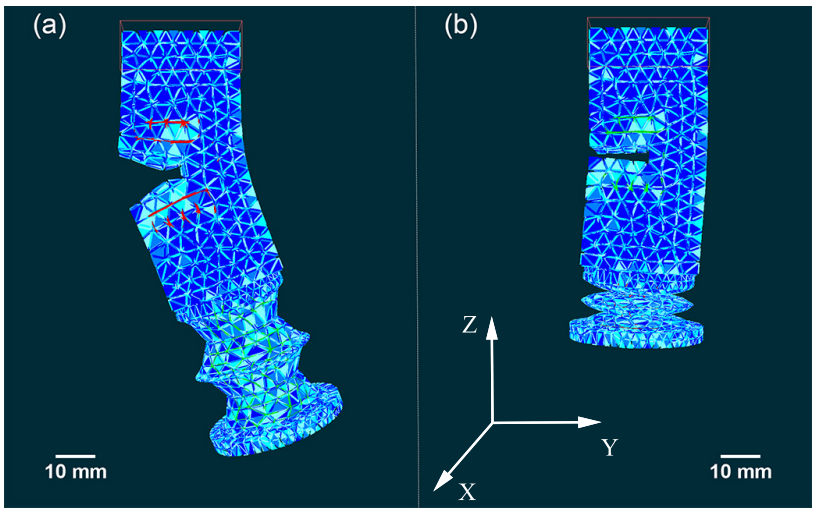


Figure 5.2: FEM analysis of leg (a) pressurization and (b) depressurization in the SOFA environment. Each tetrahedron represents the FEM force field. Node displacements demonstrate changes in shape.

In the extension and bending tests, the actuator was mounted horizontally (see Fig. 5.3). Both extension and bending parts are pressurized/depressurized at 2.5 kPa in-

crements. The position of the actuator's free end was recorded in the extension test. In simulation, the direction of gravity points to the negative direction along Y-axis to match the experimental setting (see Fig. 5.2). To represent the additional rigidity created by the silicone tube in the bending part, we used a model of stiff springs in the direction of the tubes [30]. We exported the position of the corresponding node via a Python script in SOFA. Extension test results (Fig. 5.3) show the experimentally-measured values match the simulation data. The extension part can elongate by 48 mm at 30 kPa and be shortened by 9 mm in depressurization. It is worth mentioning that the simulation diverged when pressure values extended beyond the range of $[-2, 10]$ kPa.

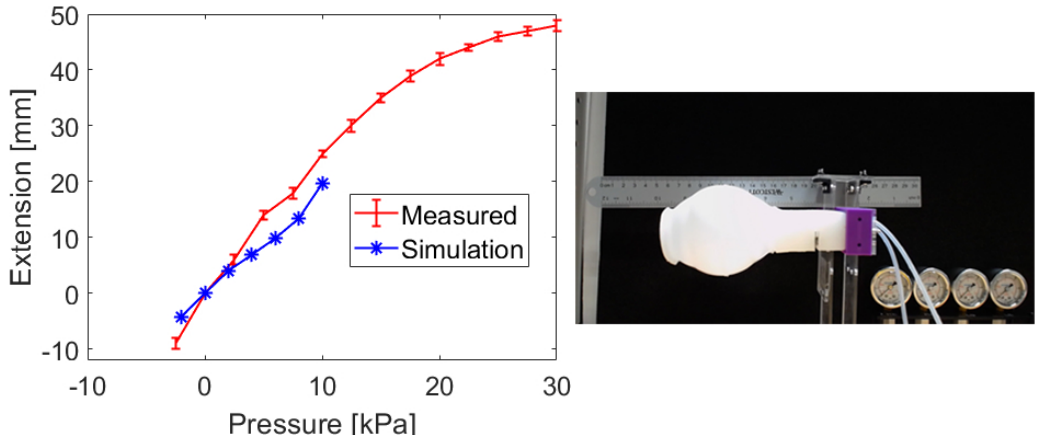


Figure 5.3: Results and experimental setup for the extension test. Negative pressure numbers relate to depressurization (vacuum) mode of the air source.

In the bending test we measured bending angles as input pressure varies. Results (Fig. 5.4) show that the actuator can bend 91 deg at 60 kPa. However, angles in simulation are smaller than the measured ones. Further, simulations diverged when the input pressure exceeded 30 kPa.

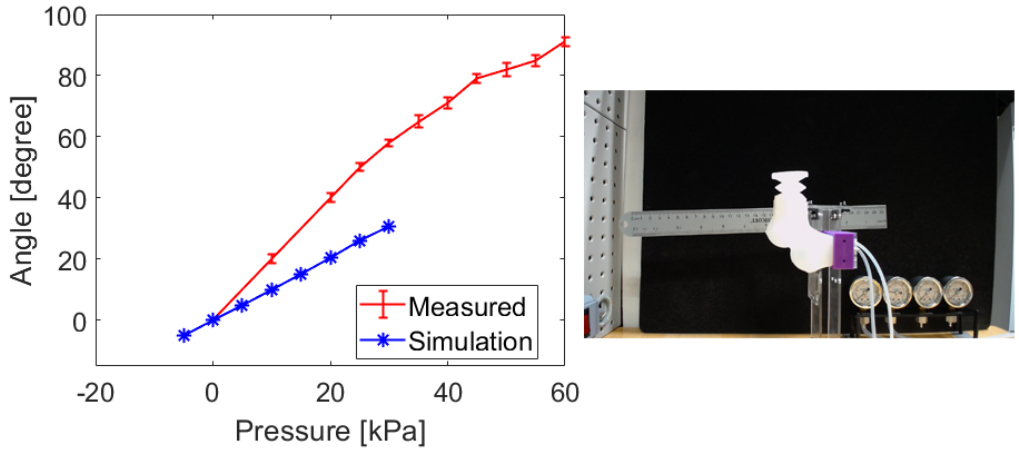


Figure 5.4: Results and experimental setup for the bending test.

In both tests, we observed some mismatch between the measured and simulated results. This mismatch may be caused by approximations in material properties such as Young's modulus and Poisson ratio, measurement errors, and vibrations caused while the actuator was pressurized. Material properties may vary due to fabrication, e.g., it is very difficult to remove all air bubbles during casting despite using a degassing chamber.

Moreover, we measured the force generated by the actuator as a function of the input pressure to illustrate the actuator's stiffness-varying property. In this test, the actuator was mounted vertically above a load cell with amplifier HX711 and microcontroller Arduino Mega (Fig. 5.5). The actuator was in contact with the load cell when the pump was switched off. Input pressure values ranged from 0 kPa to 20 kPa. Results indicate that the actuator can apply 10.67 N at 20 kPa. As such, our hexapedal robot can lift a maximum weight of 3.26 kg when it follows an alternating tripod gait.hat is, three legs are touching the ground at all times. However, as pressure increases over a critical point, the leg will passively bend; this effect can lead to the sharp increase observed in Fig. 5.5.

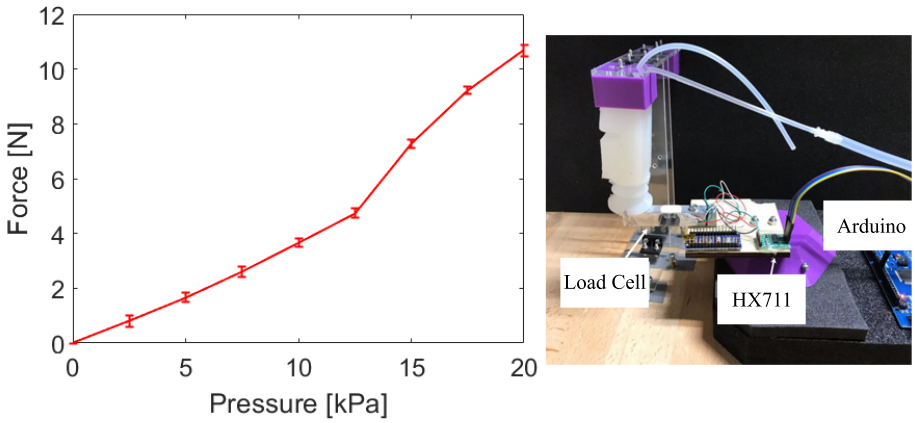


Figure 5.5: Results and experimental setup for the stiffness-varying test.

### 5.2.3 Actuator Fabrication

Each actuator is cast separately out of two-part silicone elastomer (Dragon Skin 10 FAST, Smooth-On). Three pairs of 3D-printed molds (Onyx material on Markforged Mark Two carbon fiber 3D printer) are used to form shapes (Fig. 5.6). The bending part consists of two pieces: the chamber and button layer, which are molded separately. Overall, fabrication of a leg takes place in four steps. 1) Mix the elastomer and process it in vacuum chamber to remove bubbles. 2) Pour it into the molds and wait 75 minutes for it to cure, and demold the pieces. 3) Use an adhesive (Sil-Poxy, Smooth-On) to bond together the two pieces of the bending part. Meanwhile, glue two same silicone bodies made by mold (c) in Fig. 5.6 to form the extension part. 4) Insert silicone tubes for air connection and bond the two actuator parts.

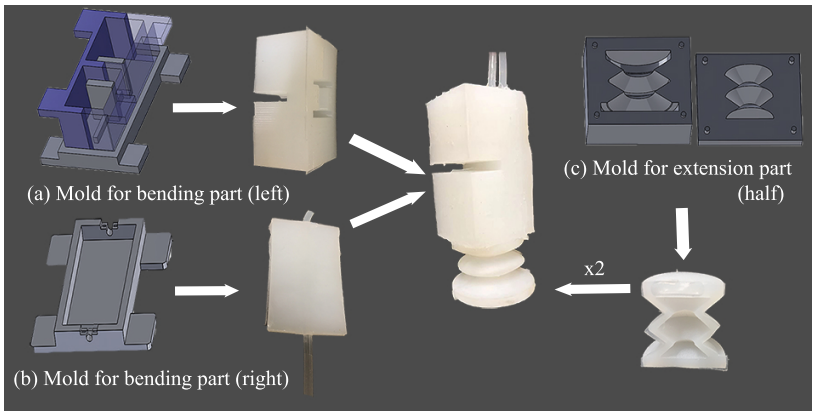


Figure 5.6: Fabrication of the soft pneumatic actuator

## 5.3 Robot Implementation and Gait Analysis

The new soft actuators are used to create the pneumatically-actuated soft robotic hexapod SoRX (Fig. 5.7). SoRX measures 230 mm L × 140 mm W × 100 mm H and weighs 650 g. The frame of SoRX was manufactured by combining laser-cut wood and acrylic sheets (Universal Laser Systems VLS 3.60 laser cutter), and six 3D-printed leg holders (Makerbot Replicator+ 3D printer). Like RHex [172] and DASH [18], among other hexapods, SoRX employs an alternating tripod gait for locomotion. Static stability is guaranteed with alternating tripods by keeping the center of mass within the support area formed by the three legs that touch the ground.

To achieve effective locomotion we need to determine appropriate cyclic control trajectories for the robot's feet. However, determining pressurization/depressurization sequences for pneumatically-actuated soft legged robots is a challenging task. As shown shortly, available simulation tools yield quite different results from those observed in practice. In this work, we identified empirically a pressurization/depressurization sequence that

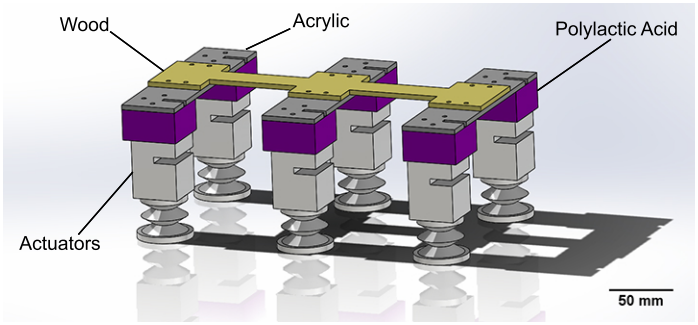


Figure 5.7: CAD of SoRX and materials.

can lead to effective locomotion. The sequence is shown in Fig. 5.8(a). Bending and extension parts are pressurized sequentially, and then they are depressurized simultaneously. Temporal duration ratios remain fixed; changing the total cycle time leads to different forward velocities.

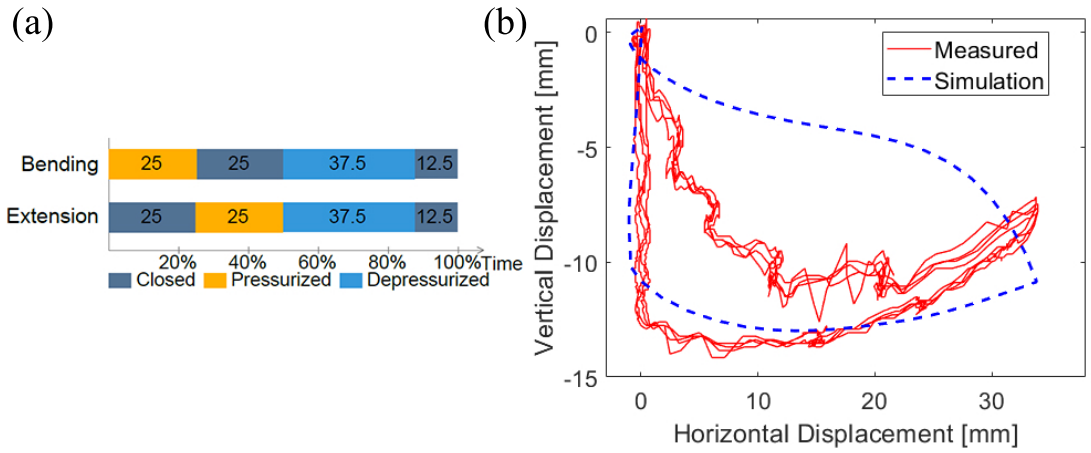


Figure 5.8: (a) Empirically-derived actuation sequence for one leg stride. (b) Resulting simulated (in blue) and experimental (in red) foot trajectories.

To identify the nominal foot trajectory, the actuator was mounted vertically as in the stiffness-varying test. The vertical axis points to the opposite direction of gravity, thus the vertical displacements are negative. An entire actuation sequence was applied to the

actuator while the camera recorded motion. Resulting image frames were post-processed and analyzed with the video analysis software Kinovea. Meanwhile, the same actuation sequence was applied in simulation. Resulting trajectories are shown in Fig. 5.8b. We notice that the foot returns to its original starting point after one stride despite the very compliant nature of the leg. A maximum foot clearance of about 14 mm was recorded. Device vibrations may cause non-smooth points in the trajectory. Further, we noticed that the bending part tended to respond faster to differential pressure inputs than the extension part. The last two points are the major differences between simulation and experiment (i.e. trajectories are smoother, and actuators respond equally fast in simulation). These differences may be caused by the various approximations noted previously, but also by the fact that the simulation relies on the assumption of quasi-static motions, which is not met in rapid actuation cycles needed in practice.

## 5.4 Experimental Results

The motion capabilities of SoRX were evaluated through five experiments: running, step climbing, and traversing rough terrain, steep terrain, and unstable terrain. A modified version of an open-source pneumatic control board [73] was used in all experiments. In our board, every air output channel is connected to two pairs of valves and pumps to allow for both pressurization and depressurization. A 12-camera VICON motion capture system was used to collect position and velocity data of the center-of-mass (CoM) of SoRX.

### 5.4.1 Walking

SoRX was able to reach a top speed of 0.44 body lengths per second (BL/s), or 101 mm/s, at maximum actuation pressures of 34 kPa for the bending part and 10 kPa for the extension part. Figure 5.10 depicts an instance of the robot running. Compared to other soft robots, SoRX can run significantly faster both in terms of body length and absolute distance (Table 5.1). To the best of our knowledge, SoRX is the fastest to date pneumatically-actuated soft legged robot.

Further, we performed running tests at two distinct speeds set at 0.35 BL/s and 0.44 BL/s, to capture the evolution of the position of SoRX's CoM in forward motion. Results reveal that the robot's CoM follows a repeatable cyclic pattern (Fig. 5.9). This observation is consistent with the CoM evolution of more rigid legged robots, suggesting that related tools to study stability and to design motion planners and controllers may be appropriate for soft legged robots as well.

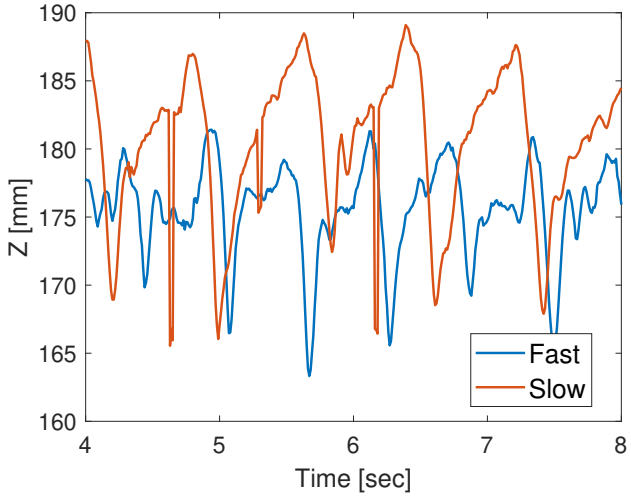


Figure 5.9: CoM position evolution in the Z axis at two different forward speeds, 0.44 BL/s (in blue) and 0.35 BL/s (in red), indicating that the robot's CoM follows a cyclic pattern.

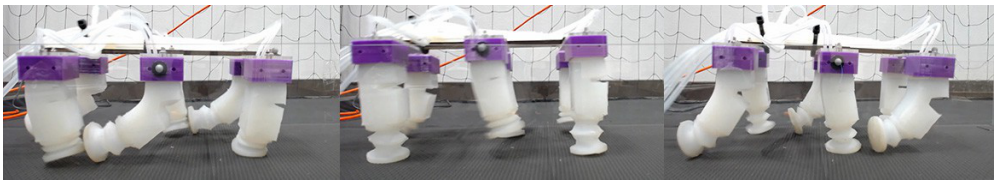

Figure 5.10: Snapshots in 0.5 sec intervals of SoRX running.

Table 5.1: Speeds for soft robots

| Robots | Speed [BL/s] | Speed [mm/s] |
|---|---|---|
| SoRX | 0.44 | 101.0 |
| Quadrupedal [46] | 0.14 | 20.0 |
| Puppy [15] | 0.12 | 15.6 |
| Multigait [181] | 0.05 | 6.7 |
| Five-limb [120] | 0.003 | 0.43 |

### 5.4.2 Step Climbing

SoRX was able to overcome obstacles up to 15 mm tall passively and while following the same alternating tripod gait used for running (Fig. 5.11). Leg softness appears to play a dual positive role. First, it can improve locomotion robustness by enabling SoRX to recover when one leg gets stuck on the obstacle. Second, it may help overcome obstacles larger than the nominal foot clearance. (Recall the nominal foot clearance was measured at 14 mm in static single-leg tests shown in Fig. 5.3.) In both cases, a leg may forcibly squeeze or over-extend beyond the range prescribed through its actuated values without any damage if forces remain below the silicone's yield point.

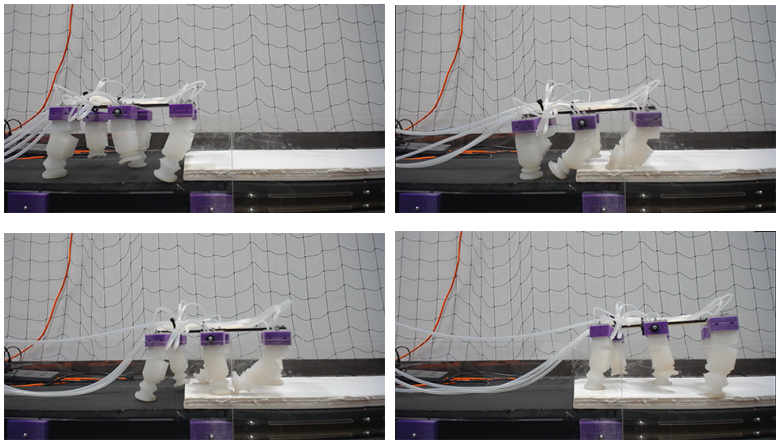

Figure 5.11: SoRX climbing over a 15 mm-tall stack of foam board.

### 5.4.3 Traversing Rough Terrain

To evaluate the robot's capability to traverse rough terrain, we considered locomotion over sand, rocks, and a mixed terrain (Fig. 5.12). The mixed terrain consisted of two flat ground parts at the two ends, as well as sand and rocks parts in the middle. The supplementary video offers a clear illustration of our experiments.

The speed of SoRX while traversing rough terrain is compared to the speed of Quadrupedal [46]. Quadrupedal was tested with small pebbles and large rocks. Therefore, the speed of SoRX over sand is compared to the one of Quadrupedal over small pebbles. Results (shown in Fig. 5.13) demonstrate that SoRX is able to navigate much faster on all types of terrain. Unlike Quadrupedal, SoRX uses one leg configuration that is adequate for flat ground and rough terrain alike. The speed of SoRX over mixed terrain suggests that keeping the same gait pattern and control effort may suffice to traverse different types of terrain.


Figure 5.12: SoRX was found capable to traverse (a) sand, (b) rocks, and (c) mixed terrain.

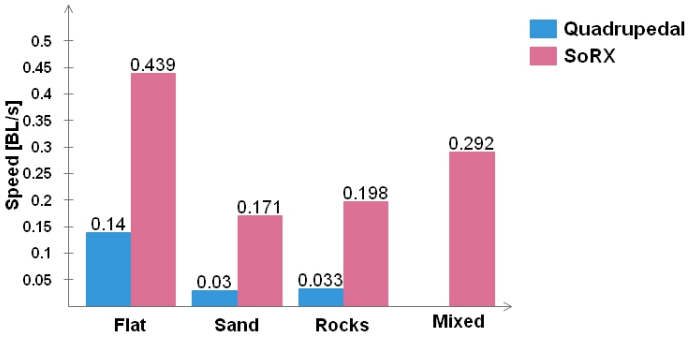


Figure 5.13: Terrain traversal speeds for Quadrupedal and SoRX.

### 5.4.4 Traversing Steep Terrain

Walking over inclined surfaces has been a challenging task for all legged robots. A spherical soft robot [196] was able to climb a slope with crawling gaits. Puppy [15] can walk up a hill only in simulation.

Two experiments were implemented to test SoRX's locomotive performance on steep terrain: 1) walking on an inclined flat surface, and 2) walking inside an inclined groove. The robot was able to climb up to a 10 deg angled flat surface made of acrylic sheet as shown in Fig. 5.14a while employing the same alternating tripod gait as in running over flat and rough terrain and climbing over a step. Moreover, the robot was able to traverse a 15 deg inclined groove made of two flat acrylic sheets as shown in Fig. 5.14b. The actuators can bend and squeeze to fit the high-slop surface. Unlike Quadrupedal, SoRX does not require any additional leg configuration to handle steep terrain.

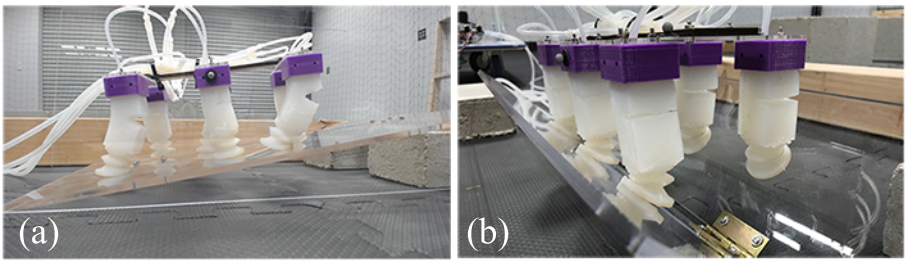


Figure 5.14: (a) SoRX climbing up a slope of 10 deg. (b) SoRX shown inside an inclined groove where actuators bend and squeeze to adapt to the high-slope surface.

### 5.4.5 Traversing Unstable Terrain

To further evaluate the robustness of SoRX's running performance, we commanded SoRX to run on an unstable (oscillating) platform. The experimental setup consisted of four caster wheels supporting a wooden sheet; see Fig. 5.15a. The platform oscillated in the X-Y plane while SoRX was running on top of it.

Figure 5.15b superimposes the speed of SoRX and of the oscillating platform's as measured through motion capture. SoRX was able to run on the platform without tipping over despite the platform oscillating at speeds comparable to the robot's forward velocity. The employed alternating tripod gait, paired with soft legs appear to yield a robust running performance in spite of the unstable (oscillating) terrain.

## 5.5 Conclusions

In this chapter, we presented SoRX, a novel pneumatically-actuated soft hexapedal robot. SoRX utilizes our new 2-DoF soft pneumatic actuators that can both bend and extend to create foot trajectory profiles that are appropriate for legged locomotion. Consistent with other hexapedal robots (and animals), SoRX employs an alternating tripod gait to pro-

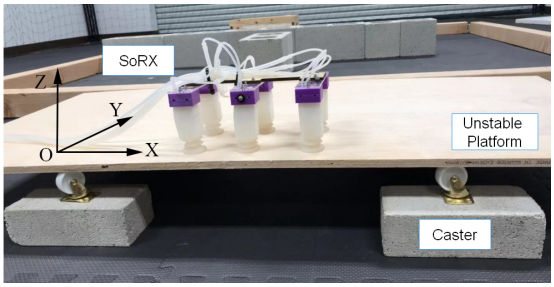


(a)

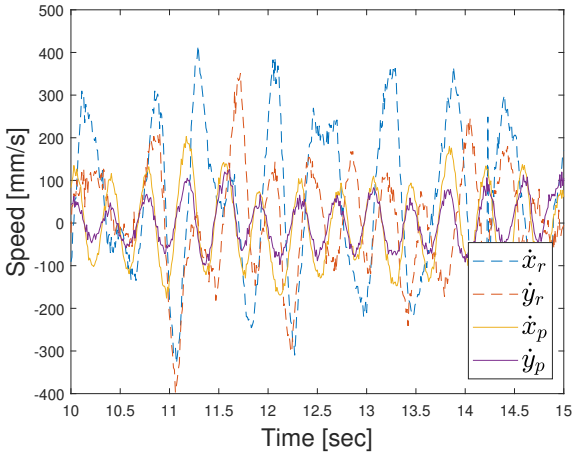


(b)

Figure 5.15: (a) Experimental setup for the unstable terrain testing. Terrain is oscillating in the X-Y plane at speeds comparable to the robot's forward speed, topping at approximately 200 mm/s. (b) Superimposed platform (solid curves) and robot (dashed curves) speeds for the unstable terrain testing. $(\dot{x}_p, \dot{y}_p)$ and $(\dot{x}_r, \dot{y}_r)$ denote the platform and combined robot and platform speeds, respectively.

pel itself forward. We showed that the alternating tripod gait can be utilized for effective locomotion of SoRX while traversing flat, rough, steep, and unstable (oscillating) terrains. Experiments reveal that SoRX can reach forward speeds of up to 0.44 BL/s, which to the authors' best of knowledge makes it the fastest soft pneumatically-actuated legged robot to date. The robot can climb over 15 mm tall obstacles, walk over terrains that contain rocks, sand, and combination of those, climb up to 10 deg slope, and walk inside 15 deg

inclined grooves. SoRX is also capable to run on an unstable platform oscillating at speeds comparable to the robot's forward speed without tipping over. These results suggest that compliance introduced through a purely soft leg design may create new opportunities for legged robots to navigate over challenging terrains.

In the next chapter, we present a static model for feedforward position control of the robot. With the aim of deploying the robot in outdoor environments, we propose a fast and precise air pressure feedback controller that utilizes a custom low-cost pneumatic regulation board. We further propose a closed-loop trajectory tracking method to enable the robot to track variable-height trajectories trajectories.

# Chapter 6

# Modeling and Trajectory Tracking of a Soft Hexapedal Robot

In this chapter, we extend the study on compliant legged robot to include modeling and trajectory tracking. Specifically, we present a static model for feedforward position control (body height and orientation) of our soft pneumatic legged robot SoRX. With the aim of deploying the robot in outdoor environments, we design and develop a novel low-cost pneumatic regulation board that powers up to 8 channels of pressurization/depressurization with air pressure feedback. By utilizing this board, we propose a novel fast and precise air pressure feedback controller. Taking advantage of the proposed model and novel pneumatic regulation system, we further propose a closed-loop trajectory tracking method to enable the robot to track variable-height trajectories trajectories.

This chapter is organized as follows: Section 6.1 discusses background and related works for modeling and trajectory tracking of soft legged robots; Section 6.2 presents the

modeling and the parameter identification; We discuss the controller design in Section 6.3,as well as the trajectory tracking in Section 6.4. Finally, we show both indoor and outdoor tests Section 6.5.

## 6.1 Background

Multiple types of rigid robots (e.g., industrial robots used in manufacturing) have been successfully endowed with rapid and precise motion control capabilities [28]. However, the high stiffness of the body, as well as the high-gain feedback control can introduce a risk of bodily injuries, especially in cases where interactions with humans are involved [168]. In response, in recent years there has been a fast-growing interest in the development and control of *soft robots*. Soft robots can enable safe interaction with humans, high power-to-weight ratio, adaptation to the interacting environment, and comparatively lower fabrication cost [155].

Various actuation methods have been developed for soft robots. Some representative examples include pneumatic [95, 168], hydraulic [121], cable-driven [15] and shape-memory alloy (SMA) [120] systems. Among those methods, pneumatic actuators have been observed to facilitate legged robots' adaptation to various types of terrain, thus making them a suitable candidate for use in the context of robotic locomotion [45, 46]. Our previous work introduced a soft pneumatic actuator with two degrees of freedom (DoFs) that can both bend and extend to create foot trajectory profiles suitable for legged locomotion [112]. Utilizing that actuator, we developed a novel soft hexapedal robot (SoRX) that can operate over a range of challenging environments, such as rough, steep, and unstable terrain, with-

out any additional control effort and by following the same feedforward control strategy (an alternating tripod gait scheduler) across all terrains [84].

However, these soft pneumatic legged robots have limitations as they rely on empirically hand-tuned input sequences for open-loop control. Meanwhile, a lack of mathematical models makes it hard to utilize model-based controllers for precise motion control. Recent related work has introduced a soft pneumatic legged robot powered by electronics-free pneumatic circuits [47]. However, the robot still requires tethered manual control for locomotion and collision avoidance.

### 6.1.1 Related Works

Model-based motion control for soft pneumatically-actuated robots has been a challenging task due to the nonlinear properties of soft materials and generally slow responses to actuation [155]. Past research on soft pneumatic robots' modeling and control has mostly focused on single actuators or soft manipulators. Model-based control of continuum manipulators with relatively higher stiffness has been well-studied. Piecewise constant curvatures [22,122] and variable curvature models [119] have been proposed to achieve feedforward control. Other attempts include Cosserat rod [48], mass-damper-spring-based [69], linear parameter-varying [155], and finite element method-based [17] models. Those models have then been used to develop various feedforward or feedback control methods, including proportional-integral-derivative (PID) [17], sliding mode [188], model predictive control [16] and learning-based methods [184, 203].

However, these methods are significantly limited in their application to the control of soft pneumatically-actuated legged robots in three main ways. 1) The methods usually fail

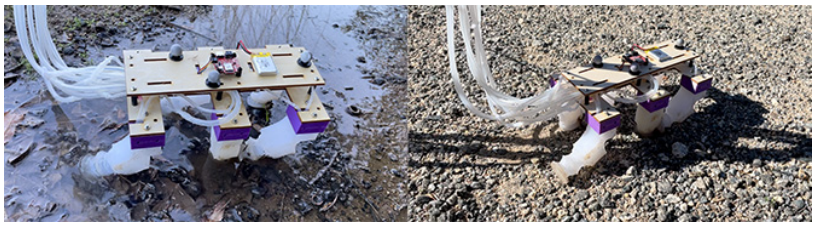

Figure 6.1: Outdoor operations for SoRX on natural unstructured terrain.

to incorporate frequent and periodic interactions with the environment, which are common in legged locomotion. 2) A large majority of methods only take a small number of actuators into account, while controlling soft legged robots is more complicated since the robots usually have at least four legs and each leg has at least two actuated DoFs. 3) The methods require relatively costly and large valves or pressure sources for fast and precise airflow regulation; high cost prohibits scaling to multiple channels of actuation while the size and weight restrict mobility.

Past research on motion control of soft pneumatic mobile robots has primarily focused on planar locomotion, featuring soft robotic snakes [117, 144, 156]. However, those robots rely on traditional rigid wheels for contacting with the surface, limiting the ability to adapt to various terrain. A recent work presents a continuum soft robot capable of tracking trajectories and interacting with the environment [39]. Nevertheless, robot movement is still limited to 2D space.

## 6.2 Modeling and Parameter Identification

SoRX has been shown to reach high (relative to scale) walking speeds across various types of terrain [112]. The efficient walking performance mainly comes from the leg design

that can bend and extend to create foot trajectory profiles suitable for legged locomotion (see Fig. 6.2a). In fact, walking tests in [112] indicate that SoRX's center of mass (CoM) displays trajectories similar to those observed in traditional hexapedal robots and which are often modeled by the spring-loaded inverted pendulum (SLIP) model [18].

However, the SLIP model is unfeasible to be applied on soft pneumatic legged robots for two reasons. First, the weight of legs of SoRX accounts for more than 80% of the total weight (excluding the pneumatic control board). Second, the relatively slow response to pressure inputs make it inappropriate to implement the dynamic modeling of rigid parts. In contrast, prior research on soft pneumatic fingers has shown the feasibility of using geometric models in real-time position control [199].

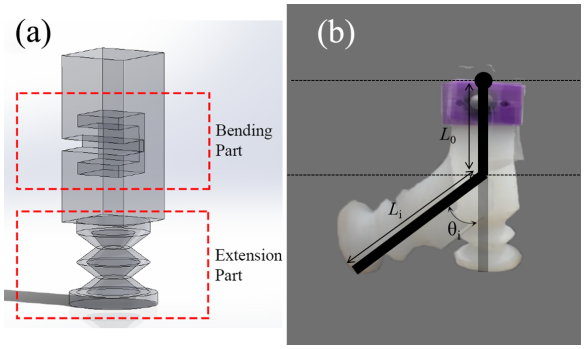


Figure 6.2: (a) CAD rendering of the leg design, and (b) the proposed static model based on geometric constraints.

### 6.2.1 Static Model

In this work, we propose a static model based on geometric constraints for each leg (see Fig. 6.2b). We use one revolute and one prismatic joint to model the bending and extension parts, respectively. Parameters $\theta_i$ and $L_i$ are used to denote joints' values for leg $i = 1, \ldots, 6$. Note that $L_i$ include both the length of the extension part and the distance

to the cut of the bending part. Using the model for single legs, we can further model the whole robot (see Fig. 6.3). Six legs are connected to a planar body frame of length $L_B$ and width $W_B$. The length of leg $i$ can be written as $L_0 + L_i$ where the $L_0$ is a constant that denotes the distance from the bending part to the robot's frame. The Euler angles of the robot planar frame are used to represent the robot's orientation.

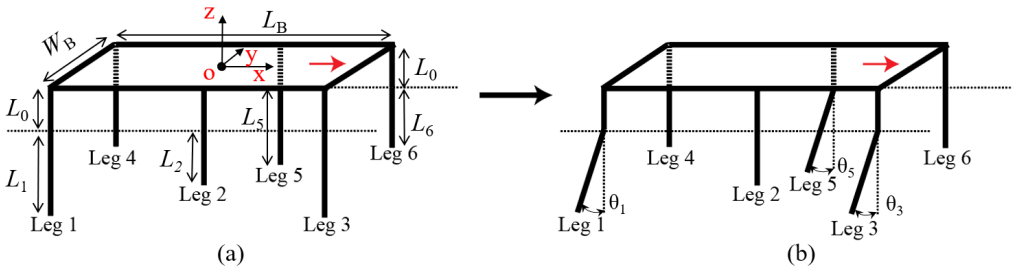


Figure 6.3: Modeling SoRX's quasi-static forward motion.

By design, there are two steady states for a single tripod gait: 1) only the extension part actuated (Fig. 6.3a), and 2) both parts actuated (Fig. 6.3b). In the first state, the extension parts of the tripod $\{1, 3, 5\}$ elongate and lift the body, then the bending parts are actuated and create angles $\{\theta_1, \theta_3, \theta_5\}$ to propel the robot forward. Both extension parts $L_i$ and bending parts $\theta_i$ depressurize when the other tripod actuates to support the robot.

We compute the robot's height and orientation with respect to parameters $L_i$ and $\theta_i$. It is important to note that we use the height of the geometric center of the robot's planar frame to denote the robot's height (point $o$ in Fig. 6.3a) as well as its Euler angles to represent the robot's orientation. Consider tripod $\{1, 3, 5\}$ is pressurized. Then, the height of the robot can be written as

$$h = L_0 + \frac{L_1 + L_5}{2} \quad . \tag{6.1}$$

By design, we set $L_1 = L_3, \quad L_4 = L_6$ in all phases of the alternating tripod gait. The robot's roll angle along $x$ axis is

$$\phi = \text{atan}(L_5 - L_1, \frac{W_B}{2}) \tag{6.2}$$

### 6.2.2 Pressure Model and Parameter Identification

In this work is that we implement a feedback pressure control for precise pneumatic regulation (to be elaborated in Section 6.3). To derive that controller, it is first crucial to determine the relation between model parameters $L_i$ and $\theta_i$ with pressure $p$, which is needed for the robot's feedforward position control. Deriving analytically an accurate model of air dynamics in the actuators can be quite complicated; yet, examining the measured experimental data as a function of input air pressure, we can approximate the model using polynomials.

Table 6.1: Test Cases for Extension Part Modeling

| | |
|---|---|
| $\text{one}_{w/o}$ | Single-leg tripod side actuated, other side not actuated |
| $\text{one}_{w/}$ | Single-leg tripod side actuated, other side pressurized (30 kPa) |
| $\text{two}_{w/o}$ | Double-leg tripod side actuated, other side not actuated |
| $\text{two}_{w/}$ | Double-leg tripod side actuated, other side pressurized (30 kPa) |

To determine the relation between input pressure and output leg length, we perform a series of extension tests. We place the robot on flat ground, pressurize the extension

part of the legs within a single tripod, and record the pressure (kPa, gauge) as well as the length (mm) of the actuated legs in steady state. Since the robot's legs are not massless and the length of the extension parts is sensitive to the load, preliminary testing revealed asymmetries to the response of the extension parts on the two sides of a tripod. To study this asymmetry within a tripod, we thus test the two sides of a tripod (i.e. the side with one leg and the other side with two legs) separately. Within these two cases, we further study two sub-cases in which the legs of the not-active side are either not actuated or pressurized at a constant pressure of 30 kPa, which is used in the experiments.The four considered cases and their respective notations are contained in Table 6.1. Note that in double-leg cases, we measure the length of both legs and record the average.

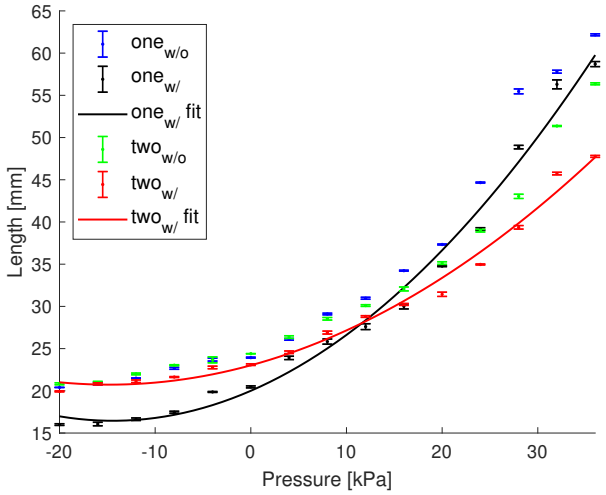


Figure 6.4: Relations between input pressure and output leg length.

We apply pressure inputs (gauge) ranging from $-20$ kPa to 36 kPa with sampling interval of 4 kPa. Actuators have higher risk to break when input pressure exceeds 36 kPa. Four distinct measurements are taken for every sampled pressure input. Figure 6.4 depicts mean values and one-standard deviations for all four cases shown in Table 6.1. Experimental

results confirm asymmetries on two sides of the tripod. Moreover, the double-leg tripod side is observed to have larger decrease in the elongation with the same positive pressure when the other side pressurized while the single-leg tripod side displays a larger decrease in length with the same negative pressure.

We select to approximate relations where the other sides are actuated ($\text{one}_\text{w}, \text{two}_\text{w}$) as the pressure models since two sides of the tripod are actuated for most of the tests. The experimental results the relations can be approximated by second-order polynomials. The curves are plotted in Fig. 6.4 as $\text{one}_\text{w/}$fit and $\text{two}_\text{w/}$fit. On the other hand, for the angle $\theta$ model, we approximate the relation between input pressure and bending angle $\theta$ presented in our previous work [112]. Polynomial coefficients for all models are listed in Table 6.2.

Table 6.2: Polynomial Coefficients for Model Fitting

| **Models** | **Polynomials** | **Units** | **Ranges** |
|---|---|---|---|
| $\text{one}_\text{w/}$ | $0.017p^2 + 0.492p + 53.801$ | mm | [-20, 36] kPa |
| $\text{two}_\text{w/}$ | $0.010p^2 + 0.309p + 56.821$ | mm | [-20, 36] kPa |
| $\theta$ | $0.010p + 0.0153$ | rad | [-20, 50] kPa |

## 6.3 Controller Design

### 6.3.1 Pneumatic Regulation Board

In our prior work [112], SoRX was driven by a modified version of an open-source pneumatic control board [74]. In that board, every air output channel was connected to two

pairs of valves and pumps to allow for both pressurization and depressurization. Instead of free-flow passive deflation, active depressurization significantly improves the walking performance since it can accelerate bending legs to recover to upright configurations. At the same time, active depressurization can further shorten the extension parts, thus increasing foot clearance to facilitate overcoming obstacles. The pneumatic regulation board proposed herein builds upon principles of the previous configuration and also includes pressure sensors (gauge) to provide feedback.

In this work, we use custom printed circuit boards (PCBs) for the pneumatic regulation board to minimize size and weight. The PCB design is based on a portable open-source pneumatic controller with minor changes to the operational amplifier circuit for pressure sensors. A top view of our developed pneumatic regulation board is shown in Fig. 6.5. There are in total six pumps (red circles) and 16 solenoid valves on the board. Half of them are used for pressurization; the other half are responsible for depressurization. There are three types of valve boards: 1) boards with three valves and one pressure sensor (red box), 2) boards with two valves and one pressure sensor (white box), and 3) boards with only one pressure sensor (green box). Three micro-controllers (Arduino Nano, yellow ellipses) coordinate with the companion computer (Odroid XU4 [not shown in image]) to read pressure values as well as control valves and pumps. Electronics are powered by a 3500 mAh 3-cell LiPo battery. The board has a compact design (240 mm L x 420 mm W x 140 mm H), and weighs 1.7 kg. The board is fitted with casters for portability and ease of use in experiments (Fig. 6.15).

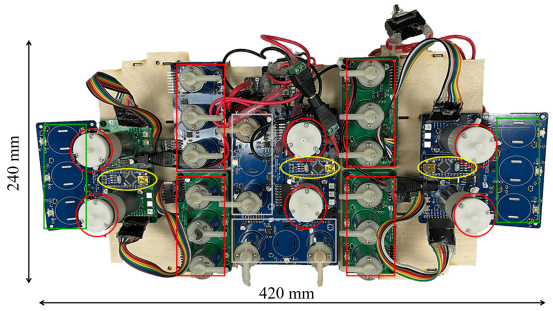


Figure 6.5: A top view of the novel pneumatic regulation board.

Compared to the only four air output channels that were actuated in our previous work [112], the pneumatic regulation board in this paper implements eight channels in total to introduce more motion capabilities for SoRX (specifically, body orientation and turning). Four additional channels are used to address the body orientation control and turning (to be elaborated in Section 6.4).

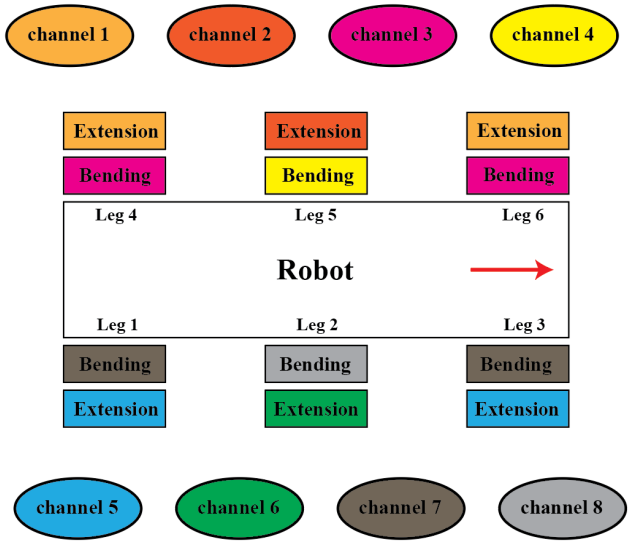


Figure 6.6: A diagram of 8 air output channels to drive 12 actuation parts (6 extension parts and 6 bending parts). Actuation parts and air ouput channels in the same color are connected, i.e channel 1 is connected to extension parts of leg 4 and leg 6.

Figure 6.6 depicts the air flow logic for the pneumatic regulation in this work. There are in total eight air output channels (shown in different colors), and six legs each

comprising two actuated parts (extension and bending parts). The channels and actuation parts of same color are connected. By design, both extension and bending parts of the two outer legs on the same side are connected and operated with the same pressure input (that is, pairs {Leg 1 & Leg 3} and {Leg 4 & Leg 6}). The two parts of the middle legs (i.e. Leg 2 and Leg 5) are separately actuated with four additional channels.

### 6.3.2 Pressure Feedback Controller

In our pneumatic regulation board, pressurization and depressurization are attained by different pairs of pumps and valves. Because of this, there can be significant delays when transitioning between actuation modes. Existing feedback control methods (e.g., PID controllers) based on pressure values alone failed in our preliminary experimental tests, causing oscillations when the pressure is close to zero.

To mitigate this challenge, we propose herein a feedback controller to achieve relatively fast and precise pressure control and avoid oscillations [109]. In our design, desired trajectories of each air output channel consist of two values: `mode` and `desired`. We command the `mode` to be either `pressurize` or `depressurize`, and the `desired` to be desired pressure values (gauge) in the steady state. Two pumps and two valves contribute to the regulation of each air output channel. Let Valve and Pump be used for pressurization while the rest take charge during depressurization. Given total time $T$, threshold $\epsilon$;, the controller inputs the desired trajectories ($\text{mode}_t$, $\text{desired}_t$), pressure feedback values $\text{real}_t$ at time $t$, and outputs ON/OFF of values and pumps. It is important to note that the controller uses a threshold $\epsilon$ to avoid oscillations. Thresholds for each channels are empirically tuned.

The performance of the pressure feedback controller is evaluated by a step response test. In the experiment, a single extension part was actuated to track step trajectories with the proposed pressure feedback controller. The desired and measured air pressure values (gauge) are shown in Fig. 6.7. The grey boxes represent that the `mode` is `pressurize` while the white ones denote `depressurize`.

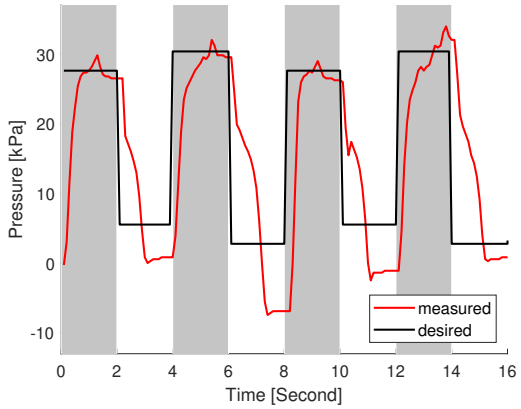


Figure 6.7: Step response for the proposed pressure feedback controller.

From the figure, the measured pressure in the steady state is generally tracking the positive desired one with small overshoot. However, when desired pressure is close to or smaller than zero, large tracking errors are observed in the steady state. Mismatches in negative pressure are caused because pressure decreases very fast when the volume of the air chamber is close to its minimum. However, based on Fig. 6.4, negative pressure values have little impact to the overall leg length. Hence, we consider that tracking errors, when desired pressure is close to or less than zero, have acceptable impact to the motion control of the robot.

## 6.4 Trajectory Tracking

### 6.4.1 Walking and Turning

This paper adopts the same actuation sequence as in [112] for walking (see Fig. 6.8a). Notations `E` and `B` represent extension bending parts, respectively. Red boxes are used to represent pressurization, while the green ones stand for depressurization. In the walking task, each tripod is actuated for half of the clock phase. During the actuation of each tripod, the extension parts are pressurized first and keep the pressure, followed by pressurization of the bending parts.

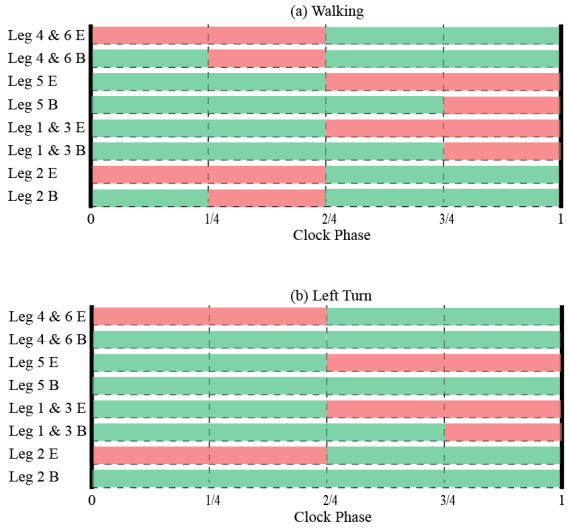


Figure 6.8: Actuation sequences for (a) walking and (b) left turn. (Figure best viewed in color.)

Compared to rigid robots, SoRX relies on leg's shape morphing to move, thus existing turning methods for hexapedal robots, such as in [170], were not successful in our preliminary experimental tests. To this end, we adopt in this work a simple yet effective turning method for the robot. Figure 6.8b shows a sample actuation sequence for making a left turn. Actuation sequences for the extension parts remain the same as in normal

walking, however, only the bending parts of two legs opposite to the turning direction are actuated. The difference in the actuation of bending parts within a tripod enables the robot to turn while the elongation of the extension parts of the other tripod assists legs to recover to upright configurations.

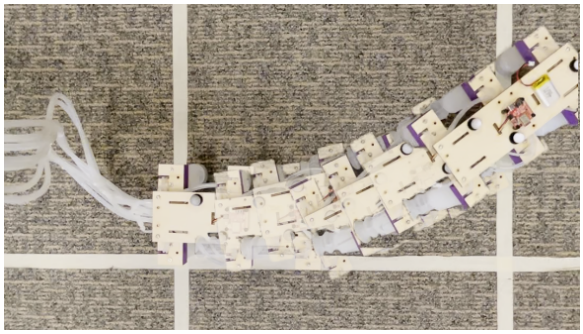

Figure 6.9: Composite images of a sample test on turning.

We test the performance of the proposed turning method with consecutive left turns. Figure 6.9 shows snapshots from a sample turning trajectory of the robot. Observations suggest that the bending part of leg 5 still curves passively due to the weight, however, actuation of two legs on the other side enables the robot to turn. A full actuation sequence enables the robot to turn by approximately 10°.

### 6.4.2 Closed-loop Trajectory Tracking

The significance of the developed turning method is that it enables implementation of *closed-loop trajectory tracking control* for the first time in the context of soft legged robots like SoRX. The approach we present herein is a direct and effective means that relies on trajectory corridors; investigation of tracking more involved trajectories in obstacle-cluttered environments is part of future work. Consider a desired trajectory containing 3D positions $(x, y, z)$ as shown in Fig. 6.10. Along with the desired trajectory, we prescribe

a 2D corridor (black dashed lines), which is defined to lie at a fixed, user-defined distance from the desired trajectory's projection on the x-y plane.

The robot receives location data from motion capture at 100 Hz and compares the 2D position (the geometric center of the planar body) with the boundaries of the corridor at a rate of 10 Hz. When the center is located outside the boundaries, the robot will trigger the turning method to move toward the desired trajectory, until the center is found across the desired trajectory. For instance, Fig. 6.10 is sketched to show the center (point $o$) being outside the right boundary, thus the turning method drives the robot to turn left. Given the current location (point $o$) from the motion capture system, we map it to the desired trajectory (point $o'$). In this work, point $o'$ is found using the same $y$ values for simplicity, however, the minimal distance can be used for mapping complex trajectories. The height of the mapped point $z(o')$ is used as the desired height of the robot at the current location. The desired air pressure is calculated based on models in Table 6.3, and sent to the pressure feedback controller.

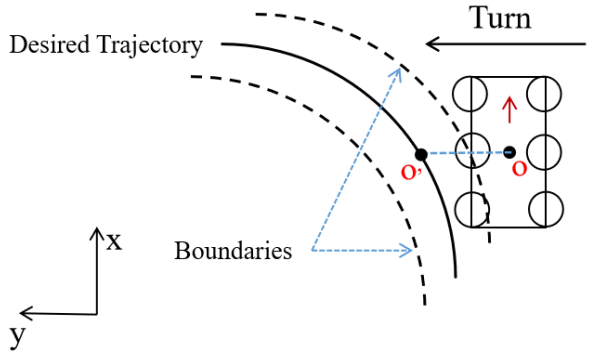


Figure 6.10: Illustration of the closed-loop trajectory tracker.

Table 6.3: Key Parameters and their Values

| $L_B$ | $W_B$ | $L_0$ | $\epsilon_B$ | $\epsilon_E$ |
|---|---|---|---|---|
| 230 mm | 140 mm | 65 mm | 10 kPa | 5 kPa |

## 6.5 Experimental Results

We conduct both indoor and outdoor experiments to test the proposed model-based position control and closed-loop trajectory tracking on the SoRX robot [112]. For indoor tests, the position of the robot is captured using a 12-camera Optitrack motion capture system. A desktop (Intel NUC 10 with 2.3 GHZ i7 CPU) is used as the companion computer for indoor tests while an Odroid XU4 takes charge for outdoor ones. The robot operates on the flat ground for all indoor tests. Values for key parameters used in the paper are listed in Table 6.3. Note that $\epsilon_B$ and $\epsilon_E$ are the thresholds for bending and extension parts used in the pressure controller, respectively.

### 6.5.1 Position Control

Two experiments are conducted to evaluate the proposed static models in Section 6.2.2. In the first test, the robot is placed on the ground, and one tripod is controlled to change the height of the center (point $o$). The largest desired height of 132 mm is achieved when all extensions parts are pressurized while the lowest desired height of 120 mm corresponds to the state of depressurization of the tripod.

Desired pressure values are determined based on (6.1) and the polynomials models in Table 6.3. It is important to note that legs for both two sides of the tripod have the same length by design. Based on the fitting models, we calculate the pressure values 19.75 and $-8.11$ kPa for the extension parts on double-leg tripod side, while 16.93 and 2.26 kPa for

the single-leg side. We input the desired pressure values to the pressure feedback controller with a time interval of 2 sec and record the height from the motion capture system.

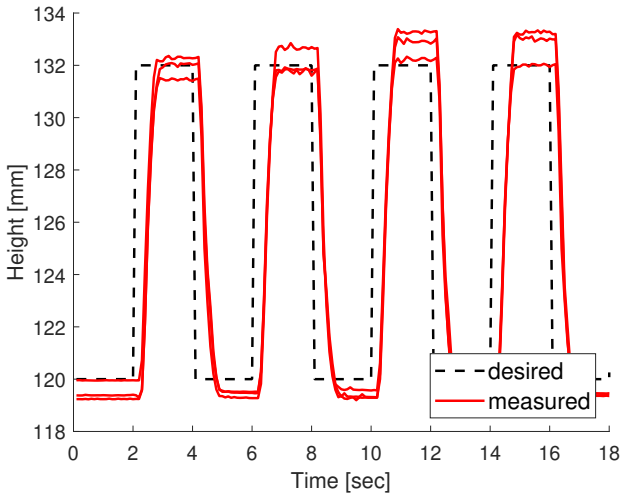


Figure 6.11: Desired and measured values for the height of the robot's center (point $o$).

Figure 6.11 presents both desired and measured height of the robot's center for three consecutive experimental trials. Although delays and relatively small steady errors are observed, results suggest the height of the center is tracking the desired trajectories with the proposed methods. Similarly, we apply the same desired pressure inputs to evaluate (6.2). Given the difference between two extreme heights ($L_5 - L_1 = 12$ mm), we can calculate the roll angle $\phi = \arctan\left(2(L_5 - L_1)/W_B\right) = 0.17$ rad. Three consecutive tests are conducted and results are shown in Fig. 6.12. The measured roll angles are in general tracking the desired ones despite delays and steady errors introduced by the pressure controller and model fitting.

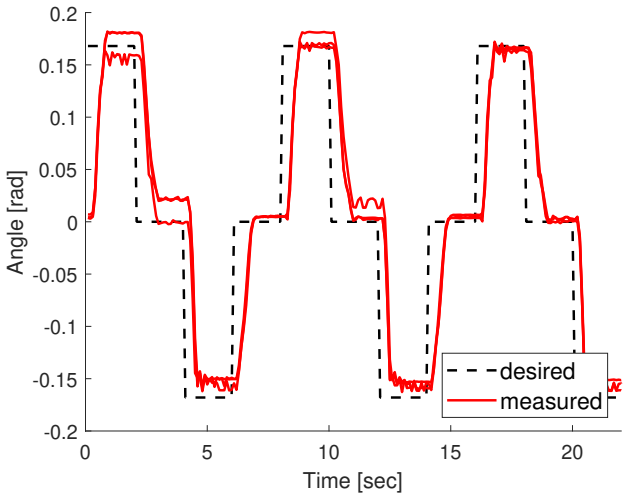


Figure 6.12: Desired and measured the roll angle $\phi$ for the robot's planar body.

### 6.5.2 Trajectory Tracking

We conduct three experiments to validate the closed-loop trajectory tracking method. In the first test, only the 2D position of the robot is considered. We command the robot to track two planar trajectories: 1) a straight line and 2) a quarter circle.

In the straight line case, the robot starts at the origin and is expected to reach the point $(0, 1.5)$ m, and the robot stops after reaching the line of $y = 1.5$ m. The boundaries are set at $x = \pm 0.05$ m. Three consecutive experimental trials are made with different starting angles $(0, \pm 15°)$. The desired and measured trajectories for all trials are shown in Fig. 6.13, where the blue and green dots denote components of the robot trajectory during which the tracker sends right and left turning commands, respectively. Results show that the robot walks generally in straight line without steering control with a zero starting angle, until reaching a distance of 1.2 m followed by right turns. Further, the effectiveness of the method is validated with $\pm 15°$ starting angles. Results shows that the robot walks outside the boundaries shortly after the start, however, the trajectory tracking method drives the

robot to move toward the desired trajectory with repeating changes of right/left turning sequences.

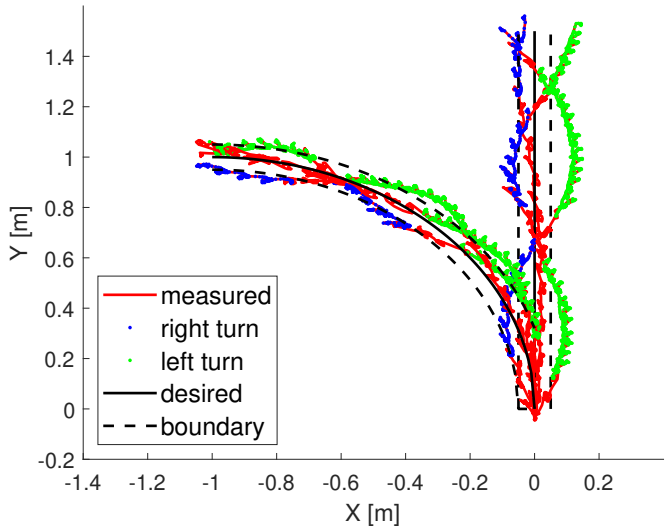


Figure 6.13: Results for closed-loop 2D trajectories tracking experiments.

Moreover, a desired trajectory of the quarter circle $(x+1)^2+y^2=1, x\in[-1,0]$ is set for the second experiment. Similarly, two boundaries $(x+1)^2+y^2=(1\pm0.05)^2$ are selected to trigger turning. The desired trajectory begins at the origin and moves toward the destination $(-1,1)$ m, where the robot stops after reaching the line $x=-1$ m. Three experimental trials are conducted with zero starting angles.

For the second experiment, we command the robot to track a variable-height trajectory. The trajectory consists of a planar straight line from the origin to the point $(0,1)$ m, and the desired maximal height jumps from 0.132 to 0.138 m after reaching the line $y=0.5$ m. Three consecutive tests are made with zero starting angles. The desired and measured trajectories of the robot are shown in Fig. 6.14. Given the two steady states for the walking task, oscillations for the height of the robot's center are observed along the

trajectories. However, results indicate the utility of our method to track variable-height trajectories since the maximal heights of the robot's center display a jump after passing the line $y = 0.5$ m, as desired.

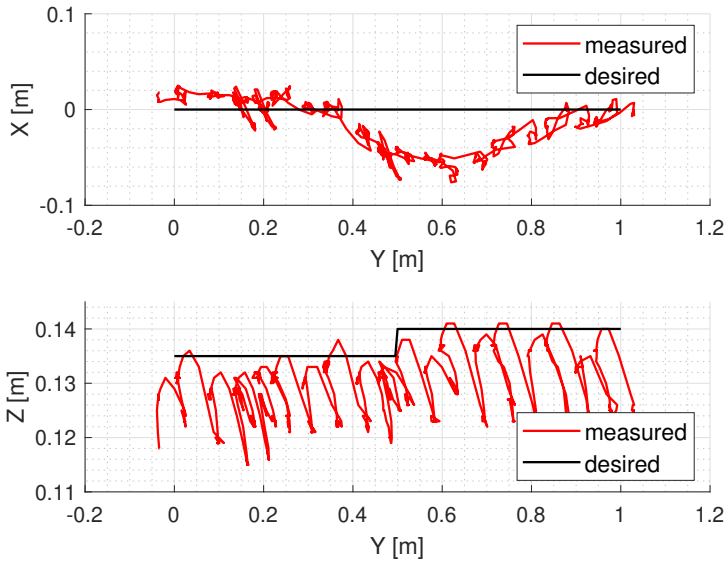


Figure 6.14: Desired and measured positions for tracking a variable-height trajectory.

### 6.5.3 Tracking Performance

We list all the tracking errors in Table 6.4. Note that we use the distance of the measured positions to the desired trajectories for both line and curve tracking experiments. For instance, $d_1$ denotes the absolute value of the measured $x$ for the straight line tracking test. For the variable-height trajectory tracking test, only the errors for the height $h$ are considered. Given the height oscillations during the walking, a relatively large tracking error is observed for the variable-height experiment, since all values are compared with the desired maximal heights.

Table 6.4: Tracking Performance

| **Variables** | **Tracking Errors** | **Units** |
|---|---|---|
| Step Response $p$ | $-0.737 \pm 11.198$ | kPa |
| Height $h$ | $-0.263 \pm 4.910$ | mm |
| Angle $\phi$ | $0.006 \pm 0.073$ | rad |
| Line $d_1$ | $0.029 \pm 0.019$ | m |
| Curve $d_2$ | $0.045 \pm 0.020$ | m |
| Variable-Height $h$ | $-6.988 \pm 5.557$ | mm |

### 6.5.4 Outdoor Field Testing

Taking advantage of the compact and mobile design of the novel pneumatic regulation board, we can deploy SoRX in outdoor environments. Figure 6.15 shows a snapshot from field testing with the robot. An Odroid XU4 coordinates with the board and a joystick controls the walking and steering of the robot. Powered by the untethered board, SoRX operates on various types of natural rough terrains, including creeks and gravels (see Fig. 6.1).

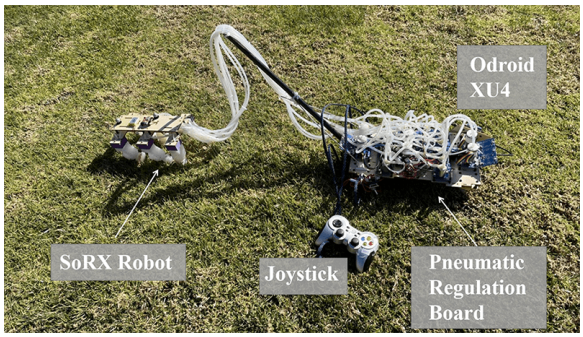


Figure 6.15: SoRX is able to operate in outdoor environments powered by the untethered pneumatic regulation board.

## 6.6 Conclusions

This chapter contributes to extending the motion capabilities of a soft pneumatic legged robot SoRX, which has shown able to traverse rough, steep and unstable terrain. We propose a static model based on geometric constraints for feedforward position control. With an aim to deploy the robot in outdoor environments, we design and implement a novel compact and mobile pneumatic regular board that powers up to 8 channels of pressurization/depressurization with pressure feedback. The chapter also proposes a pressure feedback controller, as well as a closed-loop variable-height trajectories tracking method, that utilize the pneumatic regulation board to enable the robot track trajectories. In the next chapter, we summarize the contributions of this dissertation.

# Chapter 7

# Summary

We conclude this dissertation by providing a brief overview of the contributions made in each chapter of this study, along with highlighting potential avenues for future research or further investigations.

## 7.1 Summary of Contributions of this Work

Compliant autonomous robots engaged in physical interactions have gained significant attention from both academia and industry in the past few years. These physical interactions encompass the application of instantaneous or constant external forces on the robots, creating challenges for their stability and navigation. By considering the collective contributions, we have conducted a comprehensive study on these compliant autonomous robots operating in physical interaction scenarios. The dissertation studies aerial and legged robotic platforms with the added compliance and physical interactions with environments or other robots. Three approaches are taken in studying the compliant robotic platforms

with interactions: 1) effects of the added compliance, 2) dynamic modeling of compliant autonomy and 3) interaction-inclusive motion planning. The contributions of this work may provide the foundations of a general framework for modeling, control and planning of compliant robots under physical interactions. Specifically, the **Focus 1** can find applications such as a robust experimental platform for collision-tolerant navigation in GNSS-denied clutter environments [133], extending MAVs motion planning for aggressive flight [108] and impact-resilient motion planning for heterogeneous robot teams [38]. **Focuse 2** presents an innovative technique for securely capturing an aerial micro-robot while it is in mid-air using another aerial robot equipped with a versatile soft gripper. The solution can find applications to recover malfunctioning aerial robots and intercept and contain unidentified flying targets [146]. Furthermore, **Focuse 3** offers a template in design, modeling, control, and trajectory tracking of a soft legged robot to traverse challenging terrains. Our work presents encouraging and repeatable results to motivate research on autonomous soft legged robots in outdoor environments.

- In Chapter 2, our starting point is the design of an innovative quadrotor that actively incorporates passive springs into its arms. This design feature aims to minimize the impact and enhance the quadrotor's ability to withstand collisions. To quickly detect contact and assess changes in compliance resulting from impacts, we have devised a method that combines readings from Hall effect sensors. Furthermore, we have introduced dynamics modeling for both compliant arms and contact, utilizing the KV and HC models. By leveraging the compliant structure of the quadrotor and employing a geometric tracking controller, we propose an effective recovery approach

that generates and maintains a target position following a collision. Our experimental results provide evidence of the quadrotor's impressive resilience against high-speed and large-angle collisions with vertical walls.

- In Chapter 3, we introduce the design and dynamic modeling of an aerial robot that is specifically engineered to withstand impacts. This robot incorporates a compliant arm, which serves the dual purpose of detecting contacts and minimizing collision impact. To accurately gauge the real-time contact force in the presence of compliance, we propose an estimator. By leveraging this impact-reducing mechanism and the contact force estimator, we significantly enhance the robot's ability to handle high-speed collisions with walls and poles. Additionally, we utilize the robust collision resilience capability of the robot to develop a novel planning method that prioritizes contacts. To evaluate the effectiveness of our planning method in partially-known cluttered environments, we conduct extensive simulations and physical tests, comparing it to other collision-avoidance planning approaches commonly used in similar scenarios.

- In Chapter 4, we propose a novel technique to securely capture an aerial micro-robot while it is in mid-air, utilizing another aerial robot equipped with a versatile soft gripper. The design of the gripper incorporates soft actuators, allowing it to maintain a horizontal orientation and flex appropriately when exposed to air pressure. Additionally, our research introduces a planning method that utilizes piecewise polynomial optimization to guarantee a safe capture of flying micro-robots while avoiding destabilizing the target. We present experimental results that validate the effectiveness of capturing both stationary and moving aerial targets. Furthermore, we conduct a com-

parative analysis of the free flight performance between our robot and a conventional quadrotor under various gripper and payload conditions.

- In Chapter 5, we present a soft legged robot that possess the unique capability to compress and flex, granting them the ability to navigate through obstacles and traverse narrow areas. In this study, we introduce an innovative soft hexapedal robot, named SoRX. This robot incorporates a cutting-edge design feature: 2-DoF soft pneumatic actuators that offer both bending and extension capabilities. These actuators enable the generation of foot trajectory profiles that are well-suited for legged locomotion. We propose an alternating tripod gait for the robot, and through experimentation, we demonstrate its exceptional effectiveness in facilitating locomotion across diverse terrains, including flat surfaces, rough terrains, steep inclines, and unstable ground.

- In Chapter 6, we enhance the motion capabilities of our soft pneumatic legged robot. Firstly, we present a static model that enables feedforward position control, specifically for regulating the body height and orientation of SoRX. This control mechanism is crucial for deploying the robot effectively in outdoor environments. To achieve fast and precise control, we propose the utilization of an air pressure feedback controller, which is implemented through a custom low-cost pneumatic regulation board. This controller ensures efficient regulation of the robot's pneumatic system. Additionally, we introduce a closed-loop trajectory tracking method, enabling the robot to accurately follow variable-height trajectories. These advancements aim to enhance the overall performance and versatility of SoRX in a variety of real-world scenarios.

## 7.2 Future Research Directions

The work here motivates several future research direction for each aspect that is considered. In **Focus 1**, we assumed regular wall and pole obstacles; we plan to extend results to irregular obstacles in 3D space. While collision handling involves basic motion control, it is possible to study force-control-based recovery methods on the compliant robot such as impedance and admittance control [205]. Further, we plan to incorporate camera or laser distance sensors for odometry feedback and deploy impact-resilient aerial robots in outdoor environments such as subterranean maps [135]. Lastly, we plan to study collision-inclusive high-speed flight drone racing [59] is also another direction of future research.

Furthermore, in **Focus 2**, the flying target's weight in current stage is very small. We plan to upgrade the MAV hardware and incorporate the target's mass onto the system's modeling as in [128], as well as robust or adaptive controlling methods to address changes in mass and inertia.While the aerial vehicle has a maximum payload of 1.2 kg, the proposed soft gripper can only grasp objects with masses up to 280 g. To scale up the solution, we plan to strengthen the grasping capacity by using stronger materials and pneumatic actuation. Third, it is of interest to incorporate feedback control of the soft end-effector as in [138]. Lastly, **Focus 3** includes future work such as implementation of more involved trajectory trackers while considering interactions with the environment, and incorporation of sensors for autonomous navigation and applications to precision agriculture.

# Bibliography


[1] M Ahmad, Ismail Khairul Azwan, and F Mat. Impact models and coefficient of restitution: a review. *ARPN Journal of Engineering and Applied Sciences*, 2016.

[2] Omar M Al-Jarrah and Yuan F Zheng. Arm-manipulator coordination for load sharing using compliant control. In *IEEE International Conference on Robotics and Automation (ICRA)*, volume 2, pages 1000–1005. IEEE, 1996.

[3] Albert Albers, Simon Trautmann, Thomas Howard, Trong Anh Nguyen, Markus Frietsch, and Christian Sauter. Semi-autonomous flying robot for physical interaction with environment. In *IEEE Conference on Robotics, Automation and Mechatronics*, pages 441–446, 2010.

[4] Jérémie Allard, Stéphane Cotin, François Faure, Pierre-Jean Bensoussan, François Poyer, Christian Duriez, Hervé Delingette, and Laurent Grisoni. Sofa-an open source framework for medical simulation. In *Medicine Meets Virtual Reality(MMVR)*, volume 125, pages 13–18, 2007.

[5] Richard Altendorfer, Ned Moore, Haldun Komsuoglu, Martin Buehler, HB Brown, Dave McMordie, Uluc Saranli, Robert Full, and Daniel E Koditschek. Rhex: A biologically inspired hexapod runner. *Autonomous Robots*, 11(3):207–213, 2001.

[6] Taylor Apgar, Patrick Clary, Kevon Green, Alan Fern, and Jonathan W. Hurst. Fast online trajectory optimization for the bipedal robot cassie. In *Robotics: Science and Systems (RSS)*, 2018.

[7] Aurel X Appius, Erik Bauer, Marc Blöchlinger, Aashi Kalra, Robin Oberson, Arman Raayatsanati, Pascal Strauch, Sarath Suresh, Marco von Salis, and Robert K Katzschmann. Raptor: Rapid aerial pickup and transport of objects by robots. In *IEEE/RSJ International Conference on Intelligent Robots and Systems (IROS)*, pages 349–355, 2022.

[8] Barbara Arbanas, Antun Ivanovic, Marko Car, Tomislav Haus, Matko Orsag, Tamara Petrovic, and Stjepan Bogdan. Aerial-ground robotic system for autonomous delivery tasks. In *IEEE International Conference on Robotics and Automation (ICRA)*, pages 5463–5468, 2016.

[9] Federico Augugliaro and Raffaello D'Andrea. Admittance control for physical human-quadrocopter interaction. In *European Control Conference (ECC)*, pages 1805–1810. IEEE, 2013.

[10] Frederico Augugliaro, Sergei Lupashin, Michael Hamer, Cason Male, Markus Hehn, Mark W Mueller, Jan Sebastian Willmann, Fabio Gramazio, Matthias Kohler, and Raffaello D'Andrea. The flight assembled architecture installation: Cooperative construction with flying machines. *IEEE Control Systems Magazine*, 34(4):46–64, 2014.

[11] Khelifa Baizid, Gerardo Giglio, Francesco Pierri, Miguel Angel Trujillo, Gianluca Antonelli, Fabrizio Caccavale, Antidio Viguria, Stefano Chiaverini, and Aníbal Ollero. Experiments on behavioral coordinated control of an unmanned aerial vehicle manipulator system. In *IEEE International Conference on Robotics and Automation (ICRA)*, pages 4680–4685, 2015.

[12] T Bartelds, Alex Capra, Salua Hamaza, Stefano Stramigioli, and Matteo Fumagalli. Compliant aerial manipulators: Toward a new generation of aerial robotic workers. *IEEE Robotics and Automation Letters*, 1(1):477–483, 2016.

[13] Manuel Bejar, Anibal Ollero, and Konstantin Kondak. Helicopter based aerial manipulators. In *Aerial Robotic Manipulation*, pages 35–52. Springer, 2019.

[14] Steven Bellens, Joris De Schutter, and Herman Bruyninckx. A hybrid pose/wrench control framework for quadrotor helicopters. In *IEEE International Conference on Robotics and Automation (ICRA)*, pages 2269–2274, 2012.

[15] James M. Bern, P. Banzet, Roi Poranne, and Stelian Coros. Trajectory optimization for cable-driven soft robot locomotion. In *Robotics: Science and Systems (RSS)*, 2019.

[16] Charles M Best, Morgan T Gillespie, Phillip Hyatt, Levi Rupert, Vallan Sherrod, and Marc D Killpack. A new soft robot control method: Using model predictive control for a pneumatically actuated humanoid. *IEEE Robotics & Automation Magazine*, 23(3):75–84, 2016.

[17] Thor Morales Bieze, Frederick Largilliere, Alexandre Kruszewski, Zhongkai Zhang, Rochdi Merzouki, and Christian Duriez. Finite element method-based kinematics and closed-loop control of soft, continuum manipulators. *Soft robotics*, 5(3):348–364, 2018.

[18] Paul Birkmeyer, Kevin Peterson, and Ronald S Fearing. Dash: A dynamic 16g hexapedal robot. In *IEEE/RSJ International Conference on Intelligent Robots and Systems (IROS)*, pages 2683–2689, 2009.

[19] Dario Brescianini, Markus Hehn, and Raffaello D'Andrea. Nonlinear quadrocopter attitude control: Technical report. Technical report, ETH Zurich, 2013.

[20] Adrien Briod, Przemyslaw Kornatowski, Adam Klaptocz, Arnaud Garnier, Marco Pagnamenta, Jean-Christophe Zufferey, and Dario Floreano. Contact-based navigation for an autonomous flying robot. In *IEEE/RSJ International Conference on Intelligent Robots and Systems (IROS)*, pages 3987–3992, 2013.

[21] Andrea Calanca, Riccardo Muradore, and Paolo Fiorini. A review of algorithms for compliant control of stiff and fixed-compliance robots. *IEEE/ASME transactions on mechatronics*, 21(2):613–624, 2015.

[22] David B Camarillo, Christopher F Milne, Christopher R Carlson, Michael R Zinn, and J Kenneth Salisbury. Mechanics modeling of tendon-driven continuum manipulators. *IEEE transactions on robotics*, 24(6):1262–1273, 2008.

[23] P. Castillo, R. Lozano, and A. Dzul. Stabilization of a mini rotorcraft with four rotors. *IEEE Control Systems*, 25(6):45–55, 2005.

[24] Guangsheng Chen, Jian Zhou, Lin Wang, Yu Wang, Yong Yin, and Zhongjun Ding. Modeling and adaptive controlling of quadrotor uav with flexible gripper. In *IEEE Joint International Information Technology and Artificial Intelligence Conference (ITAIC)*, volume 10, pages 1984–1991, 2022.

[25] Tony G Chen, Kenneth AW Hoffmann, Jun En Low, Keiko Nagami, David Lentink, and Mark R Cutkosky. Aerial grasping and the velocity sufficiency region. *IEEE Robotics and Automation Letters*, 7(4):10009–10016, 2022.

[26] YuFeng Chen, Siyi Xu, Zhijian Ren, and Pakpong Chirarattananon. Collision resilient insect-scale soft-actuated aerial robots with high agility. *IEEE Transactions on Robotics*, 37(5):1752–1764, 2021.

[27] Nicholas Cherouvim and Evangelos Papadopoulos. Control of hopping speed and height over unknown rough terrain using a single actuator. In *IEEE International Conference on Robotics and Automation (ICRA)*, pages 2743–2748, 2009.

[28] Stefano Chiaverini, Bruno Siciliano, and Olav Egeland. Review of the damped least-squares inverse kinematics with experiments on an industrial robot manipulator. *IEEE Transactions on control systems technology*, 2(2):123–134, 1994.

[29] Fiona Chui, Gareth Dicker, and Inna Sharf. Dynamics of a quadrotor undergoing impact with a wall. In *IEEE International Conference on Unmanned Aircraft Systems (ICUAS)*, pages 717–726, 2016.

[30] Eulalie Coevoet, Adrien Escande, and Christian Duriez. Optimization-based inverse model of soft robots with contact handling. *IEEE Robotics and Automation Letters*, 2(3):1413–1419, 2017.

[31] Eulalie Coevoet, Adrien Escande, and Christian Duriez. Soft robots locomotion and manipulation control using fem simulation and quadratic programming. In *IEEE International Conference on Soft Robotics (RoboSoft)*, pages 739–745, 2019.

[32] Eulalie Coevoet, Thor Morales-Bieze, Frederick Largilliere, Zhongkai Zhang, Maxime Thieffry, Mario Sanz-Lopez, Bruno Carrez, Damien Marchal, Olivier Goury, Jeremie Dequidt, et al. Software toolkit for modeling, simulation, and control of soft robots. *Advanced Robotics*, 31(22):1208–1224, 2017.

[33] Todd W Danko, Kenneth P Chaney, and Paul Y Oh. A parallel manipulator for mobile manipulating uavs. In *IEEE International Conference on Technologies for Practical Robot Applications (TePRA)*, pages 1–6, 2015.

[34] Todd W Danko and Paul Y Oh. A hyper-redundant manipulator for mobile manipulating unmanned aerial vehicles. In *IEEE International Conference on Unmanned Aircraft Systems (ICUAS)*, pages 974–981, 2013.

[35] Paolo De Petris, Stephen J Carlson, Christos Papachristos, and Kostas Alexis. Collision-tolerant aerial robots: A survey. *arXiv preprint arXiv:2212.03196*, 2022.

[36] Paolo De Petris, Mihir Kulkarni, Huan Nguyen, and Kostas Alexis. Risk-aware motion planning for collision-tolerant aerial robots subject to localization uncertaint. In *IEEE/RSJ International Conference on Intelligent Robots and Systems (IROS)*, pages 4561–4568, 2022.

[37] Paolo De Petris, Huan Nguyen, Mihir Kulkarni, Frank Mascarich, and Kostas Alexis. Resilient collision-tolerant navigation in confined environments. In *IEEE International Conference on Robotics and Automation (ICRA)*, pages 2286–2292, 2021.

[38] Mark Debord, Wolfgang Hönig, and Nora Ayanian. Trajectory planning for heterogeneous robot teams. In *IEEE/RSJ International Conference on Intelligent Robots and Systems (IROS)*, pages 7924–7931, 2018.

[39] Cosimo Della Santina, Robert K Katzschmann, Antonio Bicchi, and Daniela Rus. Model-based dynamic feedback control of a planar soft robot: trajectory tracking and interaction with the environment. *The International Journal of Robotics Research*, 39(4):490–513, 2020.

[40] Gareth Dicker, Fiona Chui, and Inna Sharf. Quadrotor collision characterization and recovery control. In *IEEE International Conference on Robotics and Automation (ICRA)*, pages 5830–5836, 2017.

[41] Gareth Dicker, Inna Sharf, and Pulkit Rustagi. Recovery control for quadrotor uav colliding with a pole. In *IEEE/RSJ International Conference on Intelligent Robots and Systems*, pages 6247–6254, 2018.

[42] Krishna Manaswi Digumarti, Andrew T Conn, and Jonathan Rossiter. Euglenoid-inspired giant shape change for highly deformable soft robots. *IEEE Robotics and Automation Letters*, 2(4):2302–2307, 2017.

[43] DroGone. Drogone autonomous counter drone systems [online] available at: `https://www.drogone.com/`. 2022. [Accessed 14 Sep. 2022].

[44] DroneCatcher. Dronecatcher a delft dynamics product [online] available at: `https://dronecatcher.nl/`. 2022. [Accessed 14 Sep. 2022].

[45] Dylan Drotman, Michael Ishida, Saurabh Jadhav, and Michael T Tolley. Application-driven design of soft, 3-d printed, pneumatic actuators with bellows. *IEEE/ASME Transactions on Mechatronics*, 24(1):78–87, 2018.

[46] Dylan Drotman, Saurabh Jadhav, Mahmood Karimi, Philip Dezonia, and Michael T Tolley. 3d printed soft actuators for a legged robot capable of navigating unstructured terrain. In *IEEE International Conference on Robotics and Automation (ICRA)*, pages 5532–5538, 2017.

[47] Dylan Drotman, Saurabh Jadhav, David Sharp, Christian Chan, and Michael T Tolley. Electronics-free pneumatic circuits for controlling soft-legged robots. *Science Robotics*, 6(51), 2021.

[48] Pierre E Dupont, Jesse Lock, Brandon Itkowitz, and Evan Butler. Design and control of concentric-tube robots. *IEEE Transactions on Robotics*, 26(2):209–225, 2009.

[49] Christian Duriez. Control of elastic soft robots based on real-time finite element method. In *IEEE International Conference on Robotics and Automation (ICRA)*, pages 3982–3987, 2013.

[50] Christian Duriez, Eulalie Coevoet, Frédérick Largilliere, T Morales-Bieze, Zhongkai Zhang, Mario Sanz-Lopez, Bruno Carrez, Damien Marchal, Olivier Goury, and Jérémie Dequidt. Framework for online simulation of soft robots with optimization-based inverse model. In *IEEE International Conference on Simulation, Modeling, and Programming for Autonomous Robots (SIMPAR)*, pages 111–118, 2016.

[51] Diego S D'Antonio and David Saldaña. Folding knots using a team of aerial robots. In *IEEE/RSJ International Conference on Intelligent Robots and Systems (IROS)*, pages 3372–3377. IEEE, 2022.

[52] Alexander Enoch, Andrius Sutas, Shin'ichiro Nakaoka, and Sethu Vijayakumar. Blue: A bipedal robot with variable stiffness and damping. In *IEEE-RAS International Conference on Humanoid Robots (Humanoids)*, pages 487–494, 2012.

[53] Davide Falanga, Elias Mueggler, Matthias Faessler, and Davide Scaramuzza. Aggressive quadrotor flight through narrow gaps with onboard sensing and computing using active vision. In *IEEE International Conference on Robotics and Automation (ICRA)*, pages 5774–5781, 2017.

[54] Dadong Fan, Kexin Guo, Shangke Lyu, Xiang Yu, Lihua Xie, and Lei Guo. Quadrotor uav: Collision resilience behaviors. *IEEE Transactions on Aerospace and Electronic Systems*, 2022.

[55] Aleksey Fedoseev, Valerii Serpiva, Ekaterina Karmanova, Miguel Altamirano Cabrera, Vladimir Shirokun, Iakov Vasilev, Stanislav Savushkin, and Dzmitry Tsetserukou. Dronetrap: Drone catching in midair by soft robotic hand with color-based force detection and hand gesture recognition. In *IEEE International Conference on Soft Robotics (RoboSoft)*, pages 261–266, 2021.

[56] Usman A Fiaz, Mohamed Abdelkader, and Jeff S Shamma. An intelligent gripper design for autonomous aerial transport with passive magnetic grasping and dual-impulsive release. In *IEEE/ASME International Conference on Advanced Intelligent Mechatronics (AIM)*, pages 1027–1032, 2018.

[57] Joshua Fishman, Samuel Ubellacker, Nathan Hughes, and Luca Carlone. Dynamic grasping with a" soft" drone: From theory to practice. In *IEEE/RSJ International Conference on Intelligent Robots and Systems (IROS)*, pages 4214–4221, 2021.

[58] Juan Manuel Florez, Benjamin Shih, Yixin Bai, and Jamie K Paik. Soft pneumatic actuators for legged locomotion. In *IEEE International Conference on Robotics and Biomimetics (ROBIO)*, pages 27–34, 2014.

[59] Philipp Foehn, Dario Brescianini, Elia Kaufmann, Titus Cieslewski, Mathias Gehrig, Manasi Muglikar, and Davide Scaramuzza. Alphapilot: Autonomous drone racing. *Autonomous Robots*, 46(1):307–320, 2022.

[60] Philipp Foehn and Davide Scaramuzza. Onboard state dependent lqr for agile quadrotors. In *IEEE International Conference on Robotics and Automation (ICRA)*, pages 6566–6572, 2018.

[61] Matteo Fumagalli, Roberto Naldi, Alessandro Macchelli, Francesco Forte, Arvid QL Keemink, Stefano Stramigioli, Raffaella Carloni, and Lorenzo Marconi. Developing an aerial manipulator prototype: Physical interaction with the environment. *IEEE Robotics & Automation Magazine*, 21(3):41–50, 2014.

[62] Bruno Gabrich, David Saldana, Vijay Kumar, and Mark Yim. A flying gripper based on cuboid modular robots. In *IEEE International Conference on Robotics and Automation (ICRA)*, pages 7024–7030, 2018.

[63] Kevin C Galloway, Jonathan E Clark, and Daniel E Koditschek. Design of a tunable stiffness composite leg for dynamic locomotion. In *ASME International Design Engineering Technical Conferences and Computers and Information in Engineering Conference (IDETC/CIE)*, pages 215–222, 2009.

[64] Gowtham Garimella and Marin Kobilarov. Towards model-predictive control for aerial pick-and-place. In *IEEE International Conference on Robotics and Automation (ICRA)*, pages 4692–4697, 2015.

[65] Vaibhav Ghadiok, Jeremy Goldin, and Wei Ren. Autonomous indoor aerial gripping using a quadrotor. In *IEEE/RSJ International Conference on Intelligent Robots and Systems*, pages 4645–4651, 2011.

[66] Gianni Gilardi and Inna Sharf. Literature survey of contact dynamics modelling. *Mechanism and machine theory*, 37(10):1213–1239, 2002.

[67] Jesús M Gómez-de Gabriel, Juan M Gandarias, Francisco J Pérez-Maldonado, Francisco J García-Núñcz, Emilio J Fernández-García, and Alfonso J García-Cerezo. Methods for autonomous wristband placement with a search-and-rescue aerial manipulator. In *IEEE/RSJ International Conference on Intelligent Robots and Systems (IROS)*, pages 7838–7844, 2018.

[68] Juan Angel Gonzalez-Aguirre, Ricardo Osorio-Oliveros, Karen L Rodríguez-Hernández, Javier Lizárraga-Iturralde, Rubén Morales Menendez, Ricardo A Ramírez-Mendoza, Mauricio Adolfo Ramírez-Moreno, and Jorge de Jesús Lozoya-Santos. Service robots: Trends and technology. *Applied Sciences*, 11(22):10702, 2021.

[69] Yong Guo, Rongjie Kang, Lisha Chen, and Jian Dai. Dynamic modeling for a continuum robot with compliant structure. In *ASME 2015 International Design Engineering Technical Conferences and Computers and Information in Engineering Conference*. American Society of Mechanical Engineers Digital Collection, 2015.

[70] Salua Hamaza, Ioannis Georgilas, and Thomas Richardson. An adaptive-compliance manipulator for contact-based aerial applications. In *IEEE/ASME International Conference on Advanced Intelligent Mechatronics (AIM)*, pages 730–735, 2018.

[71] Samira Hayat, Evşen Yanmaz, Timothy X. Brown, and Christian Bettstetter. Multi-objective UAV path planning for search and rescue. In *IEEE International Conference on Robotics and Automation*, pages 5569–5574, 2017.

[72] Markus Hehn and Raffaello D'Andrea. Quadrocopter trajectory generation and control. *IFAC proceedings Volumes*, 44(1):1485–1491, 2011.

[73] Donal Holland, Evelyn J Park, Panagiotis Polygerinos, Gareth J. Bennett, and Conor J Walsh. The soft robotics toolkit: Shared resources for research and design. *Soft Robotics*, 1(3):224–230, 2014.

[74] Dónal P Holland, Evelyn J Park, Panagiotis Polygerinos, Gareth J Bennett, and Conor J Walsh. The soft robotics toolkit: Shared resources for research and design. *Soft Robotics*, 1(3):224–230, 2014.

[75] Kenneth H Hunt and Frank R Erskine Crossley. Coefficient of restitution interpreted as damping in vibroimpact. *ASME Journal of Applied Mechanics*, 1975.

[76] Jonathan W Hurst, Joel E Chestnutt, and Alfred A Rizzi. An actuator with physically variable stiffness for highly dynamic legged locomotion. In *IEEE International Conference on Robotics and Automation (ICRA)*, volume 5, pages 4662–4667, 2004.

[77] Jemin Hwangbo, Joonho Lee, Alexey Dosovitskiy, Dario Bellicoso, Vassilios Tsounis, Vladlen Koltun, and Marco Hutter. Learning agile and dynamic motor skills for legged robots. *Science Robotics*, 4(26), 2019.

[78] Antonio E Jimenez-Cano, Jesús Martin, Guillermo Heredia, Aníbal Ollero, and Raul Cano. Control of an aerial robot with multi-link arm for assembly tasks. In *IEEE International Conference on Robotics and Automation (ICRA)*, pages 4916–4921, 2013.

[79] Xinyue Kan, Hanzhe Teng, and Konstantinos Karydis. Online exploration and coverage planning in unknown obstacle-cluttered environments. *IEEE Robotics and Automation Letters*, 5(4):5969–5976, 2020.

[80] Xinyue Kan, Justin Thomas, Hanzhe Teng, Herbert G Tanner, Vijay Kumar, and Konstantinos Karydis. Analysis of ground effect for small-scale uavs in forward flight. *IEEE Robotics and Automation Letters*, 4(4):3860–3867, 2019.

[81] Sertac Karaman and Emilio Frazzoli. Sampling-based algorithms for optimal motion planning. *International Journal of Robotics Research*, 30(7):846–894, 2011.

[82] Konstantinos Karydis and M Ani Hsieh. Uncertainty quantification for small robots using principal orthogonal decomposition. In *International Symposium on Experimental Robotics*, pages 33–42. Springer, 2016.

[83] Konstantinos Karydis and Vijay Kumar. Energetics in robotic flight at small scales. *Interface focus*, 7(1):20160088, 2017.

[84] Konstantinos Karydis and Zhichao Liu. Soft pneumatic hexapedal robot, and uses thereof, June 23 2022. US Patent App. 17/560,075.

[85] Konstantinos Karydis, Ioannis Poulakakis, Jianxin Sun, and Herbert G Tanner. Probabilistically valid stochastic extensions of deterministic models for systems with uncertainty. *The International Journal of Robotics Research*, 34(10):1278–1295, 2015.

[86] Konstantinos Karydis, Ioannis Poulakakis, and Herbert G Tanner. A navigation and control strategy for miniature legged robots. *IEEE Transactions on Robotics*, 33(1):214–219, 2016.

[87] Konstantinos Karydis, Luis Valbuena, and Herbert G Tanner. Model predictive navigation for position and orientation control of nonholonomic vehicles. In *2012 IEEE International Conference on Robotics and Automation*, pages 3206–3211. IEEE, 2012.

[88] Konstantinos Karydis, David Zarrouk, Ioannis Poulakakis, Ronald S Fearing, and Herbert G Tanner. Planning with the star (s). In *2014 IEEE/RSJ International Conference on Intelligent Robots and Systems*, pages 3033–3038. IEEE, 2014.

[89] G. Kenneally, A. De, and D. E. Koditschek. Design principles for a family of direct-drive legged robots. *IEEE Robotics and Automation Letters*, 1(2):900–907, 2016.

[90] Nikhil Khedekar, Frank Mascarich, Christos Papachristos, Tung Dang, and Kostas Alexis. Contact–based navigation path planning for aerial robots. In *IEEE International Conference on Robotics and Automation*, pages 4161–4167, 2019.

[91] Suk-Jun Kim, Dae-Young Lee, Gwang-Pil Jung, and Kyu-Jin Cho. An origami-inspired, self-locking robotic arm that can be folded flat. *Science Robotics*, 3(16):eaar2915, 2018.

[92] Suseong Kim, Hoseong Seo, Seungwon Choi, and H Jin Kim. Vision-guided aerial manipulation using a multirotor with a robotic arm. *IEEE/ASME Transactions On Mechatronics*, 21(4):1912–1923, 2016.

[93] Adam Klaptocz, Adrien Briod, Ludovic Daler, Jean-Christophe Zufferey, and Dario Floreano. Euler spring collision protection for flying robots. In *IEEE/RSJ International Conference on Intelligent Robots and Systems (IROS)*, pages 1886–1892, 2013.

[94] Kristian Klausen, Thor I Fossen, and Tor Arne Johansen. Autonomous recovery of a fixed-wing uav using a net suspended by two multirotor uavs. *Journal of Field Robotics*, 35(5):717–731, 2018.

[95] Elena Kokkoni, Zhichao Liu, and Konstantinos Karydis. Development of a soft robotic wearable device to assist infant reaching. *Journal of Engineering and Science in Medical Diagnostics and Therapy*, 3(2), 2020.

[96] J Zico Kolter, Mike P Rodgers, and Andrew Y Ng. A control architecture for quadruped locomotion over rough terrain. In *IEEE International Conference on Robotics and Automation (ICRA)*, pages 811–818, 2008.

[97] Konstantin Kondak, Kai Krieger, Alin Albu-Schaeffer, Marc Schwarzbach, Maximilian Laiacker, Ivan Maza, Angel Rodriguez-Castano, and Anibal Ollero. Closed-loop behavior of an autonomous helicopter equipped with a robotic arm for aerial manipulation tasks. *International Journal of Advanced Robotic Systems*, 10(2):145, 2013.

[98] Christopher Korpela, Matko Orsag, and Paul Oh. Towards valve turning using a dual-arm aerial manipulator. In *IEEE/RSJ International Conference on Intelligent Robots and Systems (IROS)*, pages 3411–3416, 2014.

[99] Christopher Korpela, Matko Orsag, Miles Pekala, and Paul Oh. Dynamic stability of a mobile manipulating unmanned aerial vehicle. In *IEEE International Conference on Robotics and Automation (ICRA)*, pages 4922–4927, 2013.

[100] Nadia Kreciglowa, Konstantinos Karydis, and Vijay Kumar. Energy efficiency of trajectory generation methods for stop-and-go aerial robot navigation. In *IEEE International Conference on Unmanned Aircraft Systems (ICUAS)*, pages 656–662, 2017.

[101] Liam Kruse and Justin Bradley. A hybrid, actively compliant manipulator/gripper for aerial manipulation with a multicopter. In *IEEE International Symposium on Safety, Security, and Rescue Robotics (SSRR)*, pages 1–8, 2018.

[102] Benoit Landry, Robin Deits, Peter R Florence, and Russ Tedrake. Aggressive quadrotor flight through cluttered environments using mixed integer programming. In *IEEE International Conference on Robotics and Automation (ICRA)*, pages 1469–1475, 2016.

[103] Loong Yi Lee, Omar Ali Syadiqeen, Chee Pin Tan, and Surya G Nurzaman. Closed-structure compliant gripper with morphologically optimized multi-material fingertips for aerial grasping. *IEEE Robotics and Automation Letters*, 6(2):887–894, 2021.

[104] Taeyoung Lee, Melvin Leok, and N Harris McClamroch. Geometric tracking control of a quadrotor uav on se (3). In *IEEE Conference on Decision and Control (CDC)*, pages 5420–5425, 2010.

[105] Thomas Lew, Tomoki Emmei, David D Fan, Tara Bartlett, Angel Santamaria-Navarro, Rohan Thakker, and Ali-akbar Agha-mohammadi. Contact inertial odometry: collisions are your friends. In *The International Symposium of Robotics Research*, pages 938–958. Springer, 2019.

[106] Jiaoyang Li, Andrew Tinka, Scott Kiesel, Joseph W Durham, TK Satish Kumar, and Sven Koenig. Lifelong multi-agent path finding in large-scale warehouses. In *Proceedings of the AAAI Conference on Artificial Intelligence*, volume 35, pages 11272–11281, 2021.

[107] Maxim Likhachev, Geoffrey J Gordon, and Sebastian Thrun. Ara*: Anytime a* with provable bounds on sub-optimality. *Advances in Neural Information Processing Systems*, 16:767–774, 2003.

[108] Sikang Liu, Kartik Mohta, Nikolay Atanasov, and Vijay Kumar. Search-based motion planning for aggressive flight in se (3). *IEEE Robotics and Automation Letters*, 3(3):2439–2446, 2018.

[109] Zhichao Liu and Konstantinos Karydis. Position control and variable-height trajectory tracking of a soft pneumatic legged robot. In *IEEE/RSJ International Conference on Intelligent Robots and Systems (IROS)*, pages 1708–1709, 2021.

[110] Zhichao Liu and Konstantinos Karydis. Toward impact-resilient quadrotor design, collision characterization and recovery control to sustain flight after collisions. In *IEEE International Conference on Robotics and Automation (ICRA)*, pages 183–189, 2021.

[111] Zhichao Liu, Zhouyu Lu, Ali-akbar Agha-mohammadi, and Konstantinos Karydis. Contact-prioritized planning of impact-resilient aerial robots with an integrated compliant arm. *IEEE/ASME Transactions on Mechatronics*, 2023 (in press).

[112] Zhichao Liu, Zhouyu Lu, and Konstantinos Karydis. Sorx: A soft pneumatic hexapedal robot to traverse rough, steep, and unstable terrain. In *IEEE International Conference on Robotics and Automation (ICRA)*, pages 420–426, 2020.

[113] Zhichao Liu, Caio Mucchiani, Keran Ye, and Konstantinos Karydis. Safely catching aerial micro-robots in mid-air using an open-source aerial robot with soft gripper. *Frontiers in Robotics and AI*, 9, 2022.

[114] Zhouyu Lu, Zhichao Liu, Merrick Campbell, and Konstantinos Karydis. Online search-based collision-inclusive motion planning and control for impact-resilient mobile robots. *IEEE Transactions on Robotics*, 2022.

[115] Zhouyu Lu, Zhichao Liu, Gustavo J Correa, and Konstantinos Karydis. Motion planning for collision-resilient mobile robots in obstacle-cluttered unknown environments with risk reward trade-offs. In *IEEE/RSJ International Conference on Intelligent Robots and Systems*, pages 7064–7070, 2020.

[116] Zhouyu Lu, Zhichao Liu, and Konstantinos Karydis. Deformation recovery control and post-impact trajectory replanning for collision-resilient mobile robots. In *IEEE/RSJ International Conference on Intelligent Robots and Systems*, pages 2030–2037, 2021.

[117] Ming Luo, Zhenyu Wan, Yinan Sun, Erik Howard Skorina, Weijia Tao, Fuchen Chen, Lakshay Gopalka, Hao Yang, and Cagdas Denizel Onal. Motion planning and iterative learning control of a modular soft robotic snake. *Frontiers in Robotics and AI*, 7:191, 2020.

[118] Ren C Luo, Jun Sheng, and Peng-Hsi Chang. Biped robot limit cycle walking generation considering energy dissipation caused by impact. In *IEEE International Conference on Advanced Robotics and Intelligent Systems (IROS)*, pages 17–22. IEEE, 2013.

[119] Tobias Mahl, Alexander Hildebrandt, and Oliver Sawodny. A variable curvature continuum kinematics for kinematic control of the bionic handling assistant. *IEEE transactions on robotics*, 30(4):935–949, 2014.

[120] Shixin Mao, Erbao Dong, Hu Jin, Min Xu, and KH Low. Locomotion and gait analysis of multi-limb soft robots driven by smart actuators. In *IEEE/RSJ International Conference on Intelligent Robots and Systems (IROS)*, pages 2438–2443, 2016.

[121] Andrew D Marchese, Cagdas D Onal, and Daniela Rus. Autonomous soft robotic fish capable of escape maneuvers using fluidic elastomer actuators. *Soft Robotics*, 1(1):75–87, 2014.

[122] Andrew D Marchese and Daniela Rus. Design, kinematics, and control of a soft spatial fluidic elastomer manipulator. *The International Journal of Robotics Research*, 35(7):840–869, 2016.

[123] Siddharth Mayya, Pietro Pierpaoli, Girish Nair, and Magnus Egerstedt. Collisions as information sources in densely packed multi-robot systems under mean-field approximations. In *Robotics: Science and Systems*, 2017.

[124] Christopher D McKinnon and Angela P Schoellig. Unscented external force and torque estimation for quadrotors. In *IEEE/RSJ International Conference on Intelligent Robots and Systems (IROS)*, pages 5651–5657, 2016.

[125] Andrew McLaren, Zak Fitzgerald, Geng Gao, and Minas Liarokapis. A passive closing, tendon driven, adaptive robot hand for ultra-fast, aerial grasping and perching. In *IEEE/RSJ International Conference on Intelligent Robots and Systems (IROS)*, pages 5602–5607, 2019.

[126] Lorenz Meier, Dominik Honegger, and Marc Pollefeys. Px4: A node-based multithreaded open source robotics framework for deeply embedded platforms. In *IEEE International Conference on Robotics and Automation (ICRA)*, pages 6235–6240, 2015.

[127] Daniel Mellinger and Vijay Kumar. Minimum snap trajectory generation and control for quadrotors. In *IEEE International Conference on Robotics and Automation (ICRA)*, pages 2520–2525, 2011.

[128] Daniel Mellinger, Quentin Lindsey, Michael Shomin, and Vijay Kumar. Design, modeling, estimation and control for aerial grasping and manipulation. In *IEEE/RSJ International Conference on Intelligent Robots and Systems*, pages 2668–2673, 2011.

[129] Jiawei Meng, Joao Buzzatto, Yuanchang Liu, and Minas Liarokapis. On aerial robots with grasping and perching capabilities: A comprehensive review. *Frontiers in Robotics and AI*, 8, 2021.

[130] Xin Meng, Xilun Ding, and Pin Guo. A net-launching mechanism for uav to capture aerial moving target. In *IEEE International Conference on Mechatronics and Automation (ICMA)*, pages 461–468, 2018.

[131] Stefano Mintchev, Sébastien de Rivaz, and Dario Floreano. Insect-inspired mechanical resilience for multicopters. *IEEE Robotics and Automation Letters*, 2(3):1248–1255, 2017.

[132] Shatadal Mishra, Dangli Yang, Carly Thalman, Panagiotis Polygerinos, and Wenlong Zhang. Design and control of a hexacopter with soft grasper for autonomous object detection and grasping. In *Dynamic Systems and Control Conference*, 2018.

[133] Kartik Mohta, Michael Watterson, Yash Mulgaonkar, Sikang Liu, Chao Qu, Anurag Makineni, Kelsey Saulnier, Ke Sun, Alex Zhu, Jeffrey Delmerico, Konstantinos Karydis, Nikolay Atanasov, Giuseppe Loianno, Davide Scaramuzza, Kostas Daniilidis, C. J. Taylor, and Vijay Kumar. Fast, autonomous flight in gps-denied and cluttered environments. *Journal of Field Robotics*, 35(1):101–120, 2018.

[134] Edward Moore, D Campbell, F Grimminger, and Martin Buehler. Reliable stair climbing in the simple hexapod 'rhex'. In *IEEE International Conference on Robotics and Automation (ICRA)*, volume 3, pages 2222 – 2227, 2002.

[135] Benjamin Morrell, Rohan Thakker, Àngel Santamaria Navarro, Amanda Bouman, Xiaoming Lei, Jeffrey Edlund, Torkom Pailevanian, Tiago Stegun Vaquero, Yun Lin Chang, Thomas Touma, et al. Nebula: Team costar's robotic autonomy solution that won phase ii of darpa subterranean challenge. *Field robotics*, 2:1432–1506, 2022.

[136] Bobak Mosadegh, Panagiotis Polygerinos, Christoph Keplinger, Sophia Wennstedt, Robert F Shepherd, Unmukt Gupta, Jongmin Shim, Katia Bertoldi, Conor J Walsh, and George M Whitesides. Pneumatic networks for soft robotics that actuate rapidly. *Advanced functional materials*, 24(15):2163–2170, 2014.

[137] Mark Mote, Magnus Egerstedt, Eric Feron, Andrew Bylard, and Marco Pavone. Collision-inclusive trajectory optimization for free-flying spacecraft. *Journal of Guidance, Control, and Dynamics*, pages 1–12, 2020.

[138] Caio Mucchiani, Zhichao Liu, Ipsita Sahin, Jared Dube, Linh Vu, Elena Kokkoni, and Konstantinos Karydis. Closed-loop position control of a pediatric soft robotic wearable device for upper extremity assistance. In *IEEE International Conference on Robot & Human Interactive Communication (RO-MAN)*, 2022.

[139] Mark W Mueller, Seung Jae Lee, and Raffaello D'Andrea. Design and control of drones. *Annual Review of Control, Robotics, and Autonomous Systems*, 5, 2021.

[140] Yash Mulgaonkar, Wenxin Liu, Dinesh Thakur, Kostas Daniilidis, Camillo J Taylor, and Vijay Kumar. The tiercel: A novel autonomous micro aerial vehicle that can map the environment by flying into obstacles. In *IEEE International Conference on Robotics and Automation (ICRA)*, pages 7448–7454, 2020.

[141] Yash Mulgaonkar, Anurag Makineni, Luis Guerrero-Bonilla, and Vijay Kumar. Robust aerial robot swarms without collision avoidance. *IEEE Robotics and Automation Letters*, 3(1):596–603, 2017.

[142] Roberto Naldi, Alessio Torre, and Lorenzo Marconi. Robust control of a miniature ducted-fan aerial robot for blind navigation in unknown populated environments. *IEEE Transactions on Control Systems Technology*, 23(1):64–79, 2014.

[143] Pham H Nguyen, Karishma Patnaik, Shatadal Mishra, Panagiotis Polygerinos, and Wenlong Zhang. A soft-bodied aerial robot for collision resilience and contact-reactive perching. *Soft Robotics*, 2023.

[144] Cagdas D Onal and Daniela Rus. Autonomous undulatory serpentine locomotion utilizing body dynamics of a fluidic soft robot. *Bioinspiration & biomimetics*, 8(2):026003, 2013.

[145] Sangyul Park, Jeongseob Lee, Joonmo Ahn, Myungsin Kim, Jongbeom Her, Gi-Hun Yang, and Dongjun Lee. Odar: Aerial manipulation platform enabling omnidirectional wrench generation. *IEEE/ASME Transactions on Mechatronics*, 23(4):1907–1918, 2018.

[146] Seongjoon Park, Hyeong Tae Kim, Sangmin Lee, Hyeontae Joo, and Hwangnam Kim. Survey on anti-drone systems: Components, designs, and challenges. *IEEE Access*, 9:42635–42659, 2021.

[147] Karishma Patnaik, Shatadal Mishra, Zachary Chase, and Wenlong Zhang. Collision recovery control of a foldable quadrotor. In *IEEE/ASME International Conference on Advanced Intelligent Mechatronics (AIM)*, pages 418–423, 2021.

[148] Karishma Patnaik and Wenlong Zhang. Towards reconfigurable and flexible multirotors. *International Journal of Intelligent Robotics and Applications*, pages 1–16, 2021.

[149] Panagiotis Polygerinos, Stacey Lyne, Zheng Wang, Luis Fernando Nicolini, Bobak Mosadegh, George M Whitesides, and Conor J Walsh. Towards a soft pneumatic

glove for hand rehabilitation. In *IEEE/RSJ International Conference on Intelligent Robots and Systems*, pages 1512–1517, 2013.

[150] Marija Popović, Teresa Vidal-Calleja, Gregory Hitz, Inkyu Sa, Roland Siegwart, and Juan Nieto. Multiresolution mapping and informative path planning for UAV-based terrain monitoring. In *IEEE/RSJ Int. Conf. on Intell. Robots and Syst. (IROS)*, pages 1382–1388, 2017.

[151] Paul EI Pounds, Daniel R Bersak, and Aaron M Dollar. Grasping from the air: Hovering capture and load stability. In *IEEE International Conference on Robotics and Automation (ICRA)*, pages 2491–2498, 2011.

[152] Paul EI Pounds, Daniel R Bersak, and Aaron M Dollar. Practical aerial grasping of unstructured objects. In *IEEE Conference on Technologies for Practical Robot Applications*, pages 99–104, 2011.

[153] Abbaraju Praveen, Xin Ma, Harikrishnan Manoj, Vishnunandan LN Venkatesh, Mo Rastgaar, and Richard M Voyles. Inspection-on-the-fly using hybrid physical interaction control for aerial manipulators. In *IEEE/RSJ International Conference on Intelligent Robots and Systems (IROS)*, pages 1583–1588, 2020.

[154] James A Preiss, Wolfgang Hönig, Nora Ayanian, and Gaurav S Sukhatme. Downwash-aware trajectory planning for large quadrotor teams. In *IEEE/RSJ International Conference on Intelligent Robots and Systems (IROS)*, pages 250–257, 2017.

[155] Zhi Qiao, Pham H Nguyen, Panagiotis Polygerinos, and Wenlong Zhang. Dynamic modeling and motion control of a soft robotic arm segment. In *American Control Conference (ACC)*, pages 5438–5443, 2019.

[156] Yun Qin, Zhenyu Wan, Yinan Sun, Erik H Skorina, Ming Luo, and Cagdas D Onal. Design, fabrication and experimental analysis of a 3-d soft robotic snake. In *2018 IEEE International Conference on Soft Robotics (RoboSoft)*, pages 77–82. IEEE, 2018.

[157] P Ramon-Soria, Alejandro Ernesto Gomez-Tamm, Francisco Javier Garcia-Rubiales, Begoña C Arrue, and Aníbal Ollero. Autonomous landing on pipes using soft gripper for inspection and maintenance in outdoor environments. In *IEEE/RSJ International Conference on Intelligent Robots and Systems (IROS)*, pages 5832–5839, 2019.

[158] Ioannis Rekleitis, Gregory Dudek, and Evangelos Milios. Multi-robot collaboration for robust exploration. *Annals of Mathematics and Artificial Intelligence*, 31:7–40, 2001.

[159] Charles Richter, Adam Bry, and Nicholas Roy. Polynomial trajectory planning for aggressive quadrotor flight in dense indoor environments. In *Robotics Research*, pages 649–666. Springer, 2016.

[160] Robin Ritz, Mark W Müller, Markus Hehn, and Raffaello D'Andrea. Cooperative quadrocopter ball throwing and catching. In *IEEE/RSJ International Conference on Intelligent Robots and Systems (IROS)*, pages 4972–4978, 2012.

[161] E Rocon, AF Ruiz, R Raya, A Schiele, Jose L Pons, JM Belda-Lois, R Poveda, MJ Vivas, and JC Moreno. Human-robot physical interaction. *Wearable robots: Biomechatronic exoskeletons*, pages 127–163, 2008.

[162] Alejandro Rodriguez-Ramos, Adrian Alvarez-Fernandez Hriday Bavle, Javier Rodriguez-Vazquez, Liang Lu Miguel Fernandez-Cortizas, Ramon A Suarez Fernandez, Alberto Rodelgo, Carlos Santos, Martin Molina, Luis Merino, Fernando Caballero, et al. Autonomous aerial robot for high-speed search and intercept applications. *arXiv preprint arXiv:2112.05465*, 2021.

[163] Julian Rothe, Michael Strohmeier, and Sergio Montenegro. A concept for catching drones with a net carried by cooperative uavs. In *IEEE International Symposium on Safety, Security, and Rescue Robotics (SSRR)*, pages 126–132, 2019.

[164] Fabio Ruggiero, Vincenzo Lippiello, and Anibal Ollero. Aerial manipulation: A literature review. *IEEE Robotics and Automation Letters*, 3(3):1957–1964, 2018.

[165] Fabio Ruggiero, Miguel Angel Trujillo, Raul Cano, H Ascorbe, Antidio Viguria, C Peréz, Vincenzo Lippiello, Aníbal Ollero, and Bruno Siciliano. A multilayer control for multirotor uavs equipped with a servo robot arm. In *IEEE International Conference on Robotics and Automation (ICRA)*, pages 4014–4020, 2015.

[166] Fernando Ruiz, Begoña C Arrue, and Aníbal Ollero. Sophie: Soft and flexible aerial vehicle for physical interaction with the environment. *IEEE Robotics and Automation Letters*, 7(4):11086–11093, 2022.

[167] Juergen Rummel, Yvonne Blum, H Moritz Maus, Christian Rode, and Andre Seyfarth. Stable and robust walking with compliant legs. In *IEEE International Conference on Robotics and Automation (ICRA)*, pages 5250–5255, 2010.

[168] Daniela Rus and Michael T Tolley. Design, fabrication and control of soft robots. *Nature*, 521(7553):467–475, 2015.

[169] Ali Sadeghi, Alessio Mondini, Emanuela Del Dottore, Anand Kumar Mishra, and Barbara Mazzolai. soft-legged wheel-based robot with terrestrial locomotion abilities. *Frontiers in Robotics and AI*, 3:73, 2016.

[170] Uluc Saranlı. Dynamic locomotion with a hexapod robot. *Dizertační práce, The University of Michigan*, 2002.

[171] Uluc Saranli, Martin Buehler, and Daniel E Koditschek. Rhex: A simple and highly mobile hexapod robot. *The International Journal of Robotics Research*, 20(7):616–631, 2001.

[172] Uluc Saranli, Martin Buehler, and Daniel E. Koditschek. Rhex: A simple and highly mobile hexapod robot. *The International Journal of Robotics Research*, 20(7):616–631, 2001.

[173] Pooya Sareh, Pisak Chermprayong, Marc Emmanuelli, Haris Nadeem, and Mirko Kovac. Rotorigami: A rotary origami protective system for robotic rotorcraft. *Science Robotics*, 3(22), 2018.

[174] Sergei Savin, Amer Al Badr, Dmitry Devitt, Roman Fedorenko, and Alexandr Klimchik. Mixed-integer-based path and morphing planning for a tensegrity drone. *Applied Sciences*, 12(11):5588, 2022.

[175] Stefan Scherzinger, Arne Roennau, and Rüdiger Dillmann. Forward dynamics compliance control (fdcc): A new approach to cartesian compliance for robotic manipulators. In *IEEE/RSJ International Conference on Intelligent Robots and Systems (IROS)*, pages 4568–4575, 2017.

[176] Tobias Schoels, Per Rutquist, Luigi Palmieri, Andrea Zanelli, Kai O Arras, and Moritz Diehl. Ciao$*$: Mpc-based safe motion planning in predictable dynamic environments. *IFAC-PapersOnLine*, 53(2):6555–6562, 2020.

[177] Jean Scholtz. Theory and evaluation of human robot interactions. In *IEEE International Conference on System Sciences (ICSS)*, pages 10–pp, 2003.

[178] Luis Sentis, Jaeheung Park, and Oussama Khatib. Compliant control of multicontact and center-of-mass behaviors in humanoid robots. *IEEE Transactions on robotics*, 26(3):483–501, 2010.

[179] S. Seok, A. Wang, Meng Yee Chuah, D. Otten, J. Lang, and S. Kim. Design principles for highly efficient quadrupeds and implementation on the mit cheetah robot. In *IEEE International Conference on Robotics and Automation (ICRA)*, pages 3307–3312, 2013.

[180] Hazim Shakhatreh, Ahmad H Sawalmeh, Ala Al-Fuqaha, Zuochao Dou, Eyad Almaita, Issa Khalil, Noor Shamsiah Othman, Abdallah Khreishah, and Mohsen Guizani. Unmanned aerial vehicles (uavs): A survey on civil applications and key research challenges. *IEEE Access*, 7:48572–48634, 2019.

[181] Robert F Shepherd, Filip Ilievski, Wonjae Choi, Stephen A Morin, Adam A Stokes, Aaron D Mazzeo, Xin Chen, Michael Wang, and George M Whitesides. Multigait soft robot. *Proceedings of the national academy of sciences*, 108(51):20400–20403, 2011.

[182] Thomas B Sheridan. Human–robot interaction: status and challenges. *Human factors*, 58(4):525–532, 2016.

[183] Fan Shi, Moju Zhao, Masaki Murooka, Kei Okada, and Masayuki Inaba. Aerial regrasping: Pivoting with transformable multilink aerial robot. In *IEEE International Conference on Robotics and Automation (ICRA)*, pages 200–207, 2020.

[184] Lu Shi, Zhichao Liu, and Konstantinos Karydis. Koopman operators for modeling and control of soft robotics. *Current Robotics Reports*, 2023 (in press).

[185] Jun Shintake, Vito Cacucciolo, Dario Floreano, and Herbert Shea. Soft robotic grippers. *Advanced materials*, 30(29):1707035, 2018.

[186] Jing Shu and Pakpong Chirarattananon. A quadrotor with an origami-inspired protective mechanism. *IEEE Robotics and Automation Letters*, 4(4):3820–3827, 2019.

[187] B Siciliano and L Villani. Adaptive compliant control of robot manipulators. *Control Engineering Practice*, 4(5):705–712, 1996.

[188] Erik H Skorina, Ming Luo, Selim Ozel, Fuchen Chen, Weijia Tao, and Cagdas D Onal. Feedforward augmented sliding mode motion control of antagonistic soft pneumatic actuators. In *2015 IEEE International Conference on Robotics and Automation (ICRA)*, pages 2544–2549. IEEE, 2015.

[189] Koushil Sreenath, Taeyoung Lee, and Vijay Kumar. Geometric control and differential flatness of a quadrotor uav with a cable-suspended load. In *IEEE Conference on Decision and Control (CDC)*, pages 2269–2274, 2013.

[190] Koushil Sreenath, Hae-Won Park, Ioannis Poulakakis, and Jessy W Grizzle. A compliant hybrid zero dynamics controller for stable, efficient and fast bipedal walking on mabel. *The International Journal of Robotics Research*, 30(9):1170–1193, 2011.

[191] Adam Stager and Herbert G Tanner. Composition of local potential functions with reflection. In *IEEE International Conference on Robotics and Automation (ICRA)*, pages 5558–5564, 2019.

[192] Nicolas Staub, Davide Bicego, Quentin Sablé, Victor Arellano, Subodh Mishra, and Antonio Franchi. Towards a flying assistant paradigm: the othex. In *IEEE International Conference on Robotics and Automation (ICRA)*, pages 6997–7002, 2018.

[193] Brett Stephens, Hai-Nguyen Nguyen, Salua Hamaza, and Mirko Kovac. An integrated framework for autonomous sensor placement with aerial robots. *IEEE/ASME Transactions on Mechatronics*, 2022.

[194] William Stewart, Enrico Ajanic, Matthias Müller, and Dario Floreano. How to swoop and grasp like a bird with a passive claw for a high-speed grasping. *IEEE/ASME Transactions on Mechatronics*, 2022.

[195] A Suarez, AE Jimenez-Cano, VM Vega, G Heredia, A Rodriguez-Castaño, and A Ollero. Lightweight and human-size dual arm aerial manipulator. In *IEEE International Conference on Unmanned Aircraft Systems (ICUAS)*, pages 1778–1784, 2017.

[196] Yuuta Sugiyama, Ayumi Shiotsu, Masashi Yamanaka, and Shinichi Hirai. Circular/spherical robots for crawling and jumping. In *IEEE International Conference on Robotics and Automation (ICRA)*, pages 3595–3600, 2005.

[197] Qiao Sun, Feng Gao, and Xianbao Chen. Towards dynamic alternating tripod trotting of a pony-sized hexapod robot for disaster rescuing based on multi-modal impedance control. *Robotica*, 36(7):1048—-1076, 2018.

[198] Takashi Takuma, Shinji Hayashi, and Koh Hosoda. 3d bipedal robot with tunable leg compliance mechanism for multi-modal locomotion. In *IEEE/RSJ International Conference on Intelligent Robots and Systems (IROS)*, pages 1097 – 1102, 2008.

[199] Charbel Tawk, Emre Sariyildiz, Hao Zhou, Marc in het Panhuis, Geoffrey M Spinks, and Gursel Alici. Position control of a 3d printed soft finger with integrated soft pneumatic sensing chambers. In *IEEE International Conference on Soft Robotics (RoboSoft)*, pages 446–451, 2020.

[200] Thomas C. Thayer, Stavros Vougioukas, Ken Goldberg, and Stefano Carpin. Routing algorithms for robot assisted precision irrigation. In *IEEE International Conference on Robotics and Automation*, pages 2221–2228, 2018.

[201] Thomas C. Thayer, Stavros Vougioukas, Ken Goldberg, and Stefano Carpin. Bi-objective routing for robotic irrigation and sampling in vineyards. In *IEEE International Conference on Automation. Science and Engineering*, pages 1481–1488, 2019.

[202] Justin Thomas, Morgan Pope, Giuseppe Loianno, Elliot W Hawkes, Matthew A Estrada, Hao Jiang, Mark R Cutkosky, and Vijay Kumar. Aggressive flight with quadrotors for perching on inclined surfaces. *Journal of Mechanisms and Robotics*, 8(5):051007, 2016.

[203] Thomas George Thuruthel, Egidio Falotico, Federico Renda, and Cecilia Laschi. Model-based reinforcement learning for closed-loop dynamic control of soft robotic manipulators. *IEEE Transactions on Robotics*, 35(1):124–134, 2018.

[204] Michael T Tolley, Robert F Shepherd, Bobak Mosadegh, Kevin C Galloway, Michael Wehner, Michael Karpelson, Robert J Wood, and George M Whitesides. A resilient, untethered soft robot. *Soft robotics*, 1(3):213–223, 2014.

[205] Teodor Tomić, Christian Ott, and Sami Haddadin. External wrench estimation, collision detection, and reflex reaction for flying robots. *IEEE Transactions on Robotics*, 33(6):1467–1482, 2017.

[206] Marco Tranzatto, Frank Mascarich, Lukas Bernreiter, Carolina Godinho, Marco Camurri, Shehryar Masaud Khan Khattak, Tung Dang, Victor Reijgwart, Johannes Loeje, David Wisth, et al. Cerberus: Autonomous legged and aerial robotic exploration in the tunnel and urban circuits of the darpa subterranean challenge. *Journal of Field Robotics*, 2021.

[207] Vasileios Vasilopoulos, Iosif S Paraskevas, and Evangelos G Papadopoulos. Compliant terrain legged locomotion using a viscoplastic approach. In *IEEE/RSJ International Conference on Intelligent Robots and Systems (IROS)*, pages 4849–4854, 2014.

[208] Björn Verrelst, Ronald Van Ham, Bram Vanderborght, Frank Daerden, Dirk Lefeber, and Jimmy Vermeulen. The pneumatic biped lucy actuated with pleated pneumatic artificial muscles. *Autonomous Robots*, 18:201–213, 2005.

[209] BV Vidyadhara, Lima Agnel Tony, Mohitvishnu S Gadde, Shuvrangshu Jana, VP Varun, Aashay Anil Bhise, Suresh Sundaram, and Debasish Ghose. Design and integration of a drone based passive manipulator for capturing flying targets. *Robotica*, 40(7):2349–2364, 2022.

[210] Han W Wopereis, Jim Johan Hoekstra, Tjark Harrie Post, Gerrit A Folkertsma, Stefano Stramigioli, and Matteo Fumagalli. Application of substantial and sustained force to vertical surfaces using a quadrotor. In *IEEE International Conference on Robotics and Automation (ICRA)*, pages 2704–2709, 2017.

[211] Burak Yüksel, Saber Mahboubi, Cristian Secchi, Heinrich H Bülthoff, and Antonio Franchi. Design, identification and experimental testing of a light-weight flexible-joint arm for aerial physical interaction. In *IEEE International Conference on Robotics and Automation (ICRA)*, pages 870–876, 2015.

[212] Burak Yúksel, Cristian Secchi, Heinrich H Búlthoff, and Antonio Franchi. A nonlinear force observer for quadrotors and application to physical interactive tasks. In *IEEE/ASME International Conference on Advanced Intelligent Mechatronics (AIM)*, pages 433–440, 2014.

[213] Alexander Zelinsky. A mobile robot navigation exploration algorithm. *IEEE Transactions of Robotics and Automation*, 8(6):707–717, 1992.

[214] Jiaming Zha and Mark W Mueller. Exploiting collisions for sampling-based multicopter motion planning. In *IEEE International Conference on Robotics and Automation (ICRA)*, pages 7943–7949, 2021.

[215] Jiaming Zha, Xiangyu Wu, Joseph Kroeger, Natalia Perez, and Mark W Mueller. A collision-resilient aerial vehicle with icosahedron tensegrity structure. In *IEEE/RSJ International Conference on Intelligent Robots and Systems (IROS)*, pages 1407–1412, 2020.

[216] Guangyu Zhang, Yuqing He, Bo Dai, Feng Gu, Liying Yang, Jianda Han, Guangjun Liu, and Juntong Qi. Grasp a moving target from the air: System & control of an aerial manipulator. In *IEEE International Conference on Robotics and Automation (ICRA)*, pages 1681–1687, 2018.

[217] Haijie Zhang, Jiefeng Sun, and Jianguo Zhao. Compliant bistable gripper for aerial perching and grasping. In *IEEE International Conference on Robotics and Automation (ICRA)*, pages 1248–1253, 2019.

[218] Moju Zhao, Koji Kawasaki, Xiangyu Chen, Shintaro Noda, Kei Okada, and Masayuki Inaba. Whole-body aerial manipulation by transformable multirotor with two-dimensional multilinks. In *IEEE International Conference on Robotics and Automation (ICRA)*, pages 5175–5182, 2017.

[219] Na Zhao, Yudong Luo, Hongbin Deng, Yantao Shen, and Hao Xu. The deformable quad-rotor enabled and wasp-pedal-carrying inspired aerial gripper. In *IEEE/RSJ International Conference on Intelligent Robots and Systems (IROS)*, pages 1–9, 2018.

[220] Boyu Zhou, Jie Pan, Fei Gao, and Shaojie Shen. Raptor: Robust and perception-aware trajectory replanning for quadrotor fast flight. *IEEE Transactions on Robotics*, 37(6):1992–2009, 2021.

[221] Xiaodong Zhou and Shusheng Bi. A survey of bio-inspired compliant legged robot designs. *Bioinspiration & biomimetics*, 7(4):041001, 2012.